LUND UNIVERSITY

Fault Behavior of Wind Turbines

Sulla, Francesco

2012

Total number of authors:
1

Fault Behavior of Wind Turbines

Francesco Sulla

LUND UNIVERSITY

**Doctoral Dissertation
Department of Measurement Technology and
Industrial Electrical Engineering**

2012

To my family

Abstract

Synchronous generators have always been the dominant generation type in the grid. This fact affected both planning and operation of power systems. With the fast increase of wind power share in the grid in the last decade, the situation is changing. In some countries wind power represents already a consistent amount of the total generation. Wind turbines can be classified as non-synchronous generation and they behave differently than synchronous generation under many circumstances. Fault behavior is an important example. This thesis deals with the behavior of wind turbines during faults in the grid. The first part focuses on the fault currents delivered by wind turbines with Doubly-Fed Induction Generators (DFIG). The second part investigates the impact of faults below the transmission level on wind turbine grid fault ride-through and the voltage support that wind turbines can provide in weak grids during faults.

A wide theoretical analysis of the fault current contribution of DFIG wind turbines with crowbar protection is carried out. A general analytical method for fault current calculation during symmetrical and unsymmetrical faults in the grid is proposed. The analytical method can be used to find the maximum fault current and its AC or DC components without the need to actually perform detailed simulations, which is the method used today.

DFIG wind turbines may also be protected using a chopper resistance on the DC-link. A method to model the DC-link with chopper as an equivalent resistance connected to the generator rotor during symmetrical grid faults is presented. This allows to calculate the short-circuit currents of a DFIG with chopper protection as an equivalent DFIG with crowbar protection. This is

useful since fault current calculation methods for DFIG with crowbar are available in the literature. Moreover, power system simulation tools include standard models of DFIG wind turbines with crowbar protection, but often not with chopper protection.

The use of an aggregate model to represent the fault current contribution of a wind farm has been analyzed through simulations. It has been found that the aggregate model is able to reproduce accurately the total fault current of the wind farm for symmetrical and unsymmetrical faults. The use of aggregate models simplifies simulation models and saves simulation time.

The Swedish grid code requires wind turbines at all voltage levels to ride through faults at the transmission network. For faults at voltage levels below transmission level fault clearing times are often longer and this could impact on fault ride-through of wind turbines. Simulation of study cases with faults at sub-transmission level, performed using the standard Nordic 32 test system, show that wind turbines should still be able to ride through such faults. Only in case of high dynamic load scenarios and failure of the protection system, wind turbines could disconnect from the grid. Load modelling is important when carrying out this analysis. Faults on adjacent MV feeders seriously endanger grid fault ride-through (GFRT) of wind turbines.

Finally, an investigation on the voltage support of wind turbines in weak networks during faults has been carried out. A simplified model of the power system of the Danish island of Bornholm has been used as a test system. It has been found that the minimum requirements for voltage support set by grid codes do not result in satisfactory voltage recovery in weak grids after fault clearing. However, if properly controlled, wind turbines are able to provide a voltage support comparable to that supplied by power plants with synchronous generation.

Acknowledgements

I would like to thank all the people I met here in Lund and that contributed to a nice social life outside of the department. In particular Kasia, Kinga, Luca, Anna, Yuri, Johan for all the nice dinners, lunches, evenings, concerts, excursions. Thanks for the nice time.

Finally, I want to dedicate this thesis to my wife Ela, to my parents and to my sister. Questa tesi e' dedicata a voi.

Lund, April 2012
Francesco Sulla

Preface

When I started in 2006, the subject of my Ph.D. studies was island operation with induction generators. That project was financed by Svenska Kraftnät and was divided into two sub-projects. I was responsible for the part on fault analysis and protection. That work was documented in a Licentiate thesis, published in 2009. Since the project was not continued another project was formulated.

At the end of 2009, this project titled "Power system integration of non-synchronous generation" was started, financed by Elforsk AB. This project is also divided into two sub-projects. This thesis deals with the part on fault current contribution and grid fault ride-through of wind turbines. The other part focuses on the impact of non-synchronous generation on power system frequency.

Contents

Chapter 1

Introduction

The amount of installed renewable energy in the electric power system has been steadily increasing in the past decades. This trend is due to different factors, social, environmental, political, economical and technological. Society increasingly demands for environmentally acceptable energy solutions; governments often promote renewable energy sources by economically subsidizing their installation; technology and economics of some types of renewable energy have evolved to a point that makes them competitive with electricity generation based on fossil fuel or nuclear power.

After hydropower, wind energy is the most mature among the renewable energy technologies. According to (Pure Power 2011) the global cumulative wind power capacity installed in the whole world increased from 6.1 GW in 1996 to 197 GW in 2010 and the global annual installed wind power capacity has been slightly over 38 GW both in 2009 and 2010. This number represents 20 % of the total new electric power capacity installed in the world in 2010, equal to 194 GW (REN21 2011). In the past decade, from 2001 to 2010, the global wind power capacity increased by 180 GW, while in the same period the total new installed nuclear capacity has been 26 GW (Pure Power 2011). In countries like Denmark and Spain, the wind energy production in year 2010 represented a share of 25 % and 15 % respectively of the annual electricity consumption in the country, referred to year 2008. This trend can be found also in Sweden; the total installed wind power in 2010 was slightly over 2 GW and the wind energy production grew from 0.63 TWh in 2003 to 3.51 TWh in 2010, corresponding to 2.4 % of the total electricity production (Vindkraftstatistik 2010). Preliminary data indicate that wind energy production in Sweden grew to 6.1 TWh in year 2011 and is expected to reach 8 TWh 2012. In (Pure Power 2011) scenarios are also

presented for wind power development in the EU up to 2020. In the "Baseline" scenario, wind power is expected to increase from a share of 5.3 % in 2010 to roughly more than 15 % in 2020 of the total EU electricity demand.

The growth in installed wind power capacity has been accompanied by advances in wind turbine technology. The average size of installed wind turbines has continually increased, passing, e.g. in Sweden, from 0.6 MW until 2003 to 1.9 MW in 2010 (Vindkraftstatistik 2010). Wind turbines up to a 6 MW range are today available on the market and wind turbines in the 10 MW range are under design (Manwell 2009).

The electrical technology in the wind turbines has also evolved. The first wind turbines were equipped with squirrel-cage induction generators (SCIGs) directly connected to the grid. These wind turbines operated at almost fixed speed and suffered from high flicker emission. Partly-variable-speed wind turbines with induction generators equipped with a dynamic rotor resistance allow operation at up to 10 % super-synchronous speed and can be controlled to reduce flicker emission and mechanical stresses by absorbing the fluctuating wind power into the rotor kinetic energy and the external rotor resistance (Akhmatov 2005). Modern wind turbines are of variable-speed type. The most common solutions have a Doubly-Fed Induction Generator (DFIG) or an induction or synchronous generator interfaced to the grid through a Full-Scale Converter (FSC). They are able to optimize the power extraction at wind speeds below rated speed, have low flicker emission and feed a smooth power into the grid (Akhmatov 2005). Both these types of wind turbines are equipped with power electronic back-to-back converters.

Up to some years ago, wind turbines were required to disconnect from the grid during severe disturbances. This would avoid any possible negative effect of wind turbines on the grid voltage and the fault clearing system and it would eliminate the risk for non-intentional islanding with its associated safety risks (Piwko 2010). With the high penetration reached by wind power today this solution is no longer viable, since it could result in the disconnection of a large amount of generation, weakening the power system and possibly creating problems for the frequency control. As a consequence, the latest national grid codes require wind turbines to remain connected and ride-through a fault in the grid providing active and reactive power support.

1.1   Motivation

The requirement on grid fault ride-through radically changed the role wind

turbines play in the power system during and immediately after a disturbance. Wind turbines must now remain connected through the whole duration of the disturbance under specific circumstances.

Remaining connected to the grid during a fault, wind turbines will also feed short-circuit current into the grid. The short-circuit current delivered by wind turbines is different from the short-circuit current fed into the grid by synchronous generators. In areas with a high concentration of wind power this may impact on the operation of protection relays. Knowledge of the short-circuit current delivered by wind turbines is also of importance for power system component sizing. The relevance of this topic is underlined by the fact that a special Joint Working Group has been set up in 2008 by the IEEE Power System Relay Committee in order to investigate the short-circuit current delivered by wind turbines. The assignment of the Working Group is (Webpage, http://www.pes-psrc.org/c/CWG17.html): *"To support the activities … in the production of a report that characterizes and quantifies the short circuit current contributions to faults from wind plants for the purposes of determining protective relay settings and fault interrupting equipment ratings. The report will provide guidelines on the modeling and calculations for that purpose"*.

Wind turbines of different type will deliver different short-circuit currents. For wind turbines with FSC, the short-circuit current is mainly determined by the control scheme and therefore it is also manufacturer-dependent. For wind turbines equipped with DFIGs and fixed-speed wind turbines, it is instead the physical system that determines the short-circuit behavior immediately after severe voltage dips. For these wind turbines it is therefore possible to lay down a general treatment of the short-circuit behavior. The short-circuit behavior of wind turbines with DFIG is of particular interest, since this is the most commonly installed type of wind turbine in the last decade and will continue to represent a significant share of the total wind power installed in the power system for many years to come.

Some grid codes also require wind turbines to be able to supply voltage support during depressed voltage conditions and quickly return to normal operating conditions once the grid disturbance has ceased. The limiting voltage dip profile conditions above which wind turbines are required to ride-through a fault are specified in the national grid codes and vary from country to country. Such a profile is a voltage-time curve representing a limiting condition within which voltage dips are expected to be contained, following faults in a point in the grid and the subsequent clearing by the protection system under normal circumstances.

The research into grid fault ride-through of wind turbines has flourished in the last years and this fact underlines by itself the relevance of the topic. A multitude of papers produced by academics have been accompanied by advanced hardware and software solutions adopted in the new wind turbines by manufacturers to assure grid fault ride-through capability. The competition in the field among manufacturers is fierce and this makes it very difficult to get detailed information on the particular grid fault ride-through technical solutions adopted in commercial wind turbines.

The vast majority of the literature publications in the field focuses on technical solutions for the individual wind turbine to assure ride-through capability when a specified voltage dip profile is assumed. Less explored in the literature is the grid fault ride-through behavior of wind turbines for faults in the sub-transmission and medium voltage network. In these cases, the voltage dip profiles resulting from a fault depend on the protection system used at these voltage levels and the type of load in the grid (Souza 2010); the voltage dip may last long enough to endanger the grid fault ride-through capability of wind turbines. On the other hand, the extension of the area of the grid interested by the voltage dip is more limited as compared to a fault in the transmission level (Souza 2010, Dahlgren 2006). It seems therefore interesting to further investigate these issues to better understand in which cases wind turbines may be expected to disconnect from the grid and to get an insight onto the extension of the area affected by the voltage dip.

Another topic that has not been extensively researched is how wind turbines installed in weak networks perform during a disturbance in the grid. Modern wind turbines have voltage support capability and may represent an asset to improve voltage performance in these situations. In (Neumann 2011, Shawarega 2009, Ullah 2007, Ashkhane 2011), it is suggested that a high proportional gain and continuous voltage regulation without deadband may result in better voltage during a fault. Also, active power injection from wind turbines is pointed out as a cause that deteriorates the voltage support offered by reactive power injection. However, a general treatment of the voltage support of wind turbines in weak networks is seldom found in the literature and many open issues still remain. What is the best voltage support strategy for wind turbines in weak networks, how does this strategy depend on the grid short-circuit power and X/R ratio, how does the active power injection affect the voltage recovery after fault clearing, are the basic requirements contained in the grid codes enough to achieve a satisfactory voltage recovery in weak networks? An investigation of these aspects is useful and helpful in fully exploiting the voltage support capabilities of wind turbines in weak networks.

1.2   Objectives and Outline of the Thesis

This thesis deals with the behavior of wind turbines during grid disturbances. The main objectives of the thesis can be summarized as follows:

- Analyze the short-circuit current fed into the grid by DFIG wind turbines both with crowbar and DC-chopper protection.

- Analyze the fault current contribution of wind farms.

- Investigate voltage profiles resulting from faults at sub-transmission and medium voltage networks to understand if problems for grid fault ride-through of wind turbines may arise.

- Investigate and devise possible ways to improve voltage support by wind farms in weak networks during a grid disturbance.

A brief theoretical background about wind turbines, the way they are protected and controlled during a grid disturbance and the requirements set by grid codes on fault ride-through is given in Chapter 2.

Wind turbines with DFIG are equipped with a back-to-back converter connected between the grid and the generator rotor. A voltage dip may cause high rotor currents that could damage the converter switches. The standard solution used to protect the converter switches is to divert the rotor current through a so-called crowbar resistance. During a fault, the DFIG is in effect an induction generator with short-circuited rotor, but with high rotor resistance. Approximate methods for estimating the short-circuit currents of such wind turbines for bolted three-phase faults at the machine terminals have been previously published in the literature (Morren 2007), but a general analysis is lacking. In Chapter 3, a theoretical analysis on the symmetrical and unsymmetrical short-circuit current delivered by wind turbines equipped with SCIG and DFIG with crowbar protection is presented.

In the last years, some wind turbine manufactures have adopted a new solution to protect the rotor side converter. Instead of using the standard crowbar solution, the high rotor currents in the event of a fault flow through the anti-parallel diodes of the converter into the DC-link. A chopper resistance is connected across the DC-link capacitor and it is switched to keep the DC-link voltage within an acceptable range. The many non-linearities in this system make it difficult to analyze the short-circuit currents of these wind turbines. A simplified analysis, which is found to be accurate for bolted three-

phase faults and when the wind turbine is at full power, is presented in (Martinez 2011(a)). In Chapter 4, a general analysis of the short-circuit current of such wind turbines for symmetrical faults is presented. The idea of modelling these wind turbines as an equivalent wind turbine with crowbar resistance is used.

The analysis presented in Chapter 3 and 4 allows to predict the short-circuit currents of the individual wind turbine. It may be more interesting to know instead the total short-circuit current delivered by a wind farm with many wind turbines of the same type. The same type of wind turbines in a wind farm may deliver different short-circuit currents mainly because of a different initial state and of voltage drops within the farm. Using an aggregate model of the wind farm is however beneficial and saves simulation time. The validity of aggregate models has been investigated mainly with regards to the active and reactive power contribution (Pöller 2003, Garcia-Gracia 2008) and only limited material is available in the literature on using aggregate models for fault studies (Aluko 2010, Perdana 2008). In Chapter 5, simulations results are presented to assess the validity of an aggregate model for symmetrical and unsymmetrical short-circuit current studies. Wind farms with SCIG and DFIG are both considered.

In Sweden, the voltage profiles for grid fault ride-through in the grid codes are defined with reference to faults in the transmission network (SvKFS 2005:2). Faults at the sub-transmission and medium voltage network may cause voltage profiles quite different from the ones given in the grid codes, mainly because of differences in the protection system, and still affect large areas of the power system. Some case studies are presented in Chapter 6 to gain insight into whether these faults may endanger the grid fault ride-through capability of wind turbines, on the extension of the power system area affected by the voltage dip and on the influence of the load mix composition and load behavior during the disturbance on the voltage dip itself.

Modern wind turbines are able to and by some grid codes required to provide voltage support during a grid disturbance. This capability can be very beneficial in weak networks, where voltage restoration after fault clearing can be slow and much influenced by the connected load. The influence of the proportional gain, of a regulation with or without deadband, on coordinating the active and reactive current injection and on the post-fault active power ramp on the voltage support is investigated in Chapter 7. Different voltage support schemes for wind turbines, including the ones required by the Danish and German (E.ON) grid codes, are compared and some conclusions

are drawn on possible ways to improve the voltage support of wind turbines in weak grids. Finally, the performance of wind turbines in a weak network is compared to that of a power plant with a synchronous generator in a study case, using a simplified model of a real power system, the one of the Danish island of Bornholm.

Chapter 8 summarizes the main conclusions of this work, along with some suggestions for future work.

1.3   Contributions

The major contribution of this thesis is a deep theoretical analysis of the short-circuit currents delivered by wind turbines with DFIG with both crowbar and chopper protection under symmetrical and unsymmetrical faults. A general analytical treatment of the short-circuit behavior of such wind turbines was lacking in the literature. Moreover, an investigation on the voltage dip profiles resulting from faults below transmission level and on the voltage support capability of wind turbines in weak networks has been performed.

A method for calculating the symmetrical and unsymmetrical short-circuit currents of a wind turbine equipped with SCIG or DFIG with crowbar protection is developed. The method results in an analytical expression that allows the calculation of the wind turbine short-circuit currents without the need for dynamic simulations but with an accuracy compared to that obtained by such simulations. The method is applicable during a fault, under the period the rotor side converter switching is blocked and the crowbar resistance is inserted. The analytic expression can also be used to calculate the maximum phase currents for different faults, their DC and AC components, or it may be used to get an envelope of the currents if only their RMS value is needed. The presented method can be seen as analogous to the well known three-phase short-circuit formula of a synchronous generator (Roeper 1985).

Modern DFIG wind turbines may be protected with a chopper resistance on the DC-link, instead of the crowbar resistance. An analysis of the short-circuit behavior of this type of wind turbine is presented. The idea to model the DC-link capacitor and chopper as an equivalent resistance seen from the rotor circuit was introduced in (Martinez 2011(a)). This implies that methods developed for short-circuit current calculations for a DFIG with crowbar resistance are also applicable to a wind turbine with DC chopper. In this thesis it is shown that the value of the equivalent crowbar resistance must be properly chosen, depending on the voltage dip and the initial loading of the

wind turbine, for accurate short-circuit current prediction. The proposed method is particularly useful considering that models of wind turbines with DC chopper are not commonly included in standard simulation tools.

The total short-circuit current contribution of a wind farm has been investigated through simulations in order to assess the validity of an aggregate model for short-circuit current studies. It is found that aggregate models are sufficiently accurate both in the case of wind farms with SCIGs and with DFIGs. This is valid for symmetrical and unsymmetrical faults.

The investigation on the voltage dip profiles for faults at the sub-transmission network shows that only grid buses electrically close to the fault may experience voltage dips that may compromise grid fault ride-through of wind turbines. It is shown how the modelling of the load in the system is essential for the evaluation of the resulting voltage dips and grid fault ride-through. The considered case studies show that wind turbine grid fault ride-through is endangered mainly for faults cleared by the circuit breaker failure protection and under high motor load conditions.

The grid fault ride-through behavior of wind turbines connected to a weak network has been investigated. Wind turbines can actively contribute to improve the voltage during and immediately after a fault in the grid. However, the basic grid code requirements do not always result in satisfactory wind turbine voltage support in weak networks. A high proportional gain for current injection depending on the voltage dip magnitude and continuous voltage regulation without deadband are two ways to improve voltage support. In particular, in weak networks with low X/R ratios of the equivalent grid Thevenin impedance, a coordinated injection of active and reactive current along with fast active power post-fault ramp helps improving the voltage during the fault and the post-fault voltage recovery. A study case using a simplified model of the Bornholm power system shows how the voltage support provided by wind turbines is comparable to the one provided by synchronous generators, if the proper voltage support strategy is chosen.

The thesis presents a wide analysis of the fault behavior of wind turbines with SCIG and DFIG. The expectation is that the analysis will help understanding and predicting the short-circuit behavior of these types of wind turbines.

1.4   Publications

Publications related to this Ph.D. thesis:

[1] Sulla F., Svensson J., Samuelsson O., Symmetrical and Unsymmetrical Short-Circuit Current of Squirrel-Cage and Doubly-Fed Induction Generators, *Electric Power System Research*, vol. 81, No. 7, 2011.

[2] Sulla F., Svensson J., Samuelsson O., Fault Behavior of Wind Farms with Fixed-Speed and Doubly-Fed Induction Generators, *PowerTech 2011 conference*, Trondheim, 19-23 juni 2011.

[3] Sulla F., Svensson J., Samuelsson O., Short-Circuit Analysis of a Doubly Fed Induction Generator Wind Turbine with Direct Current Chopper Protection", *Wind Energy*, first published online 9 December 2011.

Other publications:

[a] Björnstedt J., Sulla F., Samuelsson O., Experimental Investigation on Steady-State and Transient Performance of a Self-Excited Induction Generator, *IET Generation, Transmission and Distribution*, vol. 5, No. 12, 2011.

[b] Sulla F., Björnstedt J., Samuelsson O., Distributed Generation with Voltage Control Capability in the Low Voltage Network, *International Conference on Renewable Energies and Power Quality (ICREPQ'10),* Granada, Spain, March 2010.

[c] Sulla F., Samuelsson O., Short-Circuit Analysis and Protection of a Medium Voltage Network in Island Operation with Induction Generation, *Eight Nordic Distribution and Asset Management Conference (NORDAC2008),* Bergen, Norway, September 2008.

[d] Sulla F., Samuelsson O., Analysis of Island-Operated Distribution Networks with Distributed Induction Generation under Fault Conditions, *43rd International Universities Power Engineering Conference (UPEC2008),* Padova, Italy, September 2008.

[e] Sulla F., Samuelsson O., Estimation of the Zero Sequence Voltage on the D-side of a Dy Transformer by Using One Voltage Transformer on the D-side, *9th International Conference on Developments in Power System Protection (DPSP2008),* Glasgow, UK, March 2008.

Chapter 2

Wind Turbines during Faults

The requirements on grid fault ride-through (GFRT) capability have pushed a rapid evolution of wind turbine technology. Remaining connected to the grid throughout the duration of the fault, wind turbines will feed short-circuit current into the grid, affecting power system planning issues such as component sizing and relay protection settings that have traditionally been based on the short-circuit current contribution of synchronous generators. This chapter starts with presenting the different wind turbine concepts most commonly installed in the power system. A review of the literature on the fault currents of wind turbines is then performed. Finally, requirements on GFRT from some national grid codes are introduced along with protection and control schemes devised to allow wind turbine GFRT capability.

2.1   Wind Turbine Concepts

Commercial wind turbines can be classified into four major types (Hansen 2004), depending on their ability to operate at fixed- or variable-speed and on the size, partial- or full-scale, of the power electronic converter, when used. Fixed-speed wind turbines were the most common type of wind turbines installed until the nineties and there are still many in operation. In year 2000 they still represented 39 % of the total installed wind turbines in the world (Hansen 2004). Though being conceptually simple and cheap, they present many disadvantages that led to a strong decrease of their market share during the last decade. Among other disadvantages, fixed-speed wind turbines deliver a power to the grid which follows wind speed fluctuations, with flicker emission and high mechanical stresses on the drive train as a consequence (Hansen 2004). These drawbacks are eliminated in a limited variable-speed wind turbine. Such wind turbines are able of absorbing the wind power fluctuations and convert them to kinetic energy and heat into an external

rotor resistance, hence suppressing the grid power fluctuations (Akhmatov 2005). However, surveys show that market share of this wind turbine concept has steadily decreased to a quite insignificant level after the nineties (Li 2007). The vast majority of wind turbines installed nowadays is of variable-speed type. They are able to vary the shaft speed over a wide range and perform optimal power extraction from the wind, at low wind speeds, thus increasing the total yearly energy production (Petersson 2005(a)). Power extraction optimization is done by keeping the tip speed ratio close to its optimal value (Ackermann 2005). Moreover, they possess superior control possibilities, enabling grid ancillary services such as reactive power control, frequency and voltage support after grid disturbances. Modern variable-speed wind turbines also have GFRT capability.

Fixed-Speed Wind Turbine, Type A

A fixed-speed wind turbine is equipped with a SCIG directly connected to the grid via a step-up transformer, as shown in Figure 2.1. Due to the steep torque-slip characteristic of a SCIG, it will operate at almost constant speed, with a slip in the order of 2 % at rated power (Akhmatov 2005). The speed of the SCIG is therefore set by the grid frequency.
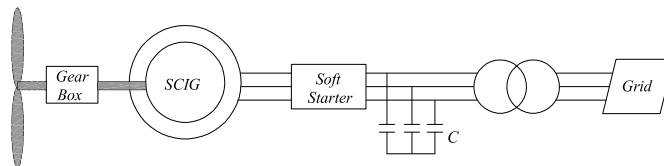
Figure 2.1   Fixed-speed wind turbine with SCIG.

Fixed-speed wind turbines may be stall, pitch or active-stall controlled. To avoid large current transients during grid connection, fixed-speed wind turbines may be connected to the grid through a soft-starter (Hansen 2004).

Due to the stiff connection to the grid, a fixed-speed wind turbine cannot absorb the wind power fluctuations in its rotor kinetic energy. As a consequence, fluctuations in the torque and delivered power will result. Torque fluctuations may cause mechanical stresses to the turbine drive train, while power fluctuations may result in voltage flicker.

A SCIG needs to be magnetized through the network and to decrease the reactive power drawn from the grid in normal operation, capacitor banks are installed at the SCIG terminals. However in case of a voltage dip, the wind

turbine accelerates and draws large amount of reactive power from the grid, well above its need in normal operating conditions. This complicates voltage recovery and could lead to generator overs-peeding and consequent disconnection (Ahkmatov 2005) to avoid voltage stability issues.

Limited Variable-Speed Wind Turbine, Type B

This wind turbine concept uses a wound rotor induction generator (WRIG) and an external resistance that can be connected to the generator rotor through a converter. By controlling the converter, the value of the effective external resistance can be controlled. A scheme of this wind turbine concept is shown in Figure 2.2. When increasing the total rotor resistance, the maximum torque of the slip-torque curve of the induction generator is shifted toward higher slip and higher generator speed. Consequently, if the mechanical power is assumed constant, this results in operation at higher speed.
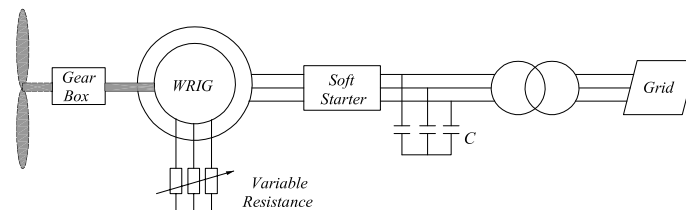
Figure 2.2   Limited variable-speed wind turbine with wound-rotor induction generator and variable rotor resistance.

Limited variable-speed wind turbines can be operated above rated speed, with a maximum slip range above 10 %. The speed range is limited by the high heat losses in the external resistance (Burnham 2009).

This control is mainly used to absorb wind power fluctuations into kinetic energy of the wind turbine shaft and then dissipate them into heat in the external resistance (Akhmatov 2005).

A major drawback of this wind turbine concept is that active and reactive power cannot be independently controlled (Burnham 2009). Just like the fixed-speed concept, this wind turbine draws reactive power from the grid and therefore capacitor banks are used to improve the power factor (Akhmatov 2005).

Variable-Speed Wind Turbine with DFIG, Type C

This type of wind turbine uses a DFIG. The stator of the generator is directly connected to the grid. The rotor is also connected to the grid, but through a back-to-back converter. A three winding step-up transformer may be used, as shown in Figure 2.3. The converter on the rotor side will be referred throughout this thesis as the rotor side converter (RSC), while the converter on the grid side as the grid side converter (GSC).
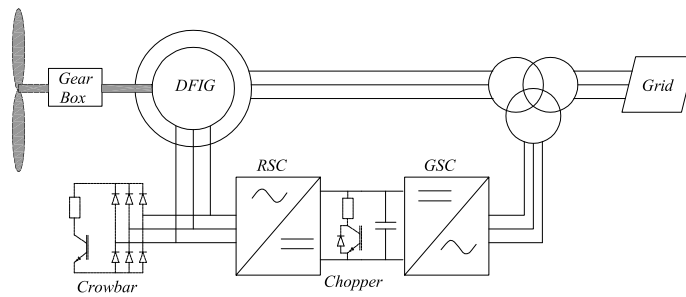
Figure 2.3   Variable-speed wind turbine with DFIG.

The power flow through the rotor can be bidirectional (Akhmatov 2005). The power flows into the rotor when the wind turbine operates at sub-synchronous speed, with low mechanical input power. The rotor power flow reverses at super-synchronous speed. Thus, with high mechanical input power, part of this power is fed to the grid through the stator and part through the back-to-back converter.

The RSC is normally set to control the active and reactive power injection into the grid through the stator. Active and reactive power can be controlled independently by adjusting the external voltage applied to the rotor. By properly adjusting the external rotor voltage, the stator current can be controlled also to deliver a reactive power to the grid. This is a major advantage of this wind turbine type over types A and B. The fast control of the RSC makes it possible to feed a smooth active power into the grid. The RSC can be controlled to optimize the wind power extraction at low wind speeds (Akhmatov 2005).

During normal operation, the GSC controls the DC-link capacitor voltage and usually does not contribute to any reactive power exchange with the grid.

A major advantage of this type of wind turbines is that the back-to-back

converter only needs to be sized to handle approximately 30 % of the generator rated power (Petersson 2005(a)). This is a direct consequence of the fact that the power flowing through the rotor is given by the product of the stator power and the slip and that these wind turbines are operated within a slip range from -0.3 to +0.3. It is also important that the rotor-to-stator turns ratio be chosen properly to reduce the current rating of the converter. If this turns ratio is chosen around 3, the maximum rotor voltage in normal operating conditions will result close to 1 pu. Consequently the rotor current will not exceed 0.3 pu of the stator current.

The major drawback of this wind turbine concept is that it is very sensitive to grid disturbances. A dip in the voltage may in fact cause high currents in the rotor that may damage the RSC. In these situations the switching of the RSC is therefore blocked. There are different schemes to protect a DFIG wind turbine during faults and at the same time allow grid fault ride-through capability. Some of these schemes are exposed in Sections 2.2 and 2.4.

The short-circuit currents delivered by DFIG wind turbines during a fault are widely discussed in Chapter 3 and 4.

Variable-Speed Wind Turbine with FSC, Type D

This wind turbine concept is connected to the grid through a full-scale back-to-back converter. The generator may be either of synchronous or induction type. In the first case, both options with a separately excited and a permanent magnet synchronous generator are available in commercial wind turbines (Manwell 2009). Gearless solutions using a synchronous generator with a high number of poles are also present in the market (Hansen 2004). If an induction generator is used, this needs to be magnetized by the generator side converter. Therefore, this has to be rated to handle not only the rated active power of the generator but also its reactive power. Reactive power can be provided also by capacitors installed at the generator terminals (Akhmatov 2005).

The generator side converter controls the speed of the generator to optimize power extraction from the wind. These wind turbines have a wider operating speed range than wind turbines with DFIG (Tsili 2008). The grid side converter controls the DC-link capacitor voltage feeding active power into the grid. It can also independently control the reactive power injection.
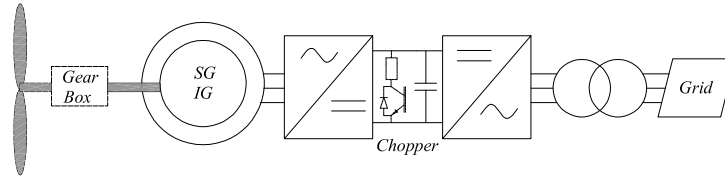
Figure 2.4   Variable-speed wind turbine with full-scale converter. The generator may
            be either of synchronous type, separately excited or permanent-magnet,
            or an induction generator.

Wind turbines with FSC are easier to control during voltage dips in the grid,
as compared to DFIG wind turbines. In this case, the voltage dip does not
directly cause any transient in the generator. The main issue is the rise of the
DC-link capacitor voltage when no active power can be delivered to the grid.
A number of strategies to mitigate and solve this problem are presented in
Section 2.4. The grid side converter can also provide fast reactive power
support.

2.2   Wind Turbine Fault Current

Different types of wind turbines will deliver different fault currents into the
grid in the event of a fault. A brief review on the short-circuit current
provided by different wind turbine types is presented below.

Fixed-Speed Wind Turbines

The short-circuit behavior of fixed-speed wind turbines with a SCIG is
determined by the dynamics of the generator itself. High short-circuit
currents will be delivered during the fault, decaying with the fluxes present in
the generator stator and rotor. The short-circuit behavior of a SCIG has been
analyzed in various text books and in many papers. Closed formulas for the
short-circuit current calculation are given in the case of a bolted three-phase
short-circuit at the generator terminals in (Kovaks 1984, Sarma 1986, Vas
1992, Jenkins 2000). The symmetrical short-circuit current is made up of
two components, an AC and a DC component that decay respectively with
the rotor and stator transient time constants. These formulas have been
deduced based on the assumption that the rotor and stator resistance are
negligible. The effect of the resistance is then accounted for in the transient
time constants. The short-circuit current is limited by the transient reactance,
and its maximum value usually varies between 5 and 9 times the generator
rated current.

The analysis of the short-circuit behavior of a SCIG during unsymmetrical faults is usually performed by means of digital simulations (Chen 1991, Samaan 2008).

Limited Variable-Speed Wind Turbines

The symmetrical short-circuit current of a limited-variable speed wind turbine with WRIG is shown in (Martinez 2011(b)). The high external rotor resistance causes the AC component of the stator current to decay rapidly. In this respect the short-circuit current of these wind turbines resembles the short-circuit current of DFIG wind turbines.

Variable-Speed Wind Turbines with DFIG

At the occurrence of a fault in the network, high stator and rotor current are induced in a DFIG. Theoretically, the RSC could be over-sized to handle the short-circuit current in the rotor but this would increase the overall cost for DFIG wind turbines and reduce the main advantage for DFIG systems compared to wind turbines connected to the network through a FSC. Therefore, the RSC switches must be blocked to avoid their damage. After blocking the RSC, there are different methods in which a DFIG wind turbine can be protected. A standard solution is blocking the RSC and at the same time short-circuiting the rotor circuit through an external resistance, called crowbar resistance (Akhmatov 2005, Morren 2007), see Figure 2.3.

Modern DFIG wind turbines can also be protected with only a DC chopper (Martinez 2011(a)), shown in Figure 2.3. At the event of a short-circuit, the RSC switches are blocked and the rotor current is led into the DC-link capacitor through the anti-parallel diodes of the RSC. A DC chopper is inserted to regulate the DC capacitor voltage. In this way the rotor circuit is rapidly demagnetized and the RSC can be re-started when the rotor current and DC-link voltage decrease below a certain value. For this configuration of the DFIG wind turbine, the anti-parallel diodes of the RSC must be over-sized to handle the short-circuit currents.

Both for a DFIG wind turbine with crowbar and with DC chopper protection, the fault current immediately after the fault is solely determined by the physical system and not by a specific control strategy. This allows carrying out analytical studies and drawing general conclusions on the delivered short-circuit current.

The short-circuit behavior of a DFIG wind turbine with crowbar protection depends on whether or not the crowbar is activated. During the time of

crowbar activation the control of the generator current is lost and the DFIG may be regarded as a SCIG, but with high rotor resistance, up to 20 times the value of the generator rotor resistance (Akhmatov 2005), and possibly high slip. Many papers have been published on the short-circuit current contribution of a DFIG but they confine their analysis to a solid symmetrical three-phase short-circuit at the generator terminals (Vicatos 1991, Morren 2007, Yang 2009, Pannell 2010). (Yang 2008, Rahimi 2010) analyze voltage dips of any magnitude but focusing on control issues and not on fault current contribution.

The high crowbar resistance causes the AC component of the symmetrical DFIG short-circuit current to decay much more rapidly as compared to a SCIG. After some periods, the short-circuit current of a DFIG is made up predominantly of a DC component. In (Morren 2007) it has been proposed to calculate the symmetrical short-circuit current of a DFIG in the same manner as done for a SCIG, but incrementing the value of the rotor resistance in the expression for the rotor transient time constant by the value of the crowbar resistance. Moreover, it has been suggested that the short-circuit current should be limited not only by the transient reactance, but by the sum of this with the crowbar resistance. As it will be shown in Chapter 3, these assumptions are still not enough for accurate DFIG short-circuit current calculation. In (Vicatos 1991, Pannell 2010), the symmetrical short-circuit current of a DFIG is obtained with the help of Laplace transformation. However, the analysis in (Vicatos 1991) is valid only under the assumption of small rotor resistance, which is not a valid assumption for a DFIG with crowbar. In (Pannell 2010) it is pointed out how in a DFIG, the frequencies of the decay components of the short-circuit current deviate from pure DC and rotor speed due to magnetic drag effects originating from the interaction between the stator and rotor fluxes. In these references the analysis is confined only to three-phase bolted short-circuits and, moreover, physical comprehension of the short-circuit process is not always straightforward from the pure mathematical treatment.

When the RSC is reconnected it controls the stator current and the DFIG may be looked at as a constant current source. The DFIG short-circuit behavior becomes then similar to that of a FSC (Walling 2009).

The fault current delivered by a DFIG wind turbine with DC chopper protection is seldom analyzed in the literature. Measurements under network faults are shown in (Engelhardt 2009), but a method to calculate the fault currents is not provided in that reference. In (Martinez 2011(a)), it has been proposed a theoretical analysis of the behavior of a DFIG with chopper

protection during symmetrical faults. The analysis results in the parameterization of a synchronous generator to represent a DFIG with chopper protection. The analysis proposed in (Martinez 2011(a)) is based on the assumption that during a symmetrical fault the DC-link capacitor and chopper can be represented simply as an equivalent resistance, whose value is chosen to be the resistance value of the chopper. In Chapter 4, it will be shown that for accurate short-circuit current prediction the value of the equivalent resistance has to be chosen depending on the initial loading of the generator and on the voltage dip magnitude.

An analysis of the DFIG behavior under unsymmetrical voltage dips is performed in (Lopez 2008(a)), though the authors focus not on the short-circuit current but instead on the rotor voltage of the DFIG under such conditions for control purposes. Unsymmetrical faults cause high rotor voltages in a DFIG, caused by the negative sequence in the grid. These voltages may be well above the control range of the RSC and, as a consequence, controllability of rotor current is lost. Moreover, since the negative sequence voltage does not decay, the crowbar must remain inserted and the RSC blocked for the whole duration of the fault (Seman 2006(b)).

Variable-Speed Wind Turbines with FSC

The short-circuit behavior of FSC wind turbines is mainly determined by the way the grid side converter is controlled and it is therefore specific to each particular commercial wind turbine (Walling 2009). However, in general, it can be said that the FSC limits the current fed into the fault to the nominal current rating of the converter or slightly above it. For severe faults, the switching of the converter may also be stopped during the fault period (Martinez 2011(b)).

2.3   Grid Fault Ride-Through Requirements

The basic way national grid codes specify the limiting conditions for a wind turbine to remain connected to the grid during a voltage dip, is by providing a curve where a voltage dip is given as a function of time. Voltage dips following a fault in the system and cleared under normal circumstances are expected to be above this curve. The duration of the voltage dip is dependent on the speed with which the protection system clears the fault. Since Transmission System Operators (TSOs) in different countries may have different protection philosophies, it follows that GFRT requirements are specific to each national grid code. The voltage-time curves from some European national grid codes are shown in Figure 2.5.
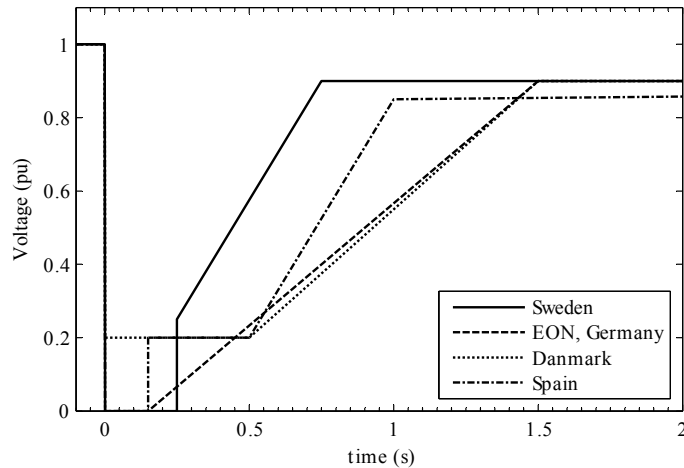
Figure 2.5   Voltage-time curves from GFRT requirements of some European national grid codes.

A process toward the harmonization of the European grid codes has started when Regulation (EC) 714/2009 assigned ENTSO-E, European Network of Transmission System Operators for Electricity, the role of developing the "*Network Code for Requirements for Grid Connection applicable to all Generators*".

A wind turbine is required to remain connected to the grid if the voltage at the Point of Common Coupling (PCC) during a fault always remains above the voltage-time curve given in the grid code. Note that in the case of the Swedish grid code, the voltage-time curve is applicable in the transmission network and, in general, not at the PCC. For wind turbines connected directly to the transmission network the Swedish GFRT curve is applicable at the PCC. Wind turbines connected below the transmission network must ride-through faults in the transmission network causing voltage dips at the connecting transmission network buses above the Swedish GFRT curve. In some cases, disconnection is allowed if followed by a fast re-synchronization within a few seconds, e.g. 2 seconds in E.ON grid code (E.ON 2006). Otherwise, the wind turbine is allowed to disconnect from the grid. Some grid codes may have an explicit requirement on recurring faults, i.e. a fault followed within a short period of time by another fault of the same type. In the case of the Danish grid code (Technical Regulation 3.2.5 2010), such a requirement exists for two single-phase-to-earth or two-phase faults following

each other within a time of 0.5 up to 3 s.

Remaining connected to the grid under the specified conditions is the basic GFRT requirement. Besides remaining connected, a wind turbine may also be required to provide reactive current support to the grid during the depressed voltage condition. The amount of reactive current to be injected in the grid is specified in the grid codes as a function of the voltage. E.ON grid code specifies that in case of a voltage dip, the reactive current injection must increase with at least 2 % per every 1 % voltage drop, i.e. rated reactive current must be delivered when the voltage falls below 50 % of rated value. This is combined with a deadband of +/- 10 % in voltage where the injection is zero. Voltage support must be continued for a further 500 ms after the voltage returns in the deadband. A similar reactive support scheme is also present in the Danish grid code, with the exception of the extra 500 ms voltage support. Spanish grid code only sets some limits on the consumed reactive power. In the case of a three-phase fault, this is allowed in the first 40 ms after the fault and in the first 80 ms after fault clearing and it cannot exceed 60 % of the nominal wind plant power rating (Leon-Martinez 2011). Swedish grid code does not have any requirement on reactive current injection during grid fault ride-through.

A requirement on active power ramp after fault clearing is also common in grid codes (Tsili 2009). E.ON grid code requires that wind turbines remaining connected during a fault have to recover their active power with a minimum gradient of 20 % rated power per second after fault clearance. Great Britain and Ireland grid codes state that active power must be restored to at least 90 % of its pre-fault value within 1 second after voltage restoration (Tsili 2009).

GFRT parts of grid codes imply a requirement not only for the technology, protection and control of the wind turbine, generator and power electronics, but also on the design and sizing of the wind plant auxiliary equipment. The Danish grid code requires for example that the hydraulic, pneumatic and emergency supply equipment in a wind plant must be designed so that continuous operation is assured for at least six different fault events at five minutes intervals.

The GFRT requirements also imply that the wind plant protection relays, e.g. the undervoltage relays, must be set so that they do not affect the GFRT capability of the wind plant.

GRFT requirements still represent a challenge for turbine manufacturers. In

the next sections, a brief overview on different solutions adopted to achieve GFRT capability is presented.

2.4   Grid Fault Ride-Through Solutions

In this section, a review is presented on the different strategies proposed in scientific literature to achieve grid fault ride-though capability of wind turbines, with particular emphasis given to the DFIG wind turbine.

Fixed-Speed Wind Turbines

A wind turbine with a SCIG will react to a fault in the grid by accelerating and drawing a large amount of reactive power when the grid voltage returns. Depending on the unbalance between input mechanical power and output electric power during the fault, the generator may accelerate beyond the critical speed and become unstable. In this case, disconnection and use of an emergency brake are necessary (Akhmatov 2005). The large amount of reactive power drawn by the SCIG after fault clearing may cause prolonged low voltages in the grid. This also contributes to generator over-speeding and may lead to instability of the SCIG and consequent disconnection (Nguyen 2010).

Generator over-speeding and voltage recovery are therefore the two main issues for GFRT of this type of wind turbines. To minimize generator over-speeding, pitch control is used to reduce the mechanical input power. Because of the limited speed of the pitch servo, this solution may however not be enough. Series connected dynamic braking resistors are proposed in (Causebrook 2007) to reduce generator over-speed and improve its stability. SVC or STATCOM are used in (Foster 2006, Molinas 2008) and shown to improve the post-fault voltage recovery of fixed-speed wind turbines. The performance of a STATCOM is shown to be superior to that of an SVC for improving stability of fixed-speed wind turbines.

Controlling nearby variable-speed wind turbines to help GFRT of fixed-speed wind turbines has been analyzed in (Luna 2008, Muyeen 2010). Variable-speed wind turbines can control the injection of reactive power during a fault and therefore support the voltage restoration after fault clearing.

Variable-Speed Wind Turbines with DFIG

The standard way to protect a DFIG wind turbine during a fault in the system is by blocking the RSC switching and inserting a crowbar resistance in the rotor circuit. Until some years ago, the crowbar resistance was inserted

through a thyristor switch, which made it impossible to disconnect the crowbar resistance before the rotor current had decayed to zero. This configuration of crowbar protection is named "passive crowbar". The DFIG wind turbine with passive crowbar is disconnected from the network some time after the short-circuit (Seman 2006(a), Bak-Jensen 2009).

Since it needs to be disconnected from the grid in the event of a fault, this DFIG configuration does not comply with the most recent GFRT requirements. By replacing the thyristor with a fully controllable switch, as for example an IGBT, the crowbar resistance can be disconnected before the rotor current has decayed to zero and even when the fault is still present. This configuration is called "active crowbar" (Seman 2006(b)). When the rotor current has decayed below a certain value, the active crowbar may be disconnected and the RSC may be re-started. In this way, the DFIG does not need to be disconnected from the network but can ride through the fault contributing to active and reactive power injection after the crowbar has been disconnected (Kayikci 2008, Salles 2009). When the crowbar is connected, pitch control is actuated to avoid over-speeding of the generator (Akhmatov 2005). During the period of crowbar activation, the DFIG will deliver active power if in a super-synchronous condition or will absorb active power if in a sub-synchronous condition (Kayikci 2008). In both cases it will absorb reactive power from the network and since its pre-fault slip may be far from zero the absorbed reactive power may be higher than that of a corresponding SCIG running almost at almost zero slip (Akhmatov 2005). The amount of absorbed reactive power may be reduced by properly choosing the value of the crowbar resistance (Hansen 2007(a)).

However, the crowbar alone may not be sufficient to achieve GFRT. After the fault, the DC-link voltage tends to increase due to the energy contribution from the rotor. A chopper resistance on the DC-link may be necessary to keep the DC-link capacitor voltage within an acceptable range (Erlich 2007). A similar solution is tested in (Engelhardt 2009), where it is found that even for the most serious faults in the network the DFIG is able to ride-through continuing its supply of reactive power, thanks to an advanced control scheme not fully described in the reference. The RSC would block only for solid three-phase faults at the generator terminals.

Some other approaches for the grid-fault ride through of a DFIG wind turbine proposed in the literature are discussed in the following. These approaches partly rely on extra hardware and partly on advanced control schemes.

(Petersson 2005(b)) proposes to dimension the RSC to handle the high transient rotor currents during the short-circuit. However, to avoid even higher transient rotor currents at fault clearing, it is proposed to disconnect the DFIG from the grid through anti-parallel thyristors, magnetize it through the RSC and re-connect it to the grid.

(Yang 2008) proposes the connection of a "series dynamic resistor" in series with the rotor circuit in the event of a fault. This resistor limits the rotor current as the crowbar resistor, but it does not require the RSC blocking, since it is connected in series with it.

(Xiang 2006, Lopez 2008(b)) point out how the high transient rotor currents are due to the natural stator flux, i.e. the flux trapped into the stator after a voltage dip. The authors of the references propose to use the RSC to quickly inject a current in the rotor counteracting the inducing stator natural flux, thus obtaining a rotor current decay faster than with the generator stator transient time constant. (Esandi 2009) proposes the simultaneous use of the demagnetizing current strategy and an extra resistance to be inserted in the stator circuit after fault occurrence. A non-linear control law for determining the reference rotor current, along with a current controller made up of a PI controller and a resonant controller, is proposed in (Rahimi 2010). (Lima 2010) proposes a new control scheme for the rotor current controller based on feeding back as reference to the controller the measured stator current. In this ways the controller synthesizes rotor currents equal in shape but opposite in phase with the stator currents, reducing both the stator and rotor currents.

A proposal for inserting a converter in series with the DFIG stator circuit is found in (Abdel-Baqi 2010, Flannery 2009). The series converter is used to inject a voltage at the generator terminals during symmetrical and unsymmetrical faults, to reduce the impact of the transient on the generator. A direct power control (DPC) method combined with a strategy for crowbar triggering is proposed in (Zhou 2008) and allows losing the DFIG controllability only for a short time. In (Martinez De Alegria 2004) a new control method for a DFIG, named Power Error Vector Control (PEVC), is briefly introduced. The authors show that the PEVC may also be used to improve the ride-through capability of the DFIG during symmetrical voltage dips, reducing the need of a crowbar only for very severe voltage dip.

Variable-Speed Wind Turbines with FSC

Being connected to the grid through a FSC, a voltage dip does not affect directly the generator dynamics in this type of wind turbines. The grid side

converter is able to ride-through and supply reactive current. A certain over-speeding of the generator is allowed to store part of the mechanical input power into kinetic energy. Pitch control is adopted to reduce the input mechanical power. During severe faults however, a chopper resistance is needed to dissipate the input power and keep the DC-link voltage within acceptable levels (Tsili 2009, Nguyen 2010).

A non-linear control technique is proposed in (Mullane 2005) to enhance the dynamic performance of the grid side converter and avoid temporary over-currents.

2.5   Summary

The most common commercial wind turbine technologies and the research done on the short-circuit behavior of these wind turbines have been introduced. Particular emphasis has been given to the DFIG wind turbine, partly because it has been the most common wind turbine type installed in the last decade. The DFIG wind turbine fault behavior is also the most apt to be studied analytically since, during the period the RSC is blocked, it is not influenced by a particular control law but merely by its physical system. This allows to draw general conclusions on the delivered short-circuit current. A brief review of the grid code requirements for GFRT from different countries has been done and solutions adopted for different wind turbine types to achieve GFRT have been presented.

Chapter 3

Fault Currents of SCIG and DFIG Wind Turbines

SCIG wind turbines are still common in the power system and DFIG wind turbines have been the most commonly installed wind turbine type during the last decade. The standard solution to protect a DFIG wind turbine during a fault is to block the RSC switching and insert a crowbar resistance in the rotor circuit. Knowledge of their fault current contribution is important when dealing with protection relay settings or power system component sizing. A thorough theoretical analysis of the fault current delivered by SCIG and DFIG wind turbines with crowbar protection is performed in this chapter. The mathematical derivation is accompanied by a simple physical explanation of the process going on inside the generator during a grid fault. The material presented in this chapter is based on Publication [1].

3.1   Introduction

Induction generators have a different short-circuit behavior when compared to synchronous generators and prediction of this behavior is an important issue in power system planning, transient stability analysis and protection setting studies.

In this chapter a general method for calculating the short-circuit current of a DFIG with crowbar resistance is proposed. For pedagogical purpose, the short-circuit current of a SCIG is calculated first. The method deals with both symmetrical and unsymmetrical faults and voltage dips of any magnitude at the generator terminals. It will be shown that the

simplifications done to derive the short-circuit current of a SCIG neglect some dynamics that become important when the rotor resistance is high, as is the case for a DFIG with crowbar protection. Therefore applying a short-circuit formula derived for a SCIG to predict the short-circuit current of a DFIG leads to inaccurate results.

The proposed method permits to predict the short-circuit currents as a function of time in the three phases of a SCIG or a DFIG by using an analytic expression, eliminating the need for dynamic simulations. The analytic expression can also be used to calculate the maximum phase currents for different faults, their DC and AC components, or it may be used to get an envelope of the currents if only their RMS value is needed. The results obtained with the proposed method are compared to those obtained through simulations using the well-established classic linear fifth order model of the induction machine (Vas 1992).

A main assumption made in this work is to neglect saturation of the induction machine reactances. This is certainly an approximation and will impact on the accuracy of the proposed method when compared to measurements on a real induction machine. Saturation of leakage reactances may increase the short-circuit current of an induction generator while main-flux saturation has little impact on the short-circuit current (Jabr 2007). A simple method to take into account the saturation of the leakage reactances is also exposed in (Jabr 2007) and could possibly be applied to the method proposed in this chapter. However, this is not done here since it is not within the primary scope of this work to investigate the effects of saturation on the short-circuit current of an induction generator.

3.2   Induction Generator Modelling

The induction generator dynamic equations are here presented in a stator reference frame using space-vector notation, as done in (Vas 1992). A three-phase voltage system may be expressed, with obvious meaning of the notation, as in Equation 3.1.

$$
\begin{aligned}
v_a(t) &= \hat{V}\cos(\omega t + \varphi) \\
v_b(t) &= \hat{V}\cos\left(\omega t + \varphi - \tfrac{2}{3}\pi\right) \\
v_c(t) &= \hat{V}\cos\left(\omega t + \varphi - \tfrac{4}{3}\pi\right)
\end{aligned}
\tag{3.1}
$$

The corresponding space-vector is calculated in Equation 3.2. Notice that the

amplitude of the defined voltage space-vector is equal to the peak amplitude of the instantaneous voltage and that V is a phasor:

$$\vec{v}_s(t) = \frac{2}{3}\left(v_a(t) + a v_b(t) + a^2 v_c(t)\right) = \hat{V}e^{j\varphi}e^{j\omega t} = Ve^{j\omega t} \tag{3.2}$$

where $a = e^{j\frac{2}{3}\pi}$, $a^2 = e^{-j\frac{2}{3}\pi}$, $V = \hat{V}e^{j\varphi}$.

The space-vectors are here indicated by an overlined arrow. The phasor V is defined in such a way that its magnitude is equal to the peak-value of the voltage. The first part of Equation 3.2 is valid also if the three-phase quantities do not form a balanced system. In this case, under the assumption that no zero-sequence is present, the space vector becomes (Vas 1992):

$$\vec{v}_s(t) = \hat{V}_1 e^{j\varphi_1}e^{j\omega t} + \hat{V}_2 e^{-j\varphi_2}e^{-j\omega t} = V_1 e^{j\omega t} + V_2 e^{-j\omega t} \tag{3.3}$$

Similar expressions can be obtained for currents and fluxes. The zero-sequence is not considered here, since commonly an induction generator is not grounded and therefore no zero-sequence current can flow. If no zero-sequence component is present, the instantaneous values of the currents in the three phases can be obtained from the corresponding space-vector as (Vas 1992):

$$
\begin{aligned}
i_a(t) &= \mathrm{Re}\!\left(\vec{i}_s\right) \\
i_b(t) &= \mathrm{Re}\!\left(a^2 \vec{i}_s\right) \\
i_c(t) &= \mathrm{Re}\!\left(a \vec{i}_s\right)
\end{aligned}
\tag{3.4}
$$

Using the introduced space-vector notation and using a stationary reference frame, the equations describing the electrical dynamics of a squirrel-cage induction machine are given by Equation 3.5 and Equation 3.6 (Vas 1992).

$$
\begin{aligned}
\vec{v}_s &= R_s \vec{i}_s + \frac{d\vec{\psi}_s}{dt} \\
0 &= R_r \vec{i}_r + \frac{d\vec{\psi}_r}{dt} - j\omega_r \vec{\psi}_r
\end{aligned}
\tag{3.5}
$$

$$
\begin{aligned}
\vec{\psi}_s &= L_s \vec{i}_s + L_m \vec{i}_r \\
\vec{\psi}_r &= L_m \vec{i}_s + L_r \vec{i}_r
\end{aligned}
\tag{3.6}
$$

where $L_s = L_{sl} + L_m$ and $L_r = L_{rl} + L_m$.

3.3   SCIG Short-Circuit Current

The short-circuit current will be calculated under the following assumptions:
a) before the occurrence of the fault balanced conditions are present in the
network; b) the generator is assumed to run at no-load and to be lossless,
which results in zero slip; c) the generator speed does not change after the
short-circuit; d) the generator is connected to a strong network, so that the
post-fault voltage is not influenced by its short-circuit current e) the generator
is linear, i.e. it does not saturate. Linearity of the induction generator allows
to use the superposition principle to find out the total short-circuit current as
sum of different components. The above assumptions mean that the short-
circuit current calculated with the method exposed in this chapter is an
approximation of the short-circuit current delivered by a real machine.

The short-circuit current of a SCIG is made up of three components. The
first component is due to the post-fault steady state voltage at the generator
terminals which may be symmetrical as well as unsymmetrical. We will refer
to this component as the forced short-circuit current component. The second
component is due to the natural stator flux and the third component is due to
the natural rotor flux. The natural stator and rotor fluxes arise just after the
fault to assure the continuity of the stator and rotor fluxes before and after
fault inception, according to the constant flux linkage theorem (Kimbark
1968). In a SCIG, these components decay exponentially with time constants
that depend upon the generator parameters (Kovaks 1984). The terms
"forced" and "natural" are used, as done in (Lopez 2008(a)).

Once the post-fault transient stator and rotor fluxes are known, the short-
circuit current can be calculated by solving Equation 3.6 with respect to the
stator current.

Post-fault Stator Flux

The stator flux is made up of a forced component and of a natural
component. In turn, the forced component is due to the contribution of the
positive and the negative sequences of the post-fault voltage. Therefore the
stator flux after fault occurrence can be expressed as in Equation 3.7.

$$\vec{\psi}_s(t) = \vec{\psi}_{sf,1}(t) + \vec{\psi}_{sf,2}(t) + \vec{\psi}_{sn}(t) \tag{3.7}$$

The pre-fault flux and the post-fault positive and negative sequence forced flux components in a stator reference frame can be derived from Equation 3.5 neglecting the stator resistance:

$$\bar{\psi}_{s,pre} = \frac{\bar{v}_{pre}}{j\omega_s} = \frac{\hat{V}_{pre}e^{j\varphi_{pre}}e^{j\omega_s t}}{j\omega_s} = \frac{V_{pre}}{j\omega_s}e^{j\omega_s t} \tag{3.8}$$

$$\bar{\psi}_{sf,1} = \frac{\bar{v}_1}{j\omega_s} = \frac{\hat{V}_1 e^{j\varphi_1}e^{j\omega_s t}}{j\omega_s} = \frac{V_1}{j\omega_s}e^{j\omega_s t} \tag{3.9}$$

$$\bar{\psi}_{sf,2} = \frac{\bar{v}_2}{-j\omega_s} = \frac{\hat{V}_2 e^{-j\varphi_2}e^{-j\omega_s t}}{-j\omega_s} = \frac{V_2}{-j\omega_s}e^{-j\omega_s t} \tag{3.10}$$

Negative sequence quantities rotate with a frequency of $-\omega_s$ in a stator reference frame.

Next, the natural component of the stator flux must be found. In general, for any kind of fault, because of the constant flux linkage theorem, the natural flux just after the fault is given by the difference between the stator forced flux components immediately before and after the fault, as in Equation 3.11. The natural stator flux is actually not constant because of the presence of the stator resistance, but decays with a time constant given by Equation 3.12, (Kovaks 1984, Vas 1992, Jenkins 2000), which is valid under the assumption that the rotor resistance is small, as it will be shown later. By combining Equations 3.7-3.11 and taking into account that the natural stator flux decays with time constant T_s, the total stator flux after fault occurrence is given by Equation 3.13.

$$\bar{\psi}_{sn}(0) = \psi_{sn} = \bar{\psi}_{s,pre}(0^-) - \left(\bar{\psi}_{sf,1}(0^+) + \bar{\psi}_{sf,2}(0^+)\right) = \frac{V_{pre}}{j\omega_s} - \left(\frac{V_1}{j\omega_s} + \frac{V_2}{-j\omega_s}\right) \tag{3.11}$$

$$T_s = \frac{L_s'}{R_s} = \frac{L_s - \dfrac{L_m^2}{L_r}}{R_s} \tag{3.12}$$

$$\bar{\psi}_s(t) = \frac{V_1}{j\omega_s}e^{j\omega_s t} + \frac{V_2}{-j\omega_s}e^{-j\omega_s t} + \left(\frac{V_{pre}}{j\omega_s} - \left(\frac{V_1}{j\omega_s} + \frac{V_2}{-j\omega_s}\right)\right)e^{-\frac{t}{T_s}} \tag{3.13}$$

Post-fault Rotor Flux

The post-fault rotor flux is the sum of three components:

$$\bar{\psi}_r(t) = \bar{\psi}_{rf,1}(t) + \bar{\psi}_{rf,2}(t) + \bar{\psi}_{rn}(t) \tag{3.14}$$

With the assumption of zero slip, the positive sequence rotor current is zero, see Figure 3.1, and the pre- and post-fault positive sequence rotor fluxes are given in Equation 3.15 (Morren 2007), where $k_s = L_m/L_s$.

$$\bar{\psi}_{r,pre} = \frac{L_m}{L_s}\bar{\psi}_{s,pre} = k_s\bar{\psi}_{s,pre} = k_s\frac{V_{pre}}{j\omega_s}e^{j\omega_s t}$$

$$\bar{\psi}_{rf,1} = \frac{L_m}{L_s}\bar{\psi}_{sf,1} = k_s\bar{\psi}_{sf,1} = k_s\frac{V_1}{j\omega_s}e^{j\omega_s t} \tag{3.15}$$
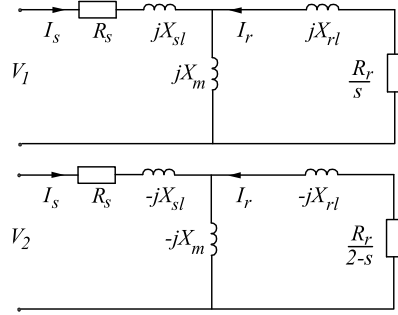
Figure 3.1   Positive and negative sequence equivalent circuits of a SCIG. These are also applicable to a DFIG with rotor windings connected to a crowbar resistance, if R_r is replaced by $R_r + R_{cr}$.

The negative sequence forced rotor flux can be found by first expressing the negative sequence stator and rotor currents. With reference to Figure 3.1, the stator negative sequence current is given by Equation 3.16, where both the stator and rotor resistances have been neglected.

$$\bar{i}_{s,2} = \frac{\bar{v}_2}{Z_2} \approx \frac{\bar{v}_2}{-j\omega_s\left(L_{sl} + \dfrac{L_m L_{rl}}{L_r}\right)} \tag{3.16}$$

The minus sign in front of the reactances is due to the fact that a negative sequence voltage induces a flux whose direction of rotation is opposite to that of a positive sequence induced flux. This is also the reason why the rotor resistance is divided by the negative sequence slip *2-s* in Figure 3.1 (Anderson 1995). The negative sequence rotor current can be found by a simple current division between the rotor and the magnetizing branch:

$$\vec{i}_{r,2} \approx -\frac{-j\omega_s L_m}{-j\omega_s L_m - j\omega_s L_{rl}}\vec{i}_{s,2} = -\frac{L_m}{L_r}\vec{i}_{s,2} \tag{3.17}$$

Finally, by inserting the negative sequence stator and rotor currents into Equation 3.6 leads to Equation 3.18.

$$\vec{\psi}_{rf,2} = L_m\vec{i}_{s,2} + L_r\vec{i}_{r,2} \approx 0 \tag{3.18}$$

This result indicates that for a SCIG the negative sequence forced rotor flux can be neglected.

The natural rotor flux is the flux trapped in the rotor circuit at fault occurrence. Its magnitude and phase immediately after the fault are found as in Equation 3.19.

$$\vec{\psi}_{rn}(0) = \psi_{rn} = \vec{\psi}_{r,pre}\left(0^-\right) - \left(\vec{\psi}_{rf,1}\left(0^+\right) + \vec{\psi}_{rf,2}\left(0^+\right)\right) = k_s\left(\frac{V_{pre}}{j\omega_s} - \frac{V_1}{j\omega_s}\right) \tag{3.19}$$

This flux is fixed with the rotor circuit, i.e. it rotates with the rotor speed in a stator reference frame (Morren 2007). In a rotor reference frame, it is a DC component decaying exponentially with time constant T_r, defined in Equation 3.20 (Morren 2007). The expressions for the inductances in Equations 3.12 and 3.20 can easily be derived by considering the induction generator equivalent circuit in Figure 3.1 or using Equations 3.5 and 3.6. See also (Vas 1992, Morren 2007).

$$T_r = \frac{L_r'}{R_r} = \frac{L_r - \frac{L_m^2}{L_s}}{R_r} \tag{3.20}$$

Summarizing what has been found in this section, the transient rotor flux for a SCIG in a stator reference frame is given as

$$\vec{\psi}_r(t) = k_s \frac{V_1}{j\omega_s} e^{j\omega_s t} + k_s \left(\frac{V_{pre}}{j\omega_s} - \frac{V_1}{j\omega_s} \right) e^{j\omega_r t} e^{-\frac{t}{T_r}} \qquad (3.21)$$

Short-Circuit Current of a SCIG

The post-fault stator and rotor fluxes are given by Equations 3.13 and 3.21. Solving Equation 3.6, the relation between fluxes and stator current is given by Equation 3.22, (Vas 1992, Morren 2007), where $k_r = L_m/L_r$.

$$\vec{i}_s = \frac{\vec{\psi}_s}{L'_s} - \frac{L_m}{L_r} \frac{\vec{\psi}_r}{L'_s} = \frac{\vec{\psi}_s}{L'_s} - k_r \frac{\vec{\psi}_r}{L'_s} \qquad (3.22)$$

Substitution of Equations 3.13 and 3.21 into 3.22 gives the final general approximate expression for the short-circuit current of a SCIG, reported in Equation 3.23.

$$\vec{i}_s = \frac{V_1}{j\omega_s L'_s} (1 - k_s k_r) e^{j\omega_s t} + \frac{V_2}{-j\omega_s L'_s} e^{-j\omega_s t} + \left(\frac{V_{pre} - (V_1 - V_2)}{j\omega_s L'_s} \right) e^{-\frac{t}{T_s}} - k_s k_r \left(\frac{V_{pre} - V_1}{j\omega_s L'_s} \right) e^{j\omega_r t} e^{-\frac{t}{T_r}}$$

$$(3.23)$$

This equation is valid under any symmetrical or unsymmetrical fault in the network. If the network and step-up transformer inductances cannot be neglected they need to be added in series with the generator stator leakage inductance in all the previous equations. To get the currents in the three phases of the induction generator it suffices now to apply Equation 3.4.

3.4   SCIG Simulation Results

The network of Figure 3.2 has been modelled in MATLAB SimPowerSystems (MATLAB R2009b). The induction generator is considered linear, without saturation, and it is connected to the network directly, without a step-up transformer. The network voltage is 575 V and the pu generator parameters are reported in Table 3.1. To comply with the assumption made above of constant rotor speed during the fault, a high inertia constant has been defined for the generator. The generator initial slip is close to zero and the generator remains unloaded during the fault. A time-step of 5 microseconds has been used in all simulations. The network reactance X_{th} is assumed equal to one hundredth of the generator base impedance and the ratio X_{th}/R_{th} is assumed equal to 10. Different kinds of faults have been simulated with different values for the parameter p.
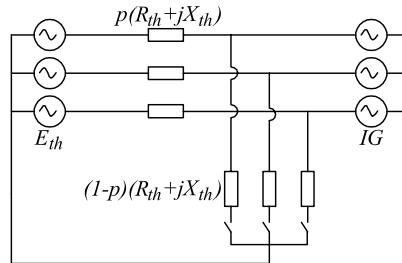
Figure 3.2   Network diagram used for the simulations. By varying the parameter p, the voltage dip magnitude at the generator terminals during the fault can be changed.

Table 3.1 Induction generator parameters

S_N (MVA)	1717
V_N (V)	575
R_s (pu)	0.0073
R_r (pu)	0.0052
L_{sl} (pu)	0.1766
L_{rl} (pu)	0.1610
L_m (pu)	3

Simulation results show that the proposed method for calculating the short-circuit currents gives accurate prediction of all phase currents under both symmetrical and unsymmetrical faults in the network. Figure 3.3 and Figure 3.4 show the calculated and simulated short-circuit currents in the case of a three-phase and of a phase-b to phase-c short-circuit with two different values of the parameter p. The calculated and simulated currents are practically indistinguishable.
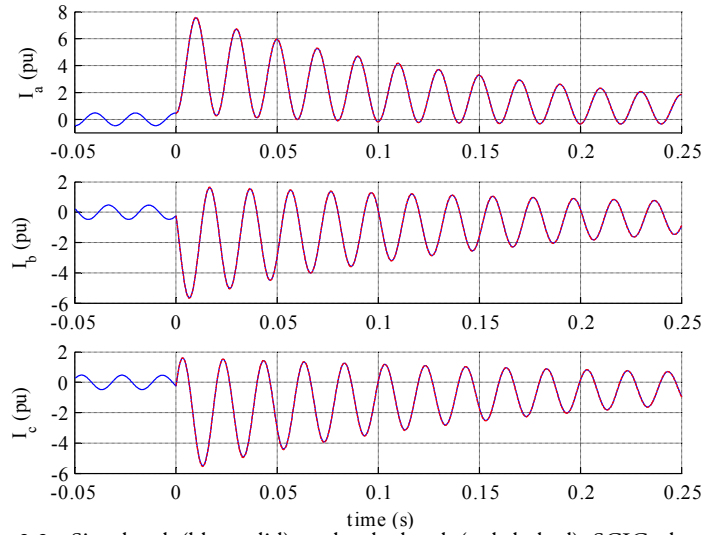
Figure 3.3   Simulated (blue-solid) and calculated (red-dashed) SCIG short-circuit current for a three-phase-phase fault, with parameter *p=1*. SCIG initially unloaded. Pre-fault voltage angle $\varphi = 90^o$.

Figure 3.4   Simulated (blue-solid) and calculated (red-dashed) SCIG short-circuit current for a phase-phase (*b-c*) fault, with parameter *p=0.85*. SCIG initially unloaded. Pre-fault voltage angle $\varphi = 45^o$.

3.5   DFIG Short-Circuit Current

A DFIG using crowbar protection is considered in this section. The analysis assumes that the crowbar remains connected during the whole duration of the fault, 250 ms in this study. This may not be the case for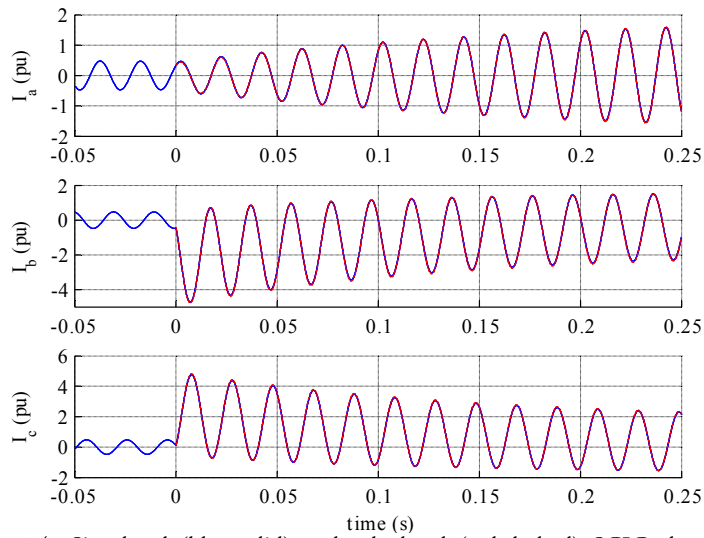 three-phase faults since the RSC would be re-started as soon as the rotor current decays below a certain predefined value. During symmetrical faults, the analysis here presented is therefore applicable during the period between crowbar insertion and RSC re-starting. However, for unsymmetrical faults, the RSC will most likely not be re-started during the fault since the cause of high rotor current is the negative sequence network voltage which does not decay during the fault period (Semaan 2006(b)). For the most severe unsymmetrical faults, the proposed analysis is therefore applicable during the whole duration of the fault.

The method proposed above for calculating the short-circuit current of a SCIG cannot be directly applied to a wind turbine driven DFIG, because of mainly two reasons.

The first reason is that the value of the crowbar resistance may be up to 20 times the value of the generator rotor resistance (Akhmatov 2005) and the total resulting rotor resistance can no longer be neglected. In (Morren 2007) it has been proposed a method for calculating the maximum short-circuit current of a DFIG with high crowbar resistance during a symmetrical three-phase fault at the generator terminals. The authors of the mentioned reference proposed to include the effects of the crowbar resistance to calculate the maximum short-circuit current of a DFIG in two steps. First, the rotor transient time constant is modified according to

$$T_{r,DFIG} = \frac{L_r^{'}}{R_r + R_{cr}} = \frac{L_r^{'}}{R_{r,tot}} \tag{3.24}$$

The second step to account for the presence of the high crowbar resistance proposed in (Morren 2007) is to include it in the impedance limiting the short-circuit current. Thus in Equation 3.23, one should use $R_{r,tot} + j\omega_s L_s^{'}$ instead of $j\omega_s L_s^{'}$, where $R_{r,tot}$ indicates the sum of the rotor and crowbar resistance. However, this proved to be still a too rough approximation when comparing with the simulations, leading to inaccurate calculations of the DFIG short-circuit current as a function of time.

The second reason, that makes the SCIG short-circuit current calculation

method inaccurate when applied to a wind turbine driven DFIG, is that a wind turbine driven DFIG may operate in a slip range between -0.3 and +0.3. The forced stator and rotor fluxes, which for the SCIG have been calculated based on the assumption of zero slip, for a DFIG should be calculated based on its initial rotor speed and delivered active and reactive power.

Influence of high crowbar resistance on natural stator flux

Let us start with the stator transient time constant. In papers dealing with the DFIG short-circuit current (Morren 2007, Yang 2009), the DFIG stator transient time constant is still assumed to be equal to the one in Equation 3.12. However, for a DFIG with high total rotor resistance, the stator transient time constant needs to be expressed in a slightly different way. The natural stator flux, which is fixed with respect to the stator, generates a voltage in the rotor whose frequency and magnitude in a rotor reference frame are proportional to the rotor speed. A current will flow in the rotor, having the same frequency of the induced voltage and opposite to the rotor speed. The stator and rotor current due to the natural stator flux have the form $Ie^{-j\omega_r t}e^{-t/T_{s,DFIG}}$ when expressed in a rotor reference frame. $T_{s,DFIG}$ is the stator transient time constant for a DFIG and is defined below. By deriving this expression and neglecting the term proportional to $1/T_{s,DFIG}$, which for a typical induction machine is much smaller than ω_r, the voltage drop over an inductance L can be expressed as $-j\omega_r LIe^{-j\omega_r t}e^{-t/T_{s,DFIG}}$. With reference to the equivalent circuit in Figure 3.1, a simple current division therefore still holds between the rotor and magnetizing branch and the rotor natural current in a rotor reference frame is:

$$\vec{i}_{rn} = -\frac{-j\omega_r L_m}{R_{r,tot} - j\omega_r L_r}\vec{i}_{sn} \tag{3.25}$$

Substituting in Equation 3.6, leads to 3.26. The term L_{sn}' can be regarded as a complex operator that gives the relation between the natural stator flux and current. A similar concept, named operator inductivity, is introduced in (Kovaks 1984) when dealing with the short-circuit behavior of a synchronous generator.

$$\vec{\psi}_{sn} = \left(L_s - \frac{-j\omega_r L_m^2}{R_{r,tot} - j\omega_r L_r} \right)\vec{i}_{sn} = L_{sn}'\vec{i}_{sn} \tag{3.26}$$

L_{sn}' is a modification of the inductance L_s' in Equation 3.12 and coincides with it if the total rotor resistance is negligible. Therefore the stator transient time constant of a DFIG with high rotor resistance is given in Equation 3.27. This means that the natural stator flux is no longer fixed with respect to the stator, but it is actually slowly rotating because of the presence of a high rotor resistance.

$$T_{s,DFIG} = \frac{L_{sn}'}{R_s} = \frac{\left(L_s - \frac{-j\omega_r L_m^2}{R_{r,tot} - j\omega_r L_r}\right)}{R_s} \tag{3.27}$$

Influence of high crowbar resistance on natural rotor flux

Let us denote the natural rotor flux immediately after the fault as ψ_{rn}. In the SCIG case, this flux in a rotor reference frame is a DC component decaying with the rotor transient time constant. This fact is no longer true for a DFIG with high rotor resistance. To explain why this no longer holds, we may find it useful to refer to a simpler analogous situation. Consider a short-circuited coil with certain resistance R and inductance L. At a certain point, an alternating flux $\psi_m(t)$ with frequency ω is induced in the coil. The coil may have an initial flux, ψ_0.

This situation is analogous to that of a DFIG with a non negligible rotor resistance under a sudden transient. The coil corresponds to the DFIG closed rotor circuit, while the external flux $\psi_m(t)$ would correspond to the natural stator flux of the DFIG.

The external flux will induce a voltage in the coil and this will result in an alternating current component, opposing the inducing flux:

$$i_{ac}(t) = \frac{v_m(t)}{R + j\omega L} = \frac{-j\omega M\psi_m e^{j\omega t}}{R + j\omega L} \tag{3.28}$$

M tells how much of the external flux is linked by the coil. A DC current component depending on the initial flux of the coil and decaying exponentially will also flow in the coil:

$$i_{dc}(t) = c_{coil}\frac{\psi_0}{L}e^{-t/(L/R)} \tag{3.29}$$

The meaning of the constant c_{coil} is that only a fraction of the initial flux ψ_0 is due to the DC current component i_{dc} in the coil. The remaining part of the initial flux ψ_0 is due to the AC current component i_{ac} and the external flux linkage with the coil. The total flux linkage with the coil will therefore be given by Equation 3.30.

$$\psi(t) = M\psi_m e^{j\omega t} + Li_{ac}(t) + Li_{dc}(t) = \left(1 - \frac{j\omega L}{R + j\omega L}\right)M\psi_m e^{j\omega t} + c_{coil}\psi_0 e^{-t/(L/R)} \quad (3.30)$$

Without the coil resistance, the AC current component in the coil would completely counteract the inducing flux, and only a DC flux would be present in the coil. This ideal situation is close to what happens in the short-circuited rotor of a SCIG during a transient, with the natural rotor flux being almost a pure DC component decaying with the rotor transient time constant. However, when the coil resistance in not negligible, the induced AC current component does not completely counteract the inducing flux. This is due to the fact that the AC current component magnitude decreases and that it acquires a phase difference with the inducing flux. As a result the total coil flux will be composed of an AC component and a DC component. The coefficient c_{coil} tells how big the DC flux component in comparison to the total coil flux is. This situation is analogous to what happens in the rotor circuit of a DFIG with high crowbar resistance. In this case the natural rotor flux can no longer be considered a pure decaying DC component.

To find out the value of the constant c_{coil}, we can refer to the constant flux linkage theorem which says that the coil flux cannot change instantaneously. Therefore it must hold that:

$$\left(1 - \frac{j\omega L}{R + j\omega L}\right)M\psi_m + c_{coil}\psi_0 = (d_{coil} + c_{coil})\psi_0 = \psi_0$$

$$d_{coil} = \left(1 - \frac{j\omega L}{R + j\omega L}\right)\frac{M\psi_m}{\psi_0} \quad (3.31)$$

$$c_{coil} = 1 - d_{coil}$$

These results can now be translated to the case of a DFIG with high crowbar resistance to find out the natural rotor flux as a function of time. In this case, the external inducing flux is the natural stator flux and the initial coil flux is the post-fault natural rotor flux ψ_{rn}. Neglecting its slow rotation as found in Equation 3.27, the natural stator flux induces in the rotor circuit a voltage

whose frequency is proportional to the electrical rotor speed with the opposite sign. The total equivalent inductance seen from the rotor circuit is given by the series connection of the rotor leakage inductance and the parallel connection between the magnetizing and the stator leakage inductance. By analogy with the coil example, we can conclude that the coefficients c and d for the DFIG are given as in Equation 3.32, where "//" denotes the parallel operator. It has been assumed that all the natural stator flux links the rotor, i.e. corresponding to M in Equation 3.28 being equal to 1.

$$d = \left(1 - \frac{-j\omega_r\left(L_{rl} + L_m \,//\, L_{sl}\right)}{R_{r,tot} - j\omega_r\left(L_{rl} + L_m \,//\, L_{sl}\right)}\right)\frac{\psi_{sn}}{\psi_{rn}}$$

$$c = 1 - d$$

(3.32)

The coefficients c and d depend on the ratio between the initial natural stator and rotor fluxes and therefore vary for different fault conditions. Similar results can be derived by solving the DFIG differential equations in the case of a three-phase short-circuit at the generator terminals. The AC part of the natural rotor flux in a rotor reference frame, which depends on the inducing natural stator flux, will decay with the same time constant $T_{s,DFIG}$ as the natural stator flux. The DC natural rotor flux component, fixed with the rotor circuit, will decay with the rotor transient time constant $T_{r,DFIG}$.

We can now express the natural rotor flux as a function of time in a stator reference frame:

$$\bar{\psi}_{rn}(t) = \left(d e^{-t/T_{s,DFIG}} + c e^{-t/T_{r,DFIG}} e^{j\omega_r t}\right)\psi_{rn}$$

(3.33)

The initial natural rotor flux ψ_{rn} for a DFIG with high crowbar resistance will be calculated later in this section. The natural stator flux is not significantly affected by the rotor resistance value, therefore we can continue to use the value calculated for a SCIG in Equation 3.11 also in the case of a DFIG with a high crowbar resistance.

Influence of high crowbar resistance on negative sequence fluxes

The rotor negative sequence current can be obtained with a simple current division between the magnetizing and the rotor circuit branches, as done for a SCIG:

$$\vec{i}_{r,2} = -\frac{-j\omega_s L_m}{\dfrac{R_{r,tot}}{2-s} - j\omega_s L_r}\vec{i}_{s,2} = -\frac{-j\omega_s L_m}{\dfrac{R_{r,tot}}{2-s} - j\omega_s L_r}\frac{\vec{v}_2}{Z_2} \tag{3.34}$$

where Z_2 is the total negative sequence impedance of the generator, which can be calculated from the equivalent circuit in Figure 3.1. By substituting into Equation 3.6, the rotor negative sequence flux can be expressed as in 3.35.

$$\vec{\psi}_{rf,2} = L_m \vec{i}_{s,2} + L_r \vec{i}_{r,2} = \left(L_m + \frac{j\omega_s L_m L_r}{\dfrac{R_{r,tot}}{2-s} - j\omega_s L_r}\right)\vec{i}_{s,2} = L_{r2}\vec{i}_{s,2} = L_{r2}\frac{\vec{v}_2}{Z_2} \tag{3.35}$$

L_{r2} gives the relation between the rotor negative sequence flux and the stator negative sequence current and it is equal to zero, as expected, if the rotor resistance is zero.

The negative sequence stator flux is still given by Equation 3.10. However, proceeding as for the rotor flux, it can also be expressed as in 3.36.

$$\vec{\psi}_{sf,2} = \left(L_s + \frac{j\omega_s L_m^2}{\dfrac{R_{r,tot}}{2-s} - j\omega_s L_r}\right)\vec{i}_{s,2} = L_{s2}\vec{i}_{s,2} \approx \frac{Z_2}{-j\omega_s}\vec{i}_{s,2} = \frac{\vec{v}_2}{-j\omega_s} \tag{3.36}$$

Total rotor transient flux

The rotor forced flux must now include the part due to the negative sequence network voltage and it is given as:

$$\vec{\psi}_{rf} = k_s \frac{V_1}{j\omega_s}e^{j\omega_s t} + L_{r2}\frac{V_2}{Z_2}e^{-j\omega_s t} \tag{3.37}$$

Therefore the natural rotor flux, given by the difference of the pre- and post-fault forced fluxes at $t=0$, becomes

$$\vec{\psi}_{rn}(0) = \psi_{rn} = k_s \frac{V_{s,pre}}{j\omega_s} - \left(k_s \frac{V_1}{j\omega_s} + L_{r2}\frac{V_2}{Z_2}\right) \tag{3.38}$$

Taking into account what has been said for the natural rotor flux with Equation 3.33, the total rotor transient flux is finally calculated as in 3.39.

$$\vec{\psi}_r(t) = k_s \frac{V_1}{j\omega_s} e^{j\omega_s t} + L_{r2} \frac{V_2}{Z_2} e^{-j\omega_s t} + \left(de^{-t/T_{s,DFIG}} + ce^{-t/T_{r,DFIG}} e^{j\omega_r t} \right)\left(k_s \frac{V_{pre}}{j\omega_s} - \left(k_s \frac{V_1}{j\omega_s} + L_{r2} \frac{V_2}{Z_2} \right) \right)$$

(3.39)

Wind turbine driven DFIG

The initial slip of a wind turbine driven DFIG may be significantly different from zero, thus the initial and post-fault forced components of the rotor flux can no longer be calculated under the assumption of zero rotor current, as done for example in Equations 3.15, 3.37 and 3.38. With reference to the positive sequence equivalent circuit of the DFIG in Figure 3.1, the positive sequence forced component of the post-fault rotor flux can be calculated using 3.6 as in 3.40, where Z_1 is the DFIG positive sequence impedance.

$$\vec{i}_{s,1} = \frac{\vec{v}_1}{Z_1}, \qquad \vec{i}_{r,1} = -\frac{j\omega_s L_m}{\dfrac{R_{r,tot}}{s} + j\omega_s L_r} \vec{i}_{s,1}$$

$$s \neq 0: \quad \vec{\psi}_{rf,1} = \left(L_m - \frac{j\omega_s L_m L_r}{\dfrac{R_{r,tot}}{s} + j\omega_s L_r} \right) \vec{i}_{s,1} = \psi_{rf,1} e^{j\omega_s t}$$

(3.40)

$$s = 0: \quad \vec{\psi}_{rf,1} = k_s \vec{\psi}_{sf,1} = k_s \frac{\vec{v}_1}{j\omega_s} = \psi_{rf,1} e^{j\omega_s t}$$

The pre-fault rotor flux must also be re-calculated taking into account the initial conditions of the DFIG. If the initial apparent power, fed into the grid according to generator convention, and rotor slip of the DFIG are known, the pre-fault rotor flux is calculated, using Equation 3.6, as:

$$\vec{i}_{s,pre} = -\frac{S_{pre}^*}{3\vec{v}_{pre}^*}, \qquad \vec{\psi}_{s,pre} \approx \frac{\vec{v}_{pre}}{j\omega_s}, \qquad \vec{i}_{r,pre} = \frac{\vec{\psi}_{s,pre} - L_s \vec{i}_{s,pre}}{L_m}$$

$$\vec{\psi}_{r,pre} = \frac{L_r L_s - L_m^2}{L_m} \frac{S_{pre}^*}{3\vec{v}_{pre}^*} + \frac{L_r}{L_m} \frac{\vec{v}_{pre}}{j\omega_s} = \psi_{r,pre} e^{j\omega_s t}$$

(3.41)

where "*" denotes the complex conjugate.

The negative sequence forced rotor flux component is unchanged with respect to what we found previously in 3.35. Therefore, the total rotor flux equation for a wind-driven DFIG is finally given by Equation 3.42, which is a modification of 3.39, where $\psi_{rf,1}$ depends on the initial slip according to 3.40.

$$\vec{\psi}_r(t) = \psi_{rf,1}e^{j\omega_s t} + L_{r2}\frac{V_2}{Z_2}e^{-j\omega_s t} + \left(de^{-t/T_{s,DFIG}} + ce^{-t/T_{r,DFIG}}e^{j\omega_r t}\right)\left(\psi_{r,pre} - \left(\psi_{rf,1} + L_{r2}\frac{V_2}{Z_2}\right)\right) \quad (3.42)$$

No modifications are needed for the stator flux, which is still given by 3.13 with the substitution of T_s with $T_{s,DFIG}$. The stator and rotor fluxes can now be substituted into Equation 3.22, leading to the final expression, 3.43, for the short-circuit current of a wind turbine driven DFIG using crowbar resistance as a protection means during network faults. Equation 3.43 can be easily implemented in a programming language or a spreadsheet program and used to get an approximate prediction for the DFIG short-circuit currents.

$$\vec{i}_{sf}(t) = \left(\frac{V_1}{j\omega_s L_s'} - k_r\frac{\psi_{rf,1}}{L_s'}\right)e^{j\omega_s t} + \left(\frac{L_{s2}}{L_s'} - k_r\frac{L_{r2}}{L_s'}\right)\frac{V_2}{Z_2}e^{-j\omega_s t} = \left(\frac{V_1}{j\omega_s L_s'} - k_r\frac{\psi_{rf,1}}{L_s'}\right)e^{j\omega_s t} + \frac{V_2}{Z_2}e^{-j\omega_s t}$$

$$\vec{i}_{sn}(t) = \frac{V_{pre} - (V_1 - V_2)}{j\omega_s L_s'}e^{-t/T_{s,DFIG}} - \frac{k_r}{L_s'}\left(de^{-t/T_{s,DFIG}} + ce^{-t/T_{r,DFIG}}e^{j\omega_r t}\right)\left(\psi_{r,pre} - \left(\psi_{rf,1} + L_{r2}\frac{V_2}{Z_2}\right)\right)$$

$$\vec{i}_s(t) = \vec{i}_{sf}(t) + \vec{i}_{sn}(t)$$

$$(3.43)$$

3.6   DFIG Simulation Results

In this section, results from simulations in SymPowerSystems (MATLAB R2009b) are shown in order to validate the theoretical analysis presented in the previous paragraphs. A wind turbine using a DFIG model available in the standard library of SimPowerSystems has been used. A detailed description of the DFIG controllers can be found in (Miller 2003). The parameters for the DFIG are according to Table 3.1. Also from the same reference, the inertia constants for the wind turbine and the generator have now been assumed equal to 4.32 s and 0.62 s respectively. This model has been modified by including a crowbar protection. The crowbar resistance is considered to be 20 times the DFIG rotor resistance and is connected to the rotor circuit through a six-pulse diode bridge and a switch. After crowbar insertion, the RSC is blocked. The crowbar remains inserted during the whole duration of the simulated period, i.e. 250 ms. Typical times for RSC blocking may be lower than a few ms (Akhmatov 2005, Pannell 2005). The crowbar insertion time

in the simulations has been varied, to investigate its influence on the short-circuit current of the DFIG. For sake of clarity the currents before fault occurrence are not shown, as was instead done in Figure 3.3 and Figure 3.4.

DFIG directly connected to the network

The DFIG wind turbine has been connected directly to the network as shown in Figure 3.2, without a step-up transformer. In Figure 3.5, Figure 3.6, Figure 3.7, the results from different short-circuits in the network are reported. The simulated short-circuit current delivered by the DFIG is compared to the one predicted with Equation 3.43. It can be noticed that the proposed method is capable of accurately reproducing the wind turbine driven DFIG short-circuit current, if the crowbar is ideally inserted at the moment of fault inception. Errors increase with increasing crowbar insertion delay time. These errors were especially appreciable for three-phase short-circuits with crowbar insertion time delay higher than about 5 ms. With lower delays or during unsymmetrical faults, the crowbar insertion delay time had little significance on the fault current.

Figure 3.5   Simulated with instantaneous (red +), 2.5 ms delayed (green ◊), 5 ms delayed (blue □) crowbar insertion and calculated (black dotted) DFIG short-circuit current for a three-phase fault, with parameter $p=1$. The area encompassed in the rectangle in the first ms after the fault is magnified on the right part of the figure. Pre-fault voltage angle $\varphi=90^{\circ}$. Initial apparent power $S=0.8-j0.25$ pu, rotor speed $\omega_r=1.25$ pu.
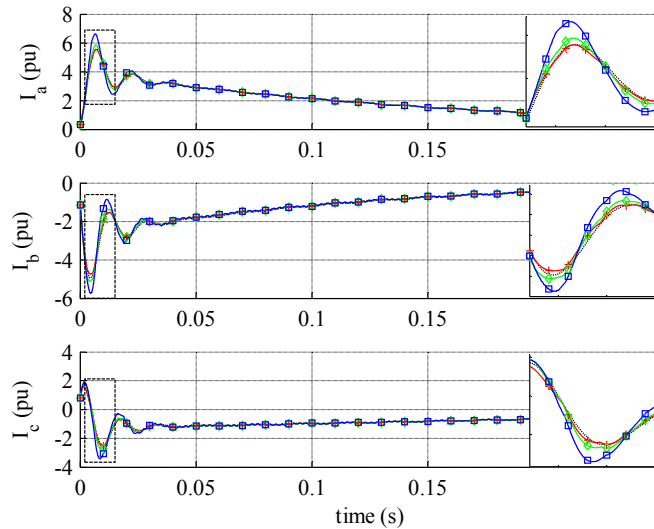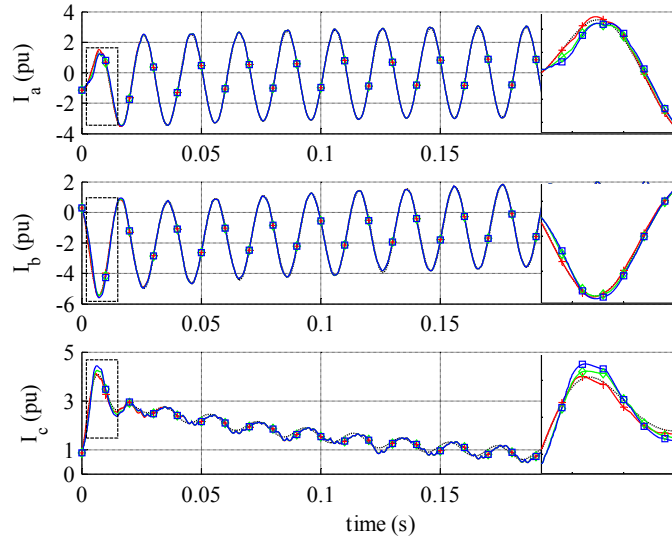
Figure 3.6   Simulated with instantaneous (red +), 2.5 ms delayed (green ◊), 5 ms delayed (blue □) crowbar insertion and calculated (black dotted) DFIG short-circuit current for a phase-phase (*b-c*) fault, with parameter *p=0.8*. Pre-fault voltage angle φ =0°. Initial apparent power *S=0.8-j0.25* pu, rotor speed ω_r=1.25 pu.

The non-linearity due to the connection of the crowbar resistance through a diode bridge are also noticeable in the simulation results especially in the case of the phase-phase fault, see Figure 3.6.

However, they do not cause significant deviations from the predictions obtained with Equation 3.43. Also, notice that the realistic value of the wind turbine inertia constant causes a change in rotor speed after the fault, leading to a small difference between the short-circuit currents simulated and calculated with 3.43, which assumes a fixed rotor speed. This difference is most visible in the simulated case of a phase-phase fault, Figure 3.6.

In Figure 3.7 it is reported a three-phase fault, same as in Figure 3.5, but with the DFIG operating at sub-synchronous speed, i.e. at lower initial loading. It is noted that the DFIG operating at sub-synchronous speed delivers less peak current.
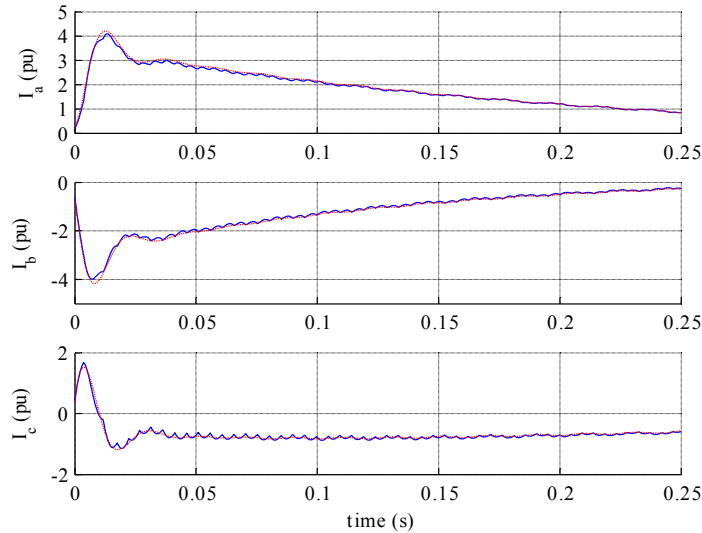
Figure 3.7   Simulated with instantaneous crowbar insertion (blue solid) and calculated (red dotted) DFIG short-circuit current for a three-phase fault, with parameter $p=1$. Pre-fault voltage angle $\varphi = 90°$. Initial apparent power $S=0.45-j0.18$ pu, rotor speed $\omega_r = 0.7$ pu.

Influence of MV line and step-up transformer

Equation 3.43 has been obtained under the assumption that the resistance of the generator stator windings is negligible. However, the resistance of the step-up transformer and MV line connecting the DFIG to the network may not be negligible. Their resistance and reactances should be added in series with the DFIG stator impedance when calculating the short-circuit current. To investigate how the resistive part of the transformer and MV line impedances influences the accuracy of Equation 3.43, simulations have been performed by adding a step-up transformer and a MV line to the network in Figure 3.2. A *Dyn* 33/0.575 kV step-up transformer, rated 1.25 times the DFIG rating, with $X=0.06$ pu and $R=0.01$ pu has been considered. The voltage angle shift due to the transformer *Dy* connection must be considered in the calculations. The line is a 50 mm^2 cable with $X=0.14$ Ω/km and $R=0.4$ *Ω/km.* Data for the transformer and the line parameters are from (Roeper 1985). Results for three-phase faults at the end of the line for two different line lengths, 10 and 45 km, are reported in Figure 3.8. The resistive part of the MV line appreciably decreases the accuracy of Equation 3.43 only when the line length becomes higher than 45 km, corresponding to a total

resistance equal to 10 times the DFIG stator resistance. Therefore, in most practical situations, the resistive part of the MV line should not decrease the accuracy of the method. The transformer resistance does not cause any appreciable loss of accuracy. The resistive character of the MV line impedance contributes to faster decay of the DC short-circuit current component.
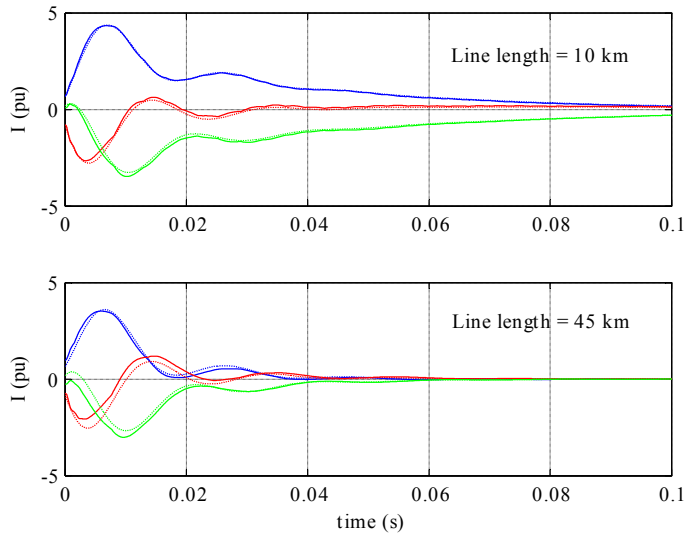
Figure 3.8   Simulated (solid) and calculated (dotted) DFIG phase currents at a three-phase short-circuit with parameter $p=1$ considering the step-up transformer and a MV line with two different length values. Pre-fault voltage angle $\varphi =90^o$. Initial apparent power $S=0.6-j0.18$ pu, rotor speed $\omega_r =1$ pu.

A case of an earth-fault at the end of the MV line is also reported in Figure 3.9, showing that Equation 3.43 provides accurate results also for unsymmetrical faults on the D-side of the transformer. It should be noted that the current shown in Figure 3.9 is the one at the DFIG terminals and not on the D-side of the transformer. To get the current on the D-side of the transformer, all the voltages in Equation 3.43 must be expressed on that side, taking into account the phase shift introduced by the Dy connection.

Figure 3.9 Simulated (solid blue) and calculated (dotted red) DFIG short-circuit current for a phase-ground (*a-g*) fault at the end of a 15 km MV line, with parameter *p=0.99*. Pre-fault voltage angle φ =90°. Initial apparent power *S=0.45-j0.18 pu*, rotor speed ω_r =0.7 pu.

Zero-sequence current

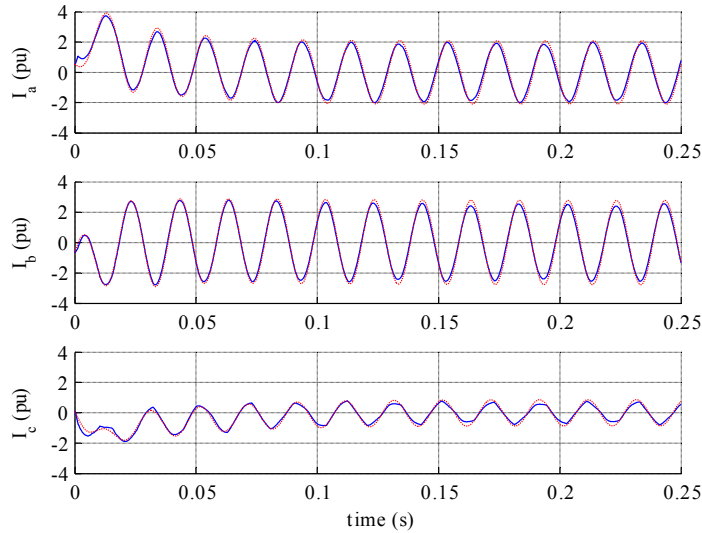In the case reported in Figure 3.9, the wind turbine does not deliver any zero-sequence current into the fault, because of the D connection of the step-up transformer. In the general case, the main transformer of a wind farm may be grounded on the high voltage side. This may for example be the case of a wind farm connected to the transmission system. In such a case, a zero-sequence current will flow into earth faults on the high voltage side. It is important to take into account this contribution when calculating the total wind farm current delivered into the earth fault. This can easily be achieved in two steps. Firstly, applying Equation 3.43, which is still valid apart the zero-sequence current contribution, and calculating the phase currents using Equation 3.4. Since the interest is now on the current on the high voltage side of the transformer, the voltages used in Equation 3.43 must be the ones on the high voltage side. Secondly, the zero sequence contribution must be added to the phase currents. If the total zero-sequence impedance to the fault is $Z_0=R_0+j\omega L_0$, for a phase-ground (*a-g*) fault the zero sequence contribution to be added to each phase current is:

$$i_{0f}(t) = \frac{V_0}{Z_0} e^{j\omega_s t}$$

$$i_0(t) = \text{Re}\left(i_{0f}(t) - i_{0f}(0)e^{-t/(L_0/R_0)} \right)$$

(3.44)

A phase-ground (*a-g*) fault with a direct grounding on the high voltage side created by a 500 kVA zig-zag transformer, is shown in Figure 3.10. The zero-sequence impedance of the zig-zag transformer is $Z_0=0.025+j0.06$ pu. The voltage on the high voltage side is considered to be 130 kV. The total fault current contribution from the wind farm into the fault in Figure 3.10 is calculated on the high voltage side and includes the DFIG contribution and the zero sequence current. Even in this case the calculated fault current accurately reproduces the simulated one.
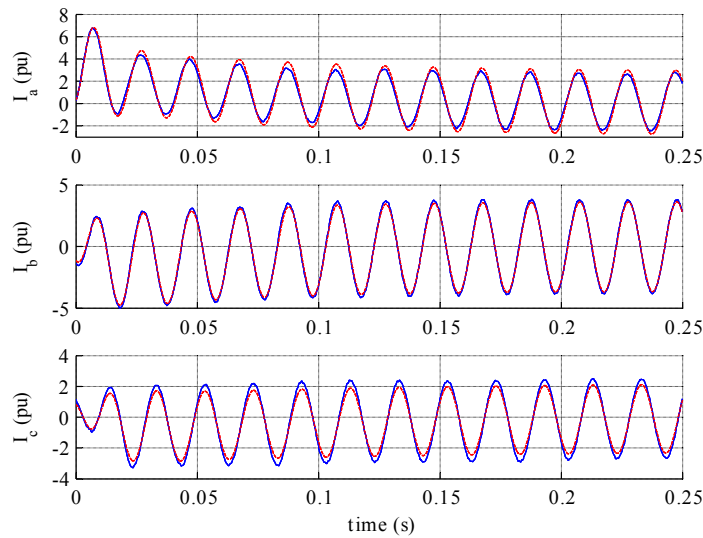
Figure 3.10 Simulated (solid blue) and calculated (dotted red) high voltage side short-circuit current for a phase-ground (*a-g*), with parameter *p=0.99*. Pre-fault voltage angle φ =90°. Initial apparent power *S=0.8-j0.25* pu, rotor speed ω_r=1.25 pu. The voltage on the high voltage side is 130 kV and a zig-zag transformer is used to create a direct grounding.

Influence of GSC and crowbar resistance

The total fault current delivered by a DFIG wind turbine is in reality the sum

of the DFIG fault current, which can be calculated according to Equation 3.43, and the GSC fault current. The GSC maximum current may be around one third of the DFIG rated current. Depending on how fast the GSC control is, it may take some cycles before it delivers maximum current. A three-phase fault is reported in Figure 3.11 including also the contribution of the GSC. As seen, the GSC contributes to a steady-state current component, but does not affect much the DFIG current delivered under the first cycles after the short-circuit.

Finally, the impact of the crowbar resistance value is here investigated by changing its value from 20, as in all previous cases, to 5 times the DFIG rotor resistance. A three-phase fault as in Figure 3.5 has been considered and the calculated and simulated results are shown in Figure 3.12. When comparing with Figure 3.5, one can see that a decreased crowbar resistance results in a higher peak current and a longer rotor transient time constant, which implies a slower decay of the AC stator current component. This is in agreement with what has been shown in (Pannell 2010).
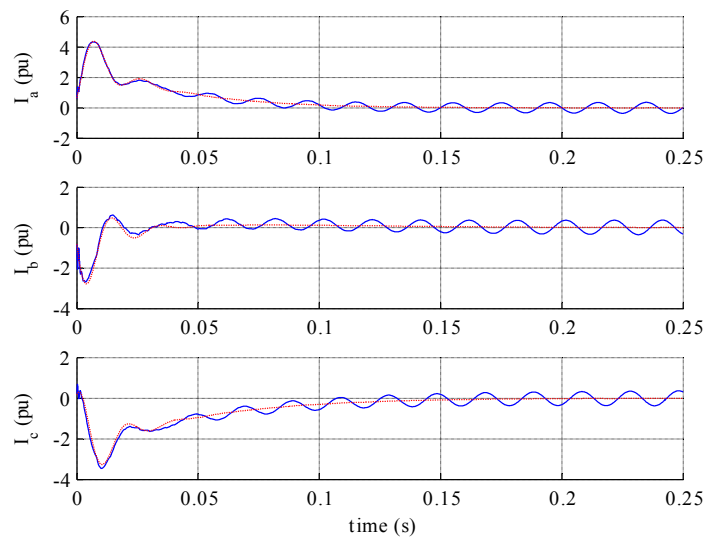

Figure 3.11 Simulated DFIG and GSC (solid blue) and calculated DFIG (dotted red) phase currents at a three-phase short-circuit with parameter $p=1$ considering the step-up transformer and a MV line of 10 km. Pre-fault voltage angle $\varphi = 90^o$. Initial apparent power $S=0.6-j0.18$ pu, rotor speed $\omega_r = 1$ pu.

Also, in the same reference it has been found that the stator natural flux decays at "near-dc", meaning that it is actually slowly rotating while decaying. In (Pannell 2010) the "near-dc" frequency of a 7.5 kW DFIG was found to be 0.46 Hz without crowbar resistance and 1.76 Hz when a crowbar resistance is connected. Here, the angular rotation of the stator natural flux is given by the imaginary part of $1/T_{s,DFIG}$. For the considered machine, with a crowbar resistance of 20 times the DFIG rotor resistance, the stator natural flux rotates with 0.3 Hz. This frequency drops to 0.1 Hz with a crowbar resistance of 5 times the DFIG rotor resistance. The difference in "near-dc" frequencies found here and in (Pannell 2010) is due to different machine parameters. If the method proposed in this chapter is applied to the machine considered in (Pannell 2010) without crowbar resistance, a frequency of 0.46 Hz is found. Choosing a crowbar resistance that results in the same rotor transient time constant as in (Pannell 2010), results in a frequency of 1.67 Hz. These results match very well with what has been found in the mentioned reference.
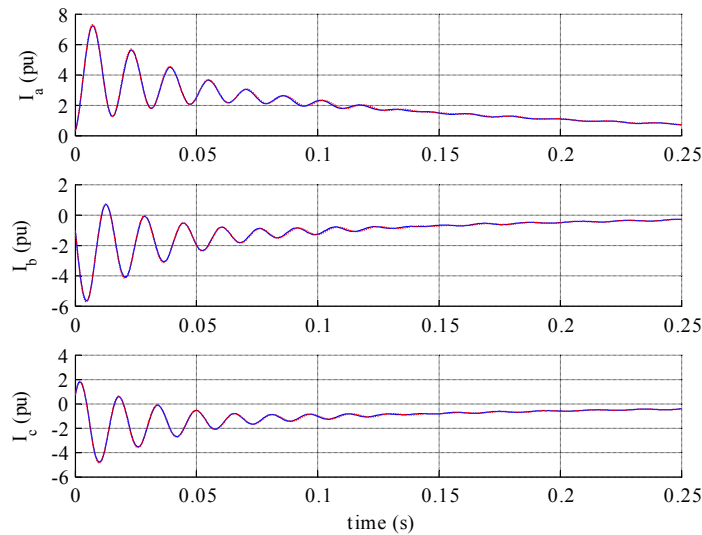

Figure 3.12 Simulated (solid blue) and calculated DFIG (dotted red) phase currents at a three-phase short-circuit with parameter $p=1$. Pre-fault voltage angle $\varphi =90°$. Initial apparent power $S=0.8\text{-}j0.25$ pu, rotor speed $\omega_r =1.25$ pu. The crowbar resistance is chosen to be equal to 5 times the DFIG rotor resistance.

3.7   Summary

An approximate method for predicting the symmetrical and unsymmetrical short-circuit current of a SCIG and a DFIG has been proposed. The proposed method gives a good prediction of the short-circuit behavior of a wind farm using a DFIG with crowbar protection, both for symmetrical and unsymmetrical faults in the network. A linear model of the induction machine has been considered and saturation has been neglected.

The accuracy of the results obtained with the proposed method may be sufficient to replace the use of simulations in many contexts, e.g. calculation of maximum current, calculation of its DC and AC components and short-circuit calculations for protection relays settings. The impedances of step-up transformer and MV line should be added in series with the DFIG stator impedance. Even though these impedances may have a non-negligible resistive part, it has been found that in practical situations this fact does not affect the accuracy of the method. Moreover, the method is capable of accurately reproducing the DFIG fault current even for unsymmetrical faults on the MV side of the step-up transformer.

A factor that may limit the accuracy of the proposed method is the delay with which the crowbar resistance is inserted relative to the fault inception instant. Delays below 5 ms result in almost no loss of accuracy.

Chapter 4

Fault Currents of DFIG Wind Turbines with Chopper

Some of the commercial DFIG wind turbines installed nowadays are protected by blocking the RSC and using a chopper resistance on the DC-link without inserting a crowbar resistance. The chopper resistance is switched to keep the DC-link capacitor voltage within an acceptable range. The analysis of the fault current contribution of this type of DFIG wind turbines is rare and represents a new issue in the literature. This chapter presents a method to model the DC link with the chopper as an equivalent resistance directly connected to the rotor during symmetrical faults. This allows calculating the three-phase short-circuit current of these wind turbines as that of a wind turbine with an equivalent crowbar resistance. The method is especially useful considering that accurate models of DFIG wind turbines with chopper protection are not commonly included in power system simulators. The material presented in this chapter is based on Publication [3].

4.1   Introduction

The fault current delivered by a DFIG wind turbine with DC chopper protection is seldom analyzed in the literature. In (Martinez 2011(a)) it is proposed to model the DC-link capacitor and chopper simply as a resistance, with the same value as the chopper resistance. This assumption means that the whole rotor current rectified by the diode bridge of the RSC goes into the DC-chopper resistance, i.e. no current goes into the DC-link capacitor. This may be correct just after a solid three-phase fault close to the DFIG terminals when the DFIG is at full power, depending on the chopper resistance value. But some time after the fault, for less severe faults or if the DFIG is not at full power, the DC chopper will however not be continuously switched on after

the fault, but it will be switched according to a modulation index chosen to control the DC-link voltage within a tolerance band. Under these conditions, just using the DC chopper nominal resistance value is not accurate.

A closer analysis of the system made up of the rotor circuit, the diode bridge of the RSC, the DC-link capacitor and the chopper is performed in this chapter. The basic idea behind the analysis is the same as in reference (Martinez 2011(a)), i.e. to model the DC-link capacitor and chopper as an equivalent resistance seen from the DFIG rotor circuit. However, it is shown that accurate modelling requires a different value of the equivalent resistance for each different symmetrical fault and initial loading of the DFIG.

The analysis proposed here is valid under the period the RSC is blocked. This is also the period when the highest fault currents occur. Moreover, the fault current is related only to the physical system composed by the induction generator with its rotor circuit connected to the DC-link capacitor and DC chopper resistance through a diode bridge rectifier.

Detailed models of a DFIG with chopper protection are not commonly available in power system simulation tools. Before simulating, modelling of the DFIG with chopper protection should be performed, with explicit detailed representation of the switched chopper resistance with its control logic and of the free-wheeling diodes of the RSC. This would also result in increased simulation time. The approach proposed here allows disregarding all these issues and allows using the standard model of a DFIG with crowbar protection also to represent a DFIG with chopper protection during short-circuits.

The proposed equivalence between DFIG with chopper and crowbar protection also allows to use short-circuit calculation methods developed for a DFIG with crowbar protection, as for example the methods exposed in (Morren 2007) and in Chapter 3. In particular the maximum short-circuit current delivered to the grid can be calculated.

The proposed theoretical analysis has been validated through simulations. The results for the short-circuit current obtained through the proposed method are compared with simulations of a detailed model of a DFIG with chopper protection under different conditions, showing good agreement. The DFIG model includes a detailed representation of the RSC and GSC switching. It is also shown that the DFIG with chopper protection delivers lower short-circuit current than a DFIG with standard crowbar protection, especially for low initial loading.

4.2   DFIG with DC Chopper Protection

After the short-circuit occurrence, the RSC is blocked and the rotor current flows into the DC-link. Under this period, the rotor circuit of the DFIG is thus connected to the DC-link capacitor through the diode bridge made up by the anti-parallel diodes of the RSC, see Figure 4.1.
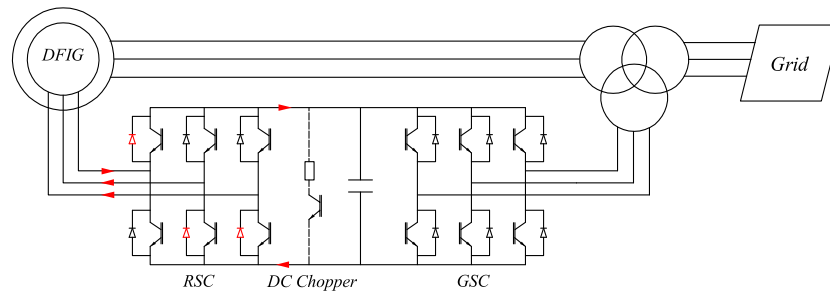

Figure 4.1 DFIG with DC chopper protection. Rotor current flow through the anti-parallel diodes of the RSC during a fault with the RSC blocked.

The chopper resistance will be switched to keep the DC capacitor voltage within acceptable values. The GSC will also strive to control the DC-link capacitor voltage, but under serious faults its capability for DC-link voltage control is highly reduced. The rotor circuit demagnetizes feeding current into the DC-link capacitor, whose voltage is controlled through the chopper. As explained in (Lopez 2007), it is mainly the voltage caused in the rotor circuit by the natural stator flux that causes high rotor currents. As already mentioned in Chapter 3, the natural stator flux arises to assure the continuity of the stator flux before and after the fault, according to the flux linkage theorem (Kimbark 1968). This voltage decays with the stator transient time constant and has a frequency equal to *1-slip* times the network frequency. During this period the rotor circuit of the DFIG can be considered as a three-phase decaying voltage source, induced in the rotor by the stator natural flux, connected through a diode bridge rectifier, the anti-parallel diodes of the blocked RSC, to a constant DC voltage source, see Figure 4.2.

When the rotor current has decayed sufficiently, the RSC may be restarted while the fault is still present. During this stage the RSC is able to control the rotor current and hence the stator current. The problem addressed here is to estimate the fault current delivered during the period the RSC is blocked.

The described system is highly non-linear due to the presence of the diode

bridge and due to the action of the chopper. Some simplifications must be done to allow for an analytical study to be carried out.
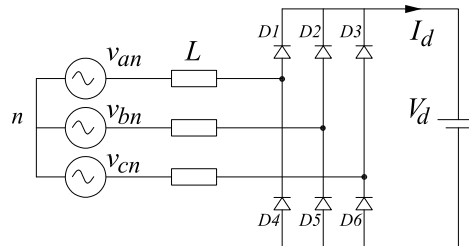

Figure 4.2 Equivalent circuit of a DFIG rotor circuit connected to the DC-link through the anti-parallel diodes of the RSC during a three-phase short-circuit. The AC voltage is induced by the natural stator flux. L is the per-phase inductance on the AC side. The resistance on the AC side is neglected.

In this chapter, the main idea is to look upon the DC-link system composed of the DC-link capacitor and the chopper as if it were a fixed DC voltage source. This is of course an approximation since the DC-link voltage will actually vary during the transient but if the chopper is properly sized and controlled the DC-link voltage variation will not exceed a predefined value, e.g. ±10 % of its nominal value. In turn, the DC-link voltage source is seen from the rotor circuit side of the diode bridge rectifier as a variable resistance, whose value is equal to the ratio between the DC-link voltage and the rectified rotor current. The value of this resistance will change with time, because of the decaying transient rotor current. The equivalent resistance seen from the rotor circuit is much higher than the rotor winding resistance and it increases with time, since the rotor current decreases with time. In effect, it is therefore possible to look at this configuration of the DFIG as a short-circuited induction generator with an equivalent high rotor resistance, with the only difference being that the equivalent rotor resistance is now changing with time. However, to simplify the analysis the value of the equivalent resistance seen from the rotor circuit is assumed to be constant and equal to the ratio between the nominal DC-link voltage and the rectified rotor current at the instant of the short-circuit.

The equivalent resistance will act as a crowbar resistance implying a very fast demagnetization of the rotor natural flux, i.e. a fast decay of the AC stator current component induced by the rotor natural flux. Once the value of the equivalent resistance seen by the rotor circuit is known, it can be used to

calculate the maximum short-circuit current of the DFIG as if this had a crowbar protection. The key issue is therefore to estimate the equivalent resistance seen by the rotor circuit during the period the RSC is blocked. To do this the circuit shown in Figure 4.2 is first analyzed.

4.3   Diode Bridge Rectifier with DC Voltage Source

When a three-phase fixed magnitude voltage source with a series AC inductance is connected to a DC voltage source through a diode bridge rectifier, as in Figure 4.2, it will supply a current whose magnitude decreases with increasing DC voltage. If the ratio between the peak AC and DC voltages is sufficiently high, the AC side current is close to a sinusoidal curve and it flows continuously. In the following it is assumed that this condition holds, when not otherwise stated. Simulated voltages and currents for such a system are shown in Figure 4.3.
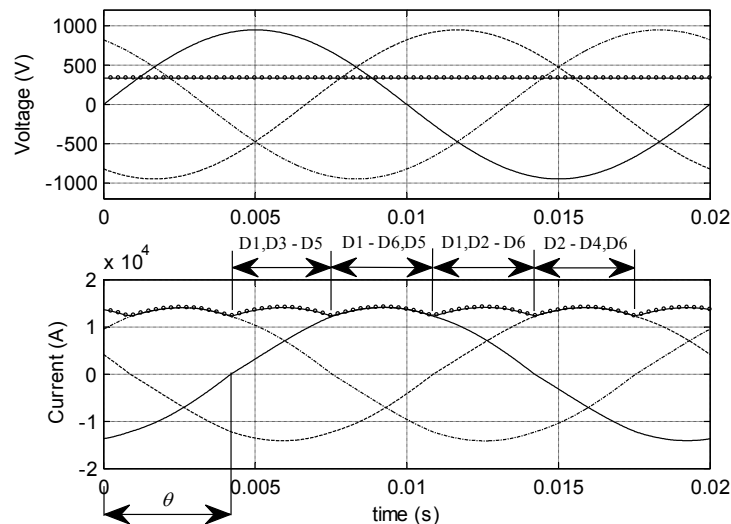
Figure 4.3 Simulated phase *a* (solid), phase *b* (dashed) phase *c* (dashed-dotted) and DC (o) voltages (above) and currents (below) for the system shown in Figure 4.2. The peak AC voltage is higher than the DC voltage.

The DC current will consist of six pulses during one period. To calculate the AC current as a function of the AC and DC voltages, it can be noticed that the diode D1 in Figure 4.2 must start conducting when the current in phase *a* becomes positive, i.e. at $\omega t=\theta$, see Figure 4.3. Meanwhile diode D3 will still

conduct until the current in phase *c* becomes negative. Therefore under this period the DC rectified current is the sum of the currents in phase *a* and phase *c*. Diode D5 is also conducting during this period. After the current in phase *c* has become negative, diode D3 will cease to conduct and diode D6 takes over the current in phase *c*. At this stage the rectified current is equal to phase *a* current, flowing through diode D1.

The AC voltages and currents can be expressed as:

$$v_{an} = V \sin(\omega t)$$
$$v_{bn} = V \sin\left(\omega t - \frac{2}{3}\pi\right) \tag{4.1}$$
$$v_{cn} = V \sin\left(\omega t - \frac{4}{3}\pi\right)$$

$$i_a = I \sin(\omega t - \theta)$$
$$i_b = I \sin\left(\omega t - \theta - \frac{2}{3}\pi\right) \tag{4.2}$$
$$i_c = I \sin\left(\omega t - \theta - \frac{4}{3}\pi\right)$$

In the period in which diodes D1, D5 and D6 are conducting the circuit shown in Figure 4.2 is equivalent to the one shown in Figure 4.4.
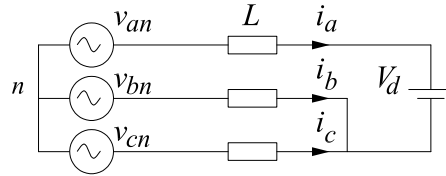
Figure 4.4 Equivalent circuit for the system shown in Figure 4.2, when diodes D1, D5 and D6 are conducting.

During this period one can write, with reference to Figure 4.4:

$$v_{bn} - L\frac{di_b}{dt} + L\frac{di_c}{dt} - v_{cn} = 0$$
$$v_{an} - v_{bn} - L\frac{di_a}{dt} + L\frac{di_b}{dt} = V_d \tag{4.3}$$

The above equations are valid in particular for $\omega t = \theta + \pi/2$, i.e. when phase *a* current is at its maximum. By solving the above equations at $\omega t = \theta + \pi/2$ for θ

and I using the definition of voltages and currents given in Equations 4.1 and 4.2, after some manipulations one gets:

$$\theta = \cos^{-1}\left(\frac{2V_d}{3V}\right)$$
$$I = \frac{V\sin(\theta)}{\omega L}$$

(4.4)

The above expressions are valid under the assumption that the AC current is sinusoidal. Simulations of the system shown in Figure 4.2 show that this is a good approximation when the ratio between V and V_d is greater than 1.

Seen from the AC side, the DC voltage source is equivalent in steady-state to a resistance whose value is the ratio between the DC voltage and the average rectified current. The term $3/\pi$ is used to get the average value of the rectified current, made up of six pulses, given the peak value of the AC current. The value of the equivalent resistance on the DC side is reported in Equation 4.5.

$$R_d = \frac{V_d}{I_d} = \frac{V_d}{\frac{3}{\pi}I}$$

(4.5)

The equivalent DC resistance R_d has to be connected on the DC side of a diode bridge rectifier.

If instead it is desired to get directly an equivalent resistance as seen from the AC side and to skip the diode bridge, some further considerations are necessary. For a DFIG, a realistic range for the product ωL is between 0.02 and 0.07 Ω, assuming the sum of the stator and rotor leakage reactances to vary between 0.15 pu (Anderson 1995) and 0.34 pu (as the considered DFIG, whose parameters are reported in Table 3.1), a stator voltage of 575 or 690 V and a generator rated power between 1.5 and 2 MVA. Realistic values of the ratio V/V_d are between 1 and 2, see Equation 4.13. Given these assumptions the ratio between the equivalent DC resistance R_d and the value of ωL is in the range between 0.5 and 1.5.

The issue consists now in replacing the diode bridge and the resistance R_d with an equivalent resistance R_{eq}, directly connected on the AC side. The value of R_{eq} must be chosen so that the same peak current I on the AC side is obtained as with the diode bridge and R_d. It turns out that, under the made assumptions for the values of the different parameters involved, the same peak

current I is obtained when the power P_{AC} delivered to R_{eq} is equal to the peak power delivered to R_d, $P_{DC,max}$. Note that the power delivered to R_{eq} is constant, being the considered AC circuit a three-phase and balanced one. This fact can be observed in Figure 4.5 where two different cases are reported.
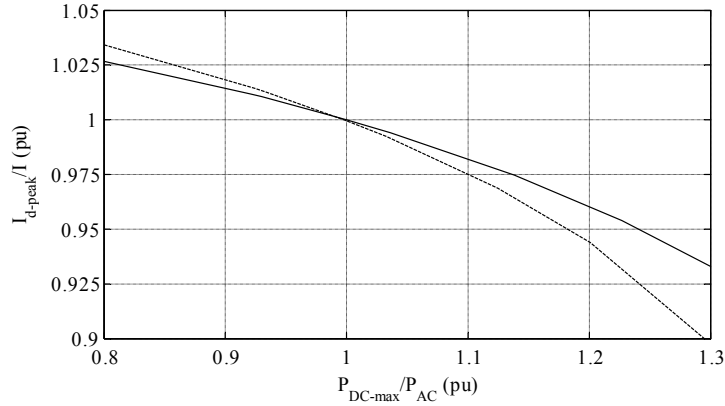
Figure 4.5 Ratio between peak current with diode bridge and R_d and peak current with R_{eq} versus ratio between peak power with diode bridge and R_d and power delivered to R_{eq}. V/V_d =2 and ωL=0.02 Ω (solid), V/V_d=1.8 and ωL =0.07 Ω (dashed).

Therefore, the condition to be used to find R_{eq} is that the maximum instantaneous power on the DC side should be equal to the power delivered to the equivalent AC resistance R_{eq} along with the condition of same peak current in both cases, i.e. $I_{d\text{-}peak}=I$. This leads to:

$$P_{DC,\max} = R_d I^2 = P_{AC} = 3R_{eq}\left(I / \sqrt{2}\right)^2 \tag{4.6}$$

By solving Equation 4.6, one finds that the equivalent resistance seen from the AC side is

$$R_{eq} = \frac{2}{3} R_d \tag{4.7}$$

Applying this relation results in the same peak current in both cases. The results in Equations 4.5 and 4.7 have been verified by comparing simulations of the system in Figure 4.2 with the same system but with the diode bridge

and V_d replaced by a resistance, whose value is given by Equation 4.7. The above analysis is valid under the assumption that the peak AC voltage is higher than the DC voltage.

The currents in a case when the peak AC voltage is almost equal to the DC voltage are shown in Figure 4.6.
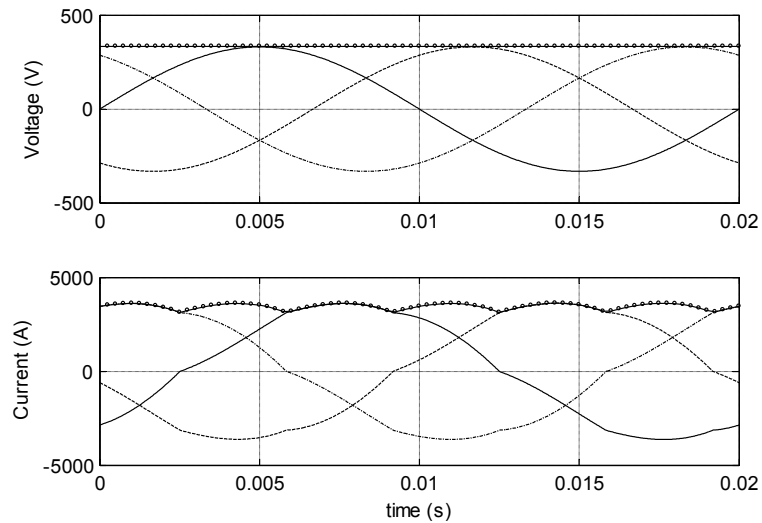
Figure 4.6 Simulated phase *a* (solid), phase *b* (dashed) phase *c* (dashed- dotted) and DC (o) voltages (above) and currents (below) for the system shown in Figure 4.2. The peak AC voltage is almost equal to the DC voltage.

It is observed that they are no longer pure sinusoids. Even in these cases it is possible to replace the DC voltage with a resistance R_d behind the diode bridge. However, the resistance R_d increases as compared to the one calculated in Equation 4.5. The increase is non-linear and depends on the ratio between the AC RMS voltage and the DC voltage according to Figure 4.7, which has been obtained by simulations.

Simulations also show that these results are independent of the value of the inductance on the AC side, at least for a wide range of inductance values. Even in this case, the equivalence between the system in Figure 4.2 and the same system in which V_d is replaced by a properly chosen resistance has been checked through simulations. When the currents are no longer sinusoidal, Equation 4.7 is no longer exact, since replacing the diode rectifier and the

DC voltage source with an equivalent resistance on the AC side, obviously, cannot reproduce the non-sinusoidal AC currents. However, choosing R_{eq} as in Equation 4.7 and according to Figure 4.7, still gives a reasonable approximation of the AC current for the system shown in Figure 4.2. A case is reported in Figure 4.8, where the non-sinusoidal current of the system with DC voltage source and diode rectifier is shown along with the current in the same system, but with an equivalent resistance on the AC side.
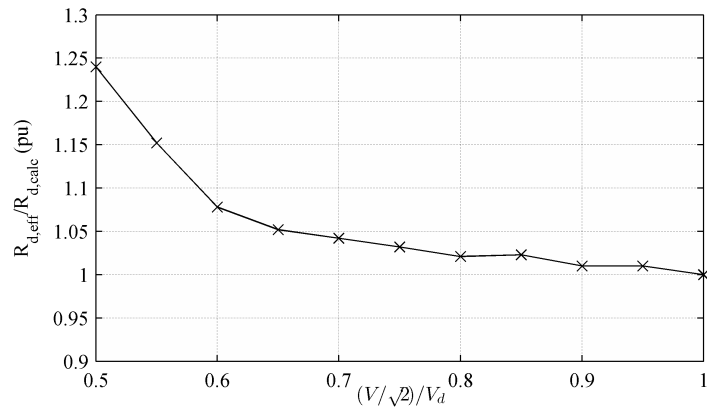

Figure 4.7 Ratio between the effective resistance $R_{d,eff}$ on the DC side (found by simulations) and the resistance $R_{d,calc}$ calculated with Equation 4.5 as a function of the ratio between the RMS AC voltage $V/\sqrt{2}$ and the DC voltage V_d.
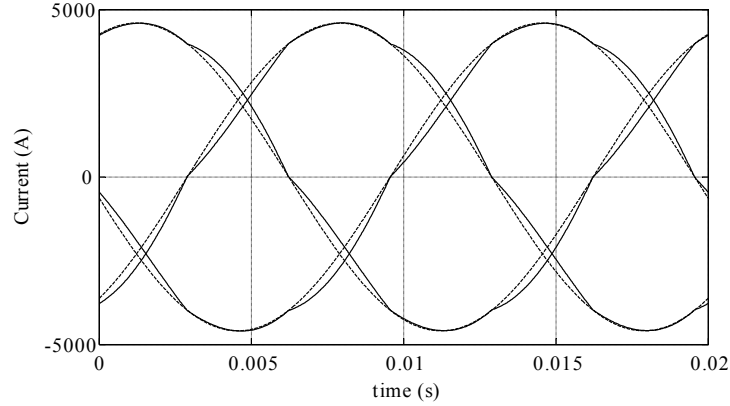
Figure 4.8 Simulated AC phase currents for the system shown in Figure 4.2 (solid) and for the same system but with the DC voltage source and diode rectifier replaced by an equivalent resistance on the AC side (dashed). The ratio between the RMS AC voltage $V/\sqrt{2}$ and the DC voltage V_d is chosen equal to 0.8.

4.4 DFIG with DC chopper protection

The results obtained above for a diode bridge rectifier and a DC voltage source can be directly translated to the rotor circuit of a DFIG with chopper protection during a three-phase fault when the RSC is blocked. All DFIG AC voltages and currents in this section are expressed in a stator reference frame and are observed from the stator. The DC-link voltage seen from the stator is

$$V_d^{'} = V_{d,nom} \frac{N_{stat}}{N_{rot}} \tag{4.8}$$

where N_{stat} and N_{rot} indicate the number of turns of stator and rotor windings. The apex is used in Equation 4.8 to indicate that the DC quantity is referred to the stator side. A typical value of the rotor to stator winding turns ratio N_{rot}/N_{stat} for a DFIG in wind power application may be around 3 (Petersson 2005). This is to get low currents in the rotor circuit during normal operation thus reducing the current rating for the RSC.

As explained in (Lopez 2007) it is the voltage caused in the rotor by the stator natural flux that is the highest component in the transient rotor voltage during symmetrical faults. Its frequency is equal to the electrical rotor speed and its peak value seen from the stator at the moment of fault occurrence is

given as:

$$V_{r,nat} = (1-s)\sqrt{2}\,\frac{L_m}{L_s}\left(\frac{V^{RMS}_{pre,LL}}{\sqrt{3}} - \frac{V^{RMS}_{post,LL}}{\sqrt{3}}\right) \tag{4.9}$$

$V_{r,nat}$ is the peak value of the AC voltage in the rotor circuit, i.e. it must substitute V in Equation 4.4. $V^{RMS}_{pre,LL}$ and $V^{RMS}_{post,LL}$ are the line-line steady-state voltages before and after the fault.

To find the peak value of the rotor current after fault occurrence, one must take into account that the angular frequency of the induced AC rotor voltage is equal to the rotor angular speed ω_r. The equivalent inductance on the AC side of the rectifier, i.e. the rotor circuit, is equal to the series connection of the rotor leakage inductance and the parallel between the magnetizing and the stator leakage inductance, see Figure 3.1. This is the transient rotor inductance L_r', defined, for example, in (Morren 2007). The resulting equations for a DFIG, corresponding to Equations 4.4, 4.5 and 4.7, are thus:

$$\theta = \cos^{-1}\left(\frac{2V_d'}{3V_{r,nat}}\right)$$
$$I_r = \frac{V_{r,nat}\sin(\theta)}{\omega_r L_r'} \tag{4.10}$$

$$R_{eq} = \frac{2}{3}\frac{V_d'}{I_d'} = \frac{2}{3}\frac{V_d'}{3/\pi\,I_r} \tag{4.11}$$

For the DFIG model considered in the simulations, the following values apply:

$$\sqrt{2}\,\frac{V^{RMS}_{pre,LL}}{\sqrt{3}} = 469V$$
$$V_d' = 335V \tag{4.12}$$
$$\frac{N_{rot}}{N_{stat}} = 3.43$$

The ratio between the induced peak AC rotor voltage and the DC-link voltage, both referred to the stator side, depends on the initial slip and on the magnitude of the voltage dip during the fault.

The following values are obtained in case of a solid short-circuit for three different slips:

$$\frac{V_{r,nat}}{V_d^{'}} \approx 1.8 \text{ , for } s = -0.3$$

$$\frac{V_{r,nat}}{V_d^{'}} \approx 1.4 \text{ , for } s = 0 \qquad\qquad\qquad (4.13)$$

$$\frac{V_{r,nat}}{V_d^{'}} \approx 1 \text{ , for } s = +0.3$$

As it can be seen, for high positive slip values the ratio between the induced rotor voltage and the DC-link voltage approaches 1. This means that the equivalent resistance calculated in Equation 4.5 must be increased as shown in Figure 4.7. For negative slip values, the analysis resulting in Equation 4.5 should give acceptable results. Negative slip values are also those resulting in higher short-circuit currents.

The ratios in Equation 4.13 are actually valid only at the moment of fault occurrence. They decrease with time as the induced rotor voltage decreases. As a consequence, a variable equivalent resistance should be considered, and it would increase with time. However, this is not practical for use in a simulation tool and the use of a fixed resistance is proposed here instead, whose value is obtained just after fault occurrence as in Equation 4.11.

4.5   Simulations

The aim of this section is to check how accurately the DC-link system of a DC chopper protected DFIG can be represented as an equivalent resistance, according to the theoretical analysis performed above. The short-circuit current delivered by a DFIG wind turbine with chopper protection has been therefore compared to the one delivered by the same DFIG wind turbine but equipped with a crowbar protection, whose resistance has been appropriately chosen. Simulations have been performed in MATLAB SimPowerSystems (MATLAB R2009b) and a DFIG model available in the standard library has been used. Detailed representation of RSC and GSC switching is included in the model. The DFIG wind turbine is connected to an external power system as shown in Figure 4.9, without a step-up transformer. The voltage dip

during the fault can be varied by changing the value of the parameter p, with $p=1$ corresponding to a solid short-circuit at the DFIG terminals.
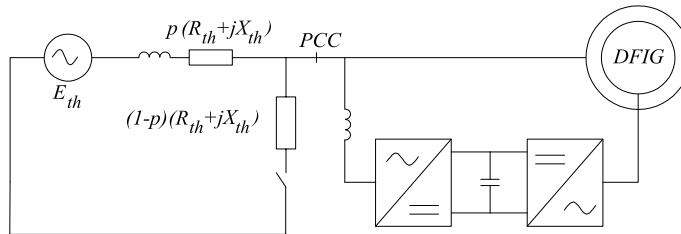

Figure 4.9 Single-line diagram of the power system used in the simulations. To simulate a strong network, the parameter X_{th} has been fixed to one hundredth of the generator base impedance. $X_{th}/R_{th}=10$.

The DFIG considered in these simulations is the same as described in Chapter 3 and its parameters can be found in Table 3.1. The model has been modified to represent a DFIG with crowbar protection or with chopper protection. The crowbar is inserted at the moment of fault occurrence. The chopper is connected through a controllable switch when the DC-link capacitor voltage exceeds a predefined value and disconnected when it reaches a second lower value. The RSC is kept blocked in both cases for 100 ms, i.e. for the total duration of the fault. Only one model at a time is connected.

The crowbar resistance for the model with crowbar protection is chosen according to Equation 4.11 and when necessary modified according to the results in Figure 4.7. The value of the crowbar resistance depends therefore on the voltage dip during the fault and on the initial slip of the DFIG. Therefore, for each different simulation, the value of the crowbar resistance has been adjusted.

In commercial wind turbines, the RSC is restarted when the rotor current decreases below a threshold value and therefore the time the RSC is blocked will depend upon the type of fault, voltage dip magnitude and the DFIG pre-fault slip. However, not knowing in detail how the conditions to restart the RSC are implemented in a commercial wind turbine, it is here assumed that the RSC remains blocked for 100 ms. Only the DFIG fault currents during the time the RSC is blocked are reported here. This implies that the short-circuit current shown in the next figures must be interpreted as the one the DFIG would deliver if the RSC is not restarted.

The current contribution of the GSC is not included either. In the worst case, the GSC current may be up to about 30 % of the rated wind turbine power, depending on the GSC rating, and can be considered to be known. This current contribution could be accounted for if needed, by adding it to the fault current delivered by the DFIG. A study on the influence of the GSC current contribution on the total wind turbine fault current has also been performed in Chapter 3.

Different cases have been considered with different initial loading for the DFIG and/or different voltage dip magnitude during the short-circuit. In each case, two simulations have been performed, one with the DFIG with crowbar and one with the DFIG with chopper protection. The two DFIGs are at the same operating point before the short-circuit occurrence. The time step used in all the simulations is 10 μs.

Simulation results

Three different initial loadings for the DFIG have been considered. For each of these cases, three-phase short-circuits resulting in a voltage dip of 100 % and 80 % at the generator terminals have been simulated. The initial DFIG slip, the active and reactive power corresponding to these initial conditions and the equivalent resistance used in the simulations are summarized in the text of Figure 4.10 to Figure 4.15, where the instantaneous phase currents for the chopper and crowbar protected DFIG are reported.

It is seen how the proposed method gives good results for all the considered initial loading and fault cases. The accuracy of the results would decrease for sub-synchronous operation and for faults causing low voltage dips if the correction reported in Figure 4.7 would not be applied to the equivalent crowbar resistance calculated with Equation 4.11.

Figure 4.10 Three-phase currents of DFIG with DC chopper (solid) and equivalent crowbar (dotted) protection during a three-phase fault with parameter *p=1*. Crowbar equivalent resistance is *0.0345 Ω*. Initial apparent power *S=0.85+j0 pu, ω$_r$=1.22 pu*.

Figure 4.11 Three-phase currents of DFIG with DC chopper (solid) and equivalent crowbar (dotted) protection during a three-phase fault with parameter *p=0.8*. Crowbar equivalent resistance is 0.0455 *Ω*. Initial apparent power *S=0.85+j0 pu, ω$_r$=1.22 pu*.

Figure 4.12 Three-phase currents of DFIG with DC chopper (solid) and equivalent crowbar (dotted) protection during a three-phase fault with parameter *p=1*. Crowbar equivalent resistance is 0.0368 *Ω*. Initial apparent power *S=0.39+j0 pu*, *ωr=0.99 pu*.

Figure 4.13 Three-phase currents of DFIG with DC chopper (solid) and equivalent crowbar (dotted) protection during a three-phase fault with parameter *p=0.8*. Crowbar equivalent resistance is *0.0509 Ω*. Initial apparent power *S=0.39+j0 pu*, *ωr=0.99 pu*.

Figure 4.14 Three-phase currents of DFIG with DC chopper (solid) and equivalent
crowbar (dotted) protection during a three-phase fault with parameter
p=1. Crowbar equivalent resistance is *0.0423 Ω*. Initial apparent power
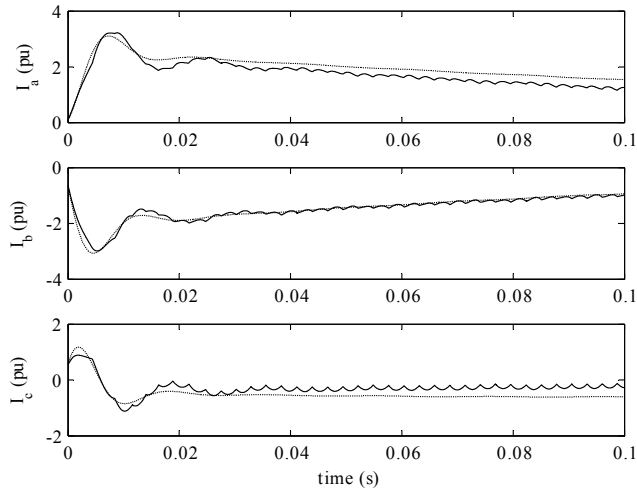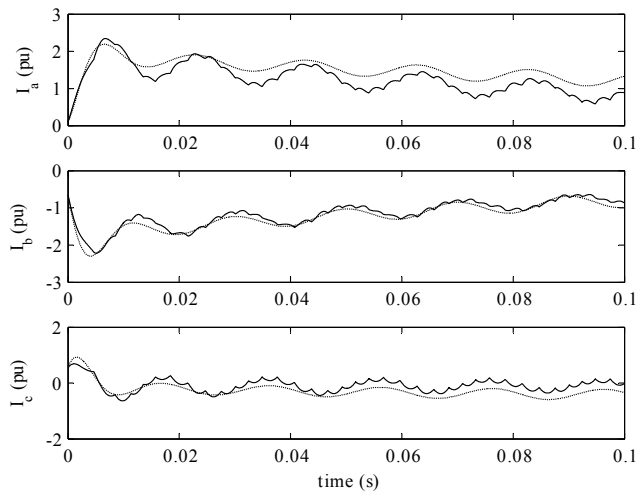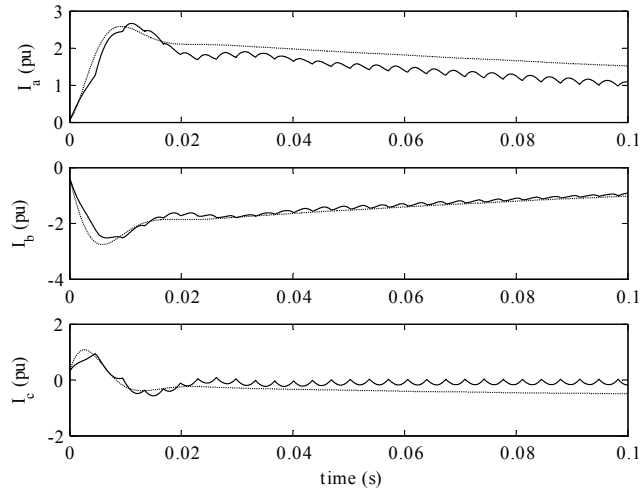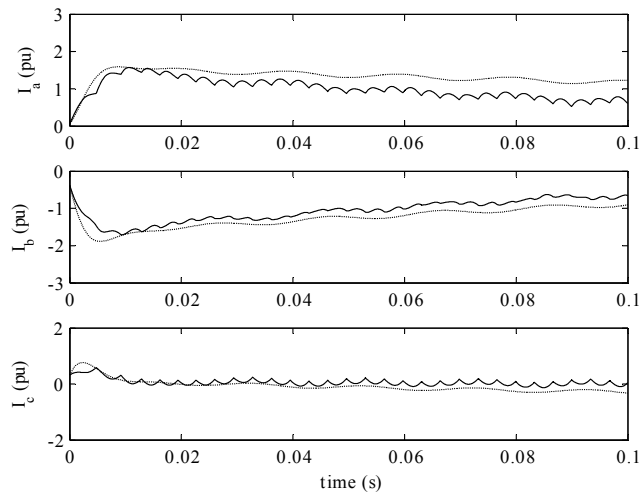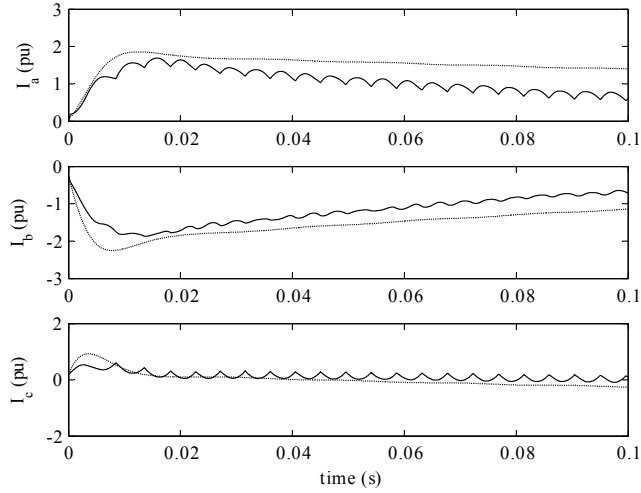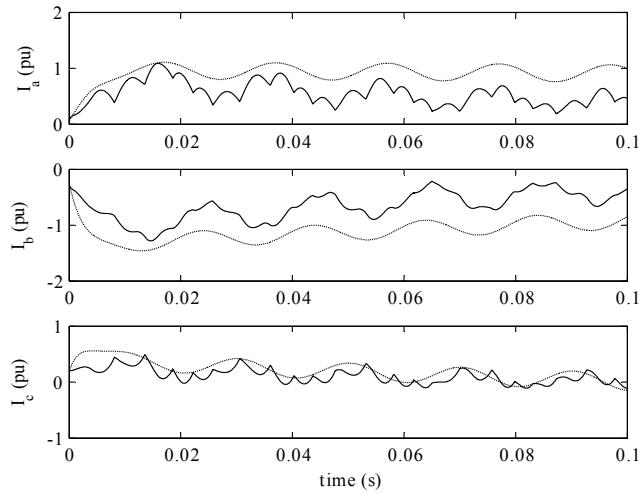*S=0.19+j0 pu, ω_r=0.76 pu*.

Figure 4.15 Three-phase currents of DFIG with DC chopper (solid) and equivalent
crowbar (dotted) protection during a three-phase fault with parameter
p=0.8. Crowbar equivalent resistance is *0.0679 Ω*. Initial apparent power
S=0.19+j0 pu, ω_r=0.76 pu.

In all cases the accuracy of the results obtained with the equivalent crowbar resistance decreases with time. This is however expected, since the actual equivalent resistance increases with time while a fixed resistance has been used in the simulations. The time divergence between the results from the two models seems however not critical and the use of a fixed equivalent resistance is therefore justified, especially in the first cycles after the fault when the RSC is blocked.

The effects of the diode bridge rectifier are visible in the pulse shaped phase currents for the DFIG with chopper protection. These pulses are not present in the DFIG with crowbar protection case since the crowbar resistance has been directly connected to the rotor.

It is interesting to note how the short-circuit current magnitude of the DFIG with chopper protection decreases not only with decreasing voltage dip magnitude caused by the fault but also with decreasing initial loading of the DFIG. In the cases with maximum positive slip, corresponding to a low initial loading, the DFIG with chopper protection delivers a current below 2 pu even in the case of a solid short-circuit at its terminals, see Figure 4.14. With this initial loading, the delivered short-circuit current is below 1 pu if the three-phase short-circuit causes a voltage dip of 80 % at the DFIG terminals, see Figure 4.15. This means that in these cases, it is possible that the RSC would block for a time shorter than 100 ms or not block at all. Therefore when the short-circuit currents obtained with the proposed method are low, as for example in Figure 4.13, Figure 4.14 and Figure 4.15, they are to be interpreted as the currents that would be delivered by the DFIG if the RSC would be blocked. The proposed method is therefore also helpful in investigating what is the minimum time the RSC will remain blocked under different initial conditions and fault severity and if the RSC is likely to block at all during the fault.

Another interesting issue emerging from the analysis is that the DFIG with chopper protection presents an equivalent crowbar resistance increasing with decreasing severity of the fault and with lighter loading conditions. Therefore, the DFIG with chopper protection delivers lower current the less severe the voltage dip caused by the fault and the lower its initial loading. A comparison between the short-circuit current of a DFIG with chopper protection and a DFIG with crowbar protection is shown in Figure 4.16. The crowbar resistance is chosen to be equal to the case presented in Figure 4.10, i.e. about 34 times the rotor resistance. The reason why this value has been chosen is that it results in the same short-circuit current magnitude as the one delivered

by a DFIG with chopper protection for a short-circuit at the DFIG terminals, while this is close to full load, as shown in Figure 4.10. This may actually be a too high value for a crowbar resistance. In (Akhmatov 2005) a crowbar resistance equal to 20 times the rotor resistance in suggested. Despite this fact, it is seen in Figure 4.16, that that the DFIG with chopper protection would deliver a lower short-circuit current compared to the crowbar protected DFIG, for a fault at the DFIG terminals with light initial loading corresponding to the same conditions as in Figure 4.14.
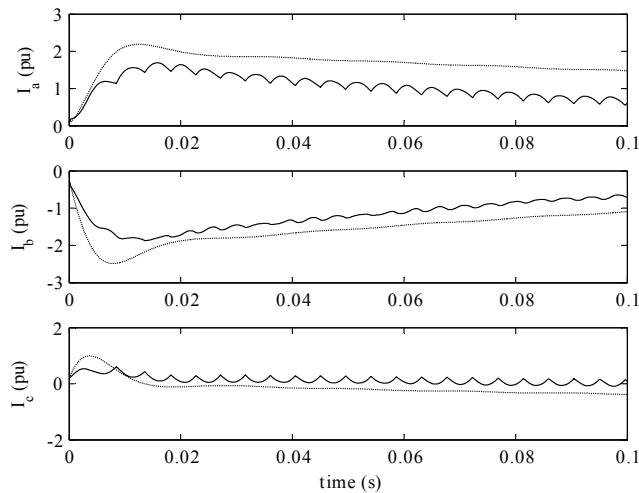
Figure 4.16 Three-phase currents of DFIG with DC chopper (solid) and crowbar (dotted) protection during a three-phase fault with parameter $p=1$. Crowbar resistance is 0.0345 Ω, i.e. about 34 times the rotor resistance. Initial apparent power $S=0.19+j0\ pu$, $\omega_r=0.76\ pu$.

4.6   Summary

A DFIG using only chopper protection on the DC-link along with RSC blocking has been analyzed under symmetrical fault conditions. It has been shown that the DC-link system, made up of the DC-link capacitor and chopper protection, during three-phase fault conditions is equivalent to an external resistance added to the rotor circuit. Therefore, the symmetrical fault behavior of a DFIG with chopper protection is equivalent to the behavior of a DFIG with crowbar protection.

A method for calculating the equivalent resistance has been proposed. Even if

in theory, a time varying equivalent resistance should be considered, it has been shown that the use of a fixed equivalent resistance leads to good fault current prediction under different fault and initial loading conditions. The equivalent resistance value increases with decreasing DFIG initial loading and decreasing fault severity. Therefore, accurate fault current prediction requires the use of a different equivalent resistance for each different fault and initial loading.

An important consequence is that the DFIG with chopper protection delivers less fault current than a DFIG with crowbar protection. The lower the DFIG initial loading and fault severity, the lower the short-circuit current delivered by the DFIG with chopper protection when compared to the one delivered by a DFIG with crowbar protection.

The theoretical analysis has been confirmed by simulation results. Results from different fault cases and operating conditions are reported, showing that the DFIG with chopper protection delivers a short-circuit current with a predominant DC component and with a very fast decaying transient AC short-circuit current component.

The proposed method allows representing a DFIG with chopper protection with an equivalent model of a DFIG with crowbar protection both for short-circuit current calculations and for short-circuit simulation studies. The advantage in using a model of a DFIG with crowbar protection, when simulating, is that it is a standard model usually available in power systems simulation tools, unlike the DFIG with chopper protection. Moreover, short-circuit current calculation methods for the DFIG with crowbar protection are common in the literature.

Chapter 5

Fault Currents from Wind Farms

In the previous chapters, a detailed description of the fault current of the individual SCIG or DFIG wind turbine has been presented. The scope of this chapter is to investigate the validity of a single-machine approach to predict the fault contribution of the entire wind farm. Only wind farms with SCIG and DFIG wind turbines are considered.

5.1   Introduction

Wind farms may contain a large number of wind turbines. As an example, the Rödsand 2 offshore wind farm in Denmark comprises 90 wind turbines. The internal collector system of a wind farm can be structured in various configurations (Dutta 2011). A simple wind farm configuration made up of three parallel rows, used in the simulations in this chapter, is shown in Figure 5.1.

Each section contains a number of wind turbines, connected between them by the internal wind farm cable network. Each wind turbine is equipped with a step-up transformer from low, 575 V, to medium voltage, 20 kV. At the Point of Common Coupling (PCC), the main wind farm transformer connects the wind farm to the external grid. Because of shadowing effects between wind turbines in relation to the incoming wind, wind turbines in a wind farm are usually not all producing the same output power. Moreover, the voltage may vary slightly throughout the internal wind farm cable network.

Because of these reasons at the event of a short-circuit in the grid, the individual wind turbines will be in different initial states. The question addressed here is how accurately the fault current contribution of the entire

wind farm can be predicted using an aggregate model of the whole wind
farm, i.e. using only one wind turbine with appropriate rated power and
initial conditions. The use of an aggregate model instead of the detailed
description of the wind farm saves simulation time and reduces model
complexity.

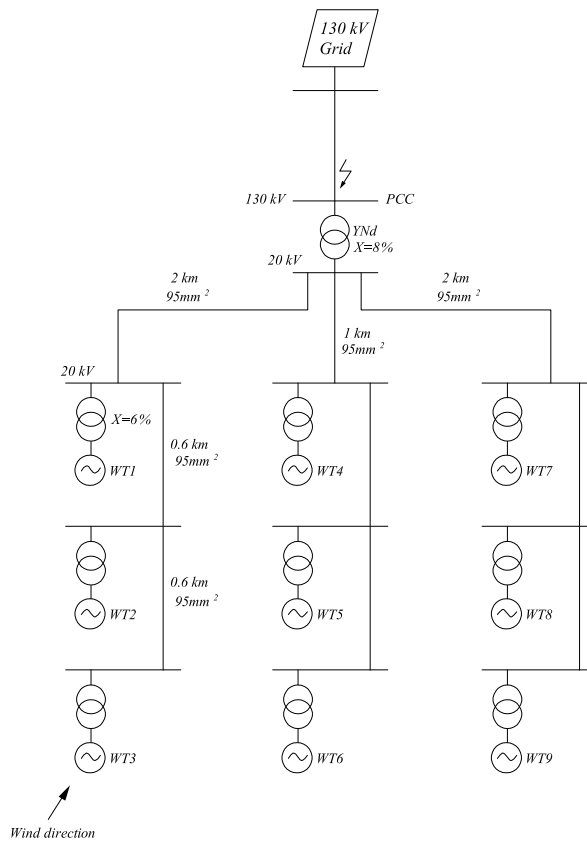Figure 5.1 Single-line diagram of detailed wind farm model with 9 wind turbines.

5.2   Detailed Wind Farm Model

A detailed model of a wind farm, as shown in Figure 5.1, has been
implemented in DigSilent PowerFactory (DigSilent PowerFactory 2010).
The wind farm is composed of three sections. Each section contains three
equal wind turbines with step-up transformer, connected to a 20 kV internal

cable network. A realistic value for the cable section for such a wind farm configuration is 95 mm^2 (Dahlgren 2006, Garcia-Gracia 2008). A 95 mm^2 aluminum cable model in the PowerFactory standard library has been used in the simulations and the parameters are reported in Table 5.1.

Table 5.1 95 mm^2 cable parameters

R (Ω/km)	0.32
X (Ω/km)	0.12

The wind turbines in the wind farm may be equipped with SCIG or with DFIG. Standard wind turbine models in the PowerFactory library have been used, but the DFIG model has been changed by adding a GSC, not implemented in the standard model. The generators are rated 1.7 MVA and their parameters are as in Table 3.1. The step-up transformers are rated 2 MVA. The main wind farm transformer is rated 20 MVA and connects the wind farm to a 130 kV external grid.

The inertia constants for the wind turbine and the generator are reported in Table 5.2. In the DFIG case, the crowbar resistance is considered to be 20 times the DFIG rotor resistance and is inserted at the same time as the RSC is blocked.

Table 5.2 Inertia constants for the wind turbine and the generator

H_{WT} (s)	4.32
H_{gen} (s)	0.62

The wind turbines have different incoming wind and they are at a different operating point before fault occurrence. The initial conditions for each wind turbine in the wind farm are reported in Table 5.4 and Table 5.5. The maximum difference between the highest and lowest active power production from the wind turbines is around 23 % of their rated power. A two-mass model is used to represent the shaft system. In the case of SCIG, a capacitor bank rated one third of total generators rating is also connected at the 20 kV common terminal.

5.3   Aggregate Wind Farm Model

The aggregate model is represented as a single wind turbine model with a rated power equal to the sum of the rated powers of the individual wind

turbines in the wind farm. The same holds for the unit transformer of the aggregate model. Determining the equivalent of a wind farm internal cable network for an aggregate model is an issue discussed in many papers. A methodology for choosing the appropriate cable parameters in an aggregate model is laid down in (Muljadi 2006) and it is applied in this chapter for determining the cable parameters for the aggregate model. Applying the method proposed in (Muljadi 2006) to the wind farm model in Figure 5.1 results in the cable parameters reported in Table 5.3 for the aggregate model.

Table 5.3 Cable parameters for the aggregate wind farm model

R (Ω)	0.213
X (Ω)	0.077

5.4   Description of Simulations

Symmetrical and unsymmetrical faults have been simulated on the 130 kV line in the network, close to the PCC. It is assumed that the wind turbine generators remain connected to the network during the whole fault duration.

The total wind farm current as measured on the 130 kV side at the PCC is reported in the next figures during symmetrical and unsymmetrical faults. This current is compared to the current measured at the same point when the detailed model of the wind farm is replaced by an aggregate model.

The aggregate model is initialized by using the maximum, the minimum or the average wind speed, as experienced by the detailed wind farm model. This is done in order to check which of these values leads to the best fault current prediction accuracy.

5.5   Simulation of a SCIG Wind Farm

The wind farm shown in Figure 5.1 has been simulated assuming all the wind turbines to be equipped with SCIG. The initial operating conditions for the wind turbines are reported in Table 5.4. The reactive power in Table 5.4 is the total delivered to the network by the generator. The cable parameters in the aggregate model are chosen as reported in Table 5.3. The total wind farm current as measured on the 130 kV side at the PCC is reported in the next figures during symmetrical and unsymmetrical faults. Fault currents are reported in pu of the main 130/20 kV transformer current. The fault occurs after 40 ms and lasts for 200 ms.

Table 5.4 Initial conditions for SCIG wind farm

	P (MW)	Q (Mvar)	v_{wind} (m/s)
WT1	1.09	-0.80	11
WT2	1.19	-0.87	11.5
WT3	1.28	-0.93	12
WT4	0.99	-0.73	10.5
WT5	1.09	-0.79	11
WT6	1.19	-0.87	11.5
WT7	0.88	-0.68	10
WT8	0.99	-0.73	10.5
WT9	1.09	-0.80	11

As seen in Figure 5.2, Figure 5.3 and Figure 5.4, the initial operating point of the SCIG wind turbine has a minor effect on its short-circuit current. In particular, the peak currents are very close in all cases. However, the best agreement with the detailed model is obtained when choosing the average wind for determining the initial condition of the aggregate model.

Figure 5.2 Simulated SCIG short-circuit current for a three-phase fault. Detailed model (black), aggregate model initialized with maximum (blue), minimum (red) and average (magenta) wind speed.

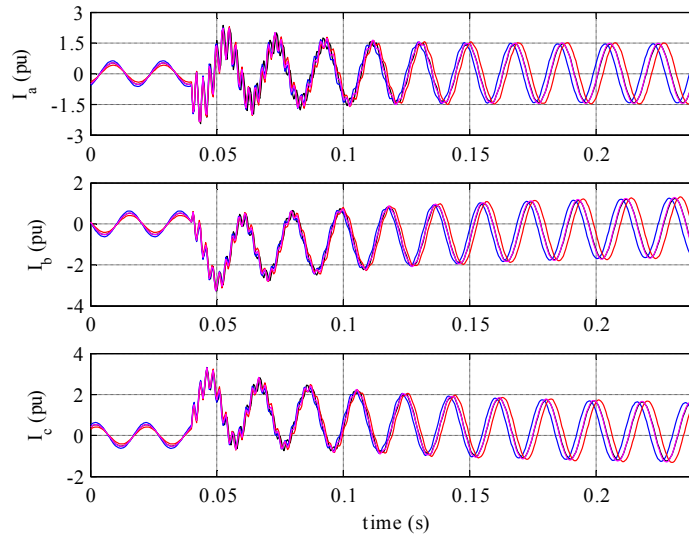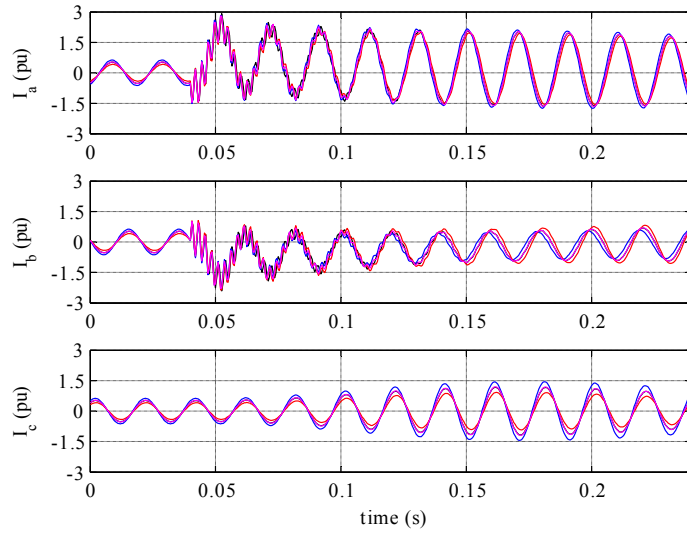Figure 5.3 Simulated SCIG short-circuit current for a phase-phase fault. Detailed model (black), aggregate model initialized with maximum (blue), minimum (red) and average (magenta) wind speed.
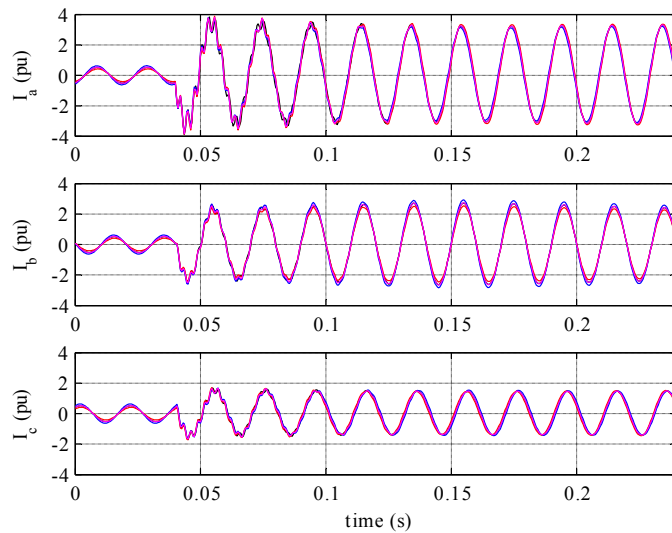
Figure 5.4 Simulated SCIG short-circuit current for a phase-*a* to ground fault. Detailed model (black), aggregate model initialized with maximum (blue), minimum (red) and average (magenta) wind speed.

The high frequency component after the fault is due to resonances between the capacitor bank and the inductances in the grid. To investigate the importance of a correct choice of the cable parameters for the aggregate model, a comparison with the short-circuit current delivered by the aggregate model disregarding the internal cable is shown in Figure 5.5. The main difference between the short-circuit current delivered by the detailed and the aggregate model without cable representation is the decay of its DC component. The DC component in the current of phase b and c decays faster in the detailed model case. The decay of the DC component is affected by the resistance of the cables in the wind farm model. Ignoring completely the cable in the aggregate model results in longer time constants for the DC component of the short-circuit currents. A too long cable, and hence high resistance, in the aggregate model results instead in shorter time constants for the DC component of the short-circuit currents.
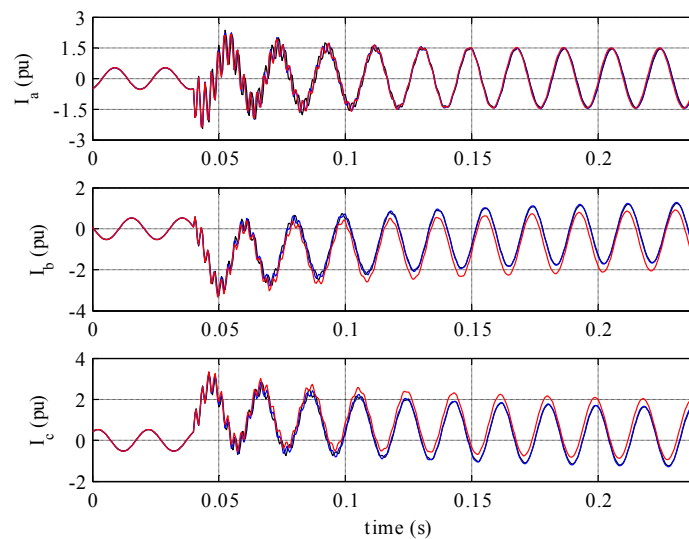
Figure 5.5 Simulated SCIG short-circuit current for a for a three-phase fault. Detailed model (black), aggregate model with cable parameters according to Table 5.3 (blue) and with no cable model (red). The aggregate model is initialized with the average wind speed.

These seem to be however minor issues. The use of a single machine equivalent leads to accurate prediction of the total SCIG wind farm fault contribution at the PCC.

5.6   Simulation of a DFIG Wind Farm

The SCIGs in the wind farm are now replaced by DFIGs with crowbar protection. Each wind turbine is initially loaded according to Table 5.5. The different loading of the wind turbines is caused by different incoming wind, and this leads to a different initial slip for each wind turbine generator. The fault occurs after 40 ms.

It is here assumed that the crowbar remains connected for a time duration of 100 ms after the fault and only this period is reported in the next figures. The period with the crowbar inserted is also the most interesting period during which the highest fault currents are delivered. When the crowbar is disconnected the RSC regains the control of the stator current and the DFIG can be seen as a constant current source, in a similar way to a FSC (Walling 2009). Notice that the crowbar may disconnect before 100 ms, depending on the magnitude of the currents and the DC-link capacitor voltage. In the case of unsymmetrical faults, special control algorithms to reduce torque or DC-link voltage oscillations can be used. The delivered fault current would then depend on this control scheme when the crowbar is disconnected. Here, it is assumed instead that the crowbar remains connected through the whole duration of the unsymmetrical fault. This is a reasonable assumption at least for severe unsymmetrical faults (Semaan 2006(b)), since the negative sequence voltage in the grid would induce high rotor currents through the whole duration of the fault.

The fault current from the detailed wind farm model is reported in the next figures along with the fault current from the aggregate model with different initial conditions.

In case of a three-phase short-circuit, the fault currents from the detailed and aggregate model are reported in Figure 5.6. The cable parameters in the aggregate model are chosen as in Table 5.3. Also in this case, the wind speed given to the aggregate model to determine the initial condition of the aggregate model affects marginally the short-circuit current. The average wind speed results however in better accuracy. From the analysis of simulation results, it is also concluded that in the detailed model, the instant in which the crowbar is inserted is roughly the same for all the generators in the wind farm.

Table 5.5 Initial conditions for DFIG wind farm

	P (MW)	Q (Mvar)	v_{wind} (m/s)	ω_r (pu)
WT1	1.06	0	11	1.13
WT2	1.17	0	11.5	1.17
WT3	1.28	0	12	1.20
WT4	0.96	0	10.5	1.10
WT5	1.06	0	11	1.13
WT6	1.17	0	11.5	1.17
WT7	0.87	0	10	1.06
WT8	0.96	0	10.5	1.10
WT9	1.06	0	11	1.13

Figure 5.6 Simulated DFIG short-circuit current for a three-phase fault. Detailed model (black), aggregate model initialized with maximum (blue), minimum (red) and average (magenta) wind speed.

The fault currents delivered by the detailed and the aggregate models for a phase-phase and a single-phase-to-ground fault are shown in Figure 5.7 and Figure 5.8.

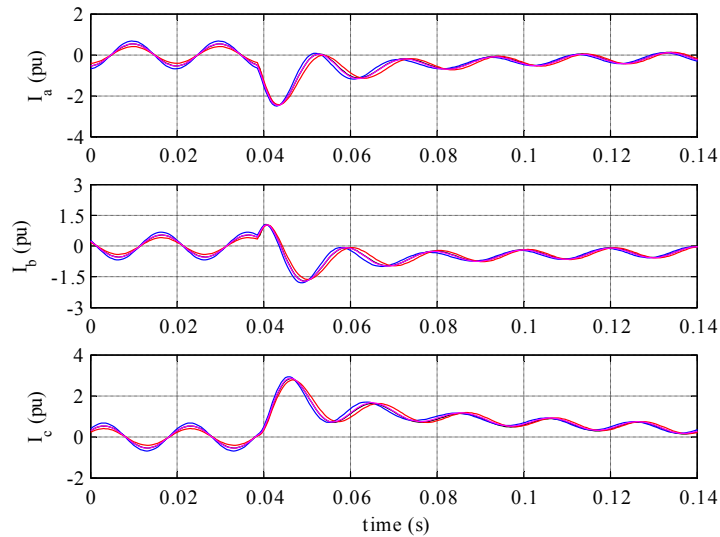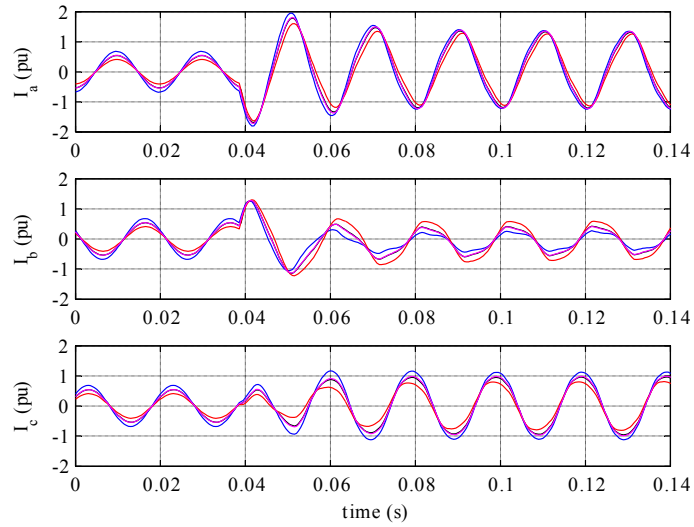Figure 5.7 Simulated DFIG short-circuit current for a phase-phase fault. Detailed model (black), aggregate model initialized with maximum (blue), minimum (red) and average (magenta) wind speed.
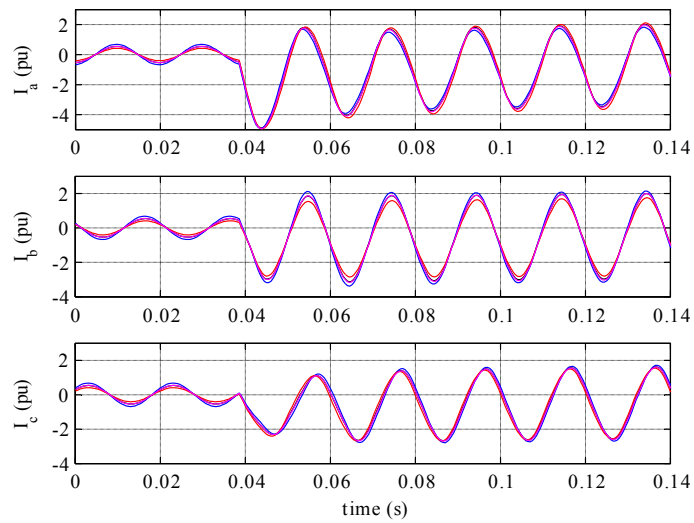

Figure 5.8 Simulated DFIG short-circuit current for a phase-*a* to ground fault. Detailed model (black), aggregate model initialized with maximum (blue), minimum (red) and average (magenta) wind speed.

The same conclusions drawn for three-phase symmetrical short-circuits also hold for unsymmetrical short-circuits. In this case, it is easier to appreciate how choosing the average wind speed in the wind farm to initialize the aggregate model results in better agreement.

In conclusion, aggregate models of DFIG wind farms can be used to accurately predict the fault current contribution of DFIG wind farms.

5.7   Summary

The use of a single-machine approach to model the total fault current contribution from a SCIG and a DFIG wind farm has been checked through simulations. The maximum difference between the lightest and heaviest loaded generator in the farm is assumed to be around 23 % of the nominal power of a generator.

Both for SCIG and DFIG wind farms, the use of an aggregate model to predict the short-circuit current contribution of the entire wind farm leads to accurate results for symmetrical as well as unsymmetrical faults. As long as the aggregate model is initialized with a wind speed in the range between the minimum and maximum wind speed experienced in the wind farm by the individual generators, the initial condition of the aggregate model does not significantly affect the short-circuit current. Initializing the aggregate model with the average wind speed in the wind farm leads to best accuracy. For DFIG wind farms, this is true at least in the first cycles after the fault, during the period the crowbar is inserted and the RSC is blocked.

Ignoring completely the cable network in the aggregate model leads to a slower decay of fault current DC component. The aggregate model should therefore be interconnected to the grid with a cable, whose parameters are to be chosen to achieve same DC component decay rate as for the detailed wind farm model.

Chapter 6

GFRT for Faults below Transmission Network

Swedish grid code (SvKFS 2005:2) requires GFRT of wind turbines for faults at transmission level, above and included the 220 kV network, cleared within maximum 250 ms by the protection system. Different requirements are set for wind farms below and above 100 MW. Document (TR2-05-2-1 2010) by the Swedish TSO states that line faults on the transmission level should be cleared instantaneously with a maximum fault clearing time of 130 ms. This assumes that communication between the two line ends is used. In case of intervention of the circuit breaker failure protection, the maximum clearing time is required to be 250 ms. Fault clearing times below the transmission level are often longer than at transmission level, due to different employed protection systems. At sub-transmission level communication is not always used, resulting in longer fault clearing times. Therefore, it is not certain that a wind turbine which respects grid code requirements for faults at the transmission level is also able to ride-through faults below transmission level. This issue is further treated in this chapter.

6.1   Introduction

An investigation on the voltage dip profiles resulting from faults at sub-transmission and medium voltage level and on their effect on GFRT of wind turbines is performed in this chapter. In Sweden there is actually no requirement for wind turbines to ride-through faults below transmission level. The voltage-time curve defined in the Swedish grid code is in fact applicable to points on the transmission network following a fault at the same network level. Wind turbines connected below the transmission network must ride-through such faults causing voltage dips at the connecting transmission network buses above the Swedish GFRT curve. To assess whether the GFRT of wind turbines is compromised for faults at sub-

transmission and medium voltage level, reasonable assumptions on their ride-through capability must be made. The voltage-dip profiles obtained from simulations can then be checked against these assumptions to evaluate the GFRT of wind turbines.

A possible way to assess GFRT of wind turbines is to use the Swedish voltage-time curve and let it represent the minimum GFRT requirement at the connection point for faults below transmission level. Using the Swedish voltage-time curve as a reference for GFRT assessment in this chapter is justified since wind turbines connected sufficiently close to the transmission network may experience voltage dips not very different from the ones experienced in the transmission network during faults in that network. As a matter of fact, for such faults the voltage dip experienced by wind turbines connected close to the transmission network may even be lower than the one experienced in the transmission network. In these cases, wind turbines complying with the Swedish grid code can also be assumed to be capable of GFRT for faults below transmission level causing voltage dip profiles at the connection point above the Swedish voltage-time curve.

It is reasonable to assume that commercial wind turbines are able to ride-through voltage-time curves defined in other national grid codes and applicable at the connection point, which may be either at transmission or distribution level. The voltage-time curves in the Danish and German (E.ON) grid code are two such examples.

The aim of the Swedish GFRT curve is to safeguard the integrity of the power system for large disturbances, as a fault on the transmission system. As already said, for wind turbines connected sufficiently close to the transmission system, the Swedish GFRT curve can also be assumed to be representative of the minimum GFRT requirement at the connection point. It is not surprising if wind turbines complying only with this minimum requirement would not ride-through some of the fault cases at sub-transmission and medium voltage level considered in this chapter. It is expected instead that wind turbines complaining with the Danish and E.ON voltage-time curves, defined even for faults below transmission level, would ride-through the faults considered in the simulations in this chapter.

These three curves will be used as a reference in this chapter to evaluate GFRT of wind turbines for faults below transmission network.

A similar analysis to the one in this chapter has been carried out in (Coster 2009) for ride-through of CHP plants, but without taking into account the

load dynamics which is instead central in this work. The authors of the mentioned paper do not focus on the post-fault voltage recovery and they do not relate the resulting voltage dips to any GFRT curve.

In Section 6.2, an analysis is performed on the extension of the network area where the wind turbine GFRT capability could be endangered during a fault on sub-transmission network. To address this question, the value of the voltage dips at different buses in a network can be calculated using standard power system analysis methods. This analysis can be used to estimate the total amount of wind power expected to be disconnected following such a fault, once the total amount of wind power connected to a sub-transmission bus is known. This analysis is however not sufficient and must be completed by dynamic simulations to account for the dynamic load effects on voltage recovery.

The influence of the load mix composition on the voltage recovery after fault clearing is then addressed. It is shown that load mix composition and its dynamic behavior play a crucial role for GFRT when the fault is below transmission network. The presence of dynamic loads, induction motors, worsens the voltage recovery in the network after fault clearing (Taylor 1994). A realistic analysis should moreover consider also the amount of dynamic load that is tripped during the voltage dip. Industrial induction motors may trip during voltage dips due to the release of the trip contacts of the AC contactor (Taylor 1994). However, the amount of dynamic load disconnected during a dip, the value of the voltage and time at which disconnection happens are all unknown variables and therefore reasonable scenarios must be used instead (Taylor 1994, Transpower 2009).

Simulations of some test cases are performed in DigSilent PowerFactory (DigSilent PowerFactory 2010) to find out the voltage dips resulting from different fault and load scenarios. The results are shown after an introduction on the system, protection and load modelling assumptions.

6.2   Network and Components Modelling

The network used in this chapter is the Nordic 32 network model (CIGRÉ 1995). However, this study focuses only on a small part of this network, a 130 kV ring composed of 5 nodes, *1041* through *1045*. This part of the network is shown in Figure 6.1. Dynamic simulations are carried out in DigSilent PowerFactory.

The 130 kV ring is connected with the 400 kV transmission network at two

points. Some modification to the original Nordic 32 model have been done
in this 130 kV system. Two extra 130 kV nodes, *6* and *7*, have been added
compared to the original model. A medium voltage network with two feeders
has been added to bus *1041* with a wind farm model connected to it. The
loads in the system were originally of static type. They have been modified so
that a certain percentage is represented as impedance load and the remaining
part as induction motor load. The total steady-state active power drawn by
the loads is still unchanged and extra capacitor banks have been added to
compensate the extra reactive power needed by the motor loads. The motor
load is represented using a standard model in PowerFactory with a
mechanical load varying quadratically with rotor speed.
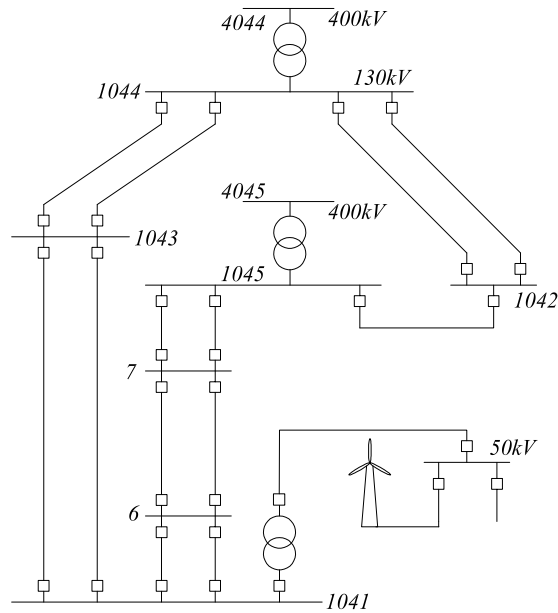
Figure 6.1   130 kV system used in the simulations. The system is originally part of
the Nordic 32 model, but it has been modified by adding buses *6, 7* and
a 50 kV network with two feeders.

Protection system

The protection system on the 130 kV network is assumed to be made up
primarily of distance protections without any communication. Distance
protection with 3 different zone settings is considered. For short-circuits
without earth involved, the delay times of the distance protection are assumed

to be as in Table 6.1.

Table 6.1 Intentional delay times for different zones of distance protection

	Zone 1	Zone 2	Zone 3
Delay time	0 s	0.4 s	1.2 s

Zone 1 is assumed to cover up to 80 % of the line length. Zone 2 covers up to 120 % of the line length. Two main protections are assumed to be installed so that the probability of protection failure is negligible. Failure of a circuit breaker is dealt with circuit breaker failure protection, CBF (Horowitz 1995). It is assumed that the total clearing time with CBF protection operation is 250 ms.

Distance protection with communication or differential protection may be used or needed in case of short lines, when the line distance is too short to achieve selectivity with only distance protection. However, this kind of protections is not considered in this study.

The total fault clearing time is given by the sum of the intentional delay times of the protection relay, plus the time necessary for the protection relay to detect a fault and the breaker opening time. The time necessary for the protection relay to detect a fault may vary depending on the type of relay and the algorithm it is based on. A realistic value is 1.5 cycles, i.e. 30 ms (ABB REL650). Here, it is assumed that the protection relay operating time is 40 ms. A realistic value for a 130 kV circuit breaker interrupting time is 3 cycles, i.e. 60 ms (ABB Type PMI). The total sum of relay operating time and circuit breaker interrupting time is therefore assumed here to be equal to 100 ms. This time must be added to the intentional delay times indicated in Table 6.1.

Load modelling

Three different cases for the load composition mix are considered. In the first case, the load is assumed to be entirely of impedance type. In the second case, 30 % of the load is assumed to be dynamic load and the remaining 70 % impedance load. In the third case, half of the load is modelled as dynamic and half as impedance load.

Modelling of dynamic load with static models is not accurate for large voltage variations (Taylor 1994). Therefore, the dynamic load is represented with the detailed model of an induction motor driving a mechanical load with torque

increasing quadratically with speed. In reality, industrial motors are automatically disconnected from the network when the voltage drops below a certain level for a certain time. The disconnection is due to the de-energization of the AC contactors used to connect the motor to the grid. The drop-off voltage may vary between 30 and 65 % of nominal voltage (Taylor 1994). Induction motors used in small appliances, mainly single-phase, will not be disconnected due to under-voltage but they are solely protected against overload.

Dynamic load will worsen the voltage profile during a fault because of the high amount of reactive power they absorb. The electromagnetic torque produced by induction motors is proportional to the square of the voltage, thus a voltage drop strongly decreases the produced motor torque leading to a deceleration of the motor with consequent higher absorption of reactive power. If the voltage is not restored, the motor could come to a stall. Disconnection of motor load during voltage drops is beneficial to voltage stability. It is assumed that either 25 % or 50 % of the total motor load is disconnected during the voltage dip. The disconnection is performed when the voltage drops below 0.5 pu with a time delay of 100 ms. Only those motors connected to the buses experiencing sufficient voltage drop are hence disconnected.

The amount of dynamic and static load is chosen in each case, so that in steady-state the total active power drawn by the load in the system is unchanged, i.e. if a certain amount of dynamic load is added, a corresponding amount of static load is disconnected. The reactive power drawn in steady-state by the motor load is compensated locally with capacitor banks.

6.3   Voltage dip calculation

In (Souza 2010) it is shown how the vulnerability area technique can be used to assess the effect of voltage dips in the grid on the GFRT of wind turbines. The technique basically gives the voltage dip magnitude at a grid location for short-circuits applied throughout the whole system. If this technique is combined with statistical data on fault rates, the expected frequency for wind turbine disconnections following a fault can be found.

In general, to calculate the voltage dip magnitude at different buses in the sub-transmission network given a fault at a certain bus, standard matrix calculation methods can be employed (Glover 2002). The result will give a first indication on which buses are seriously affected by the voltage dip and therefore an estimation of the amount of wind power that may experience

GFRT problems. Once the network structure is known, the bus admittance and impedance matrices, *Y* and *Z*, can be calculated. If the fault is at bus *k*, the voltage at bus *n* is given as:

$$V_n = \left(1 - \frac{Z_{kn}}{Z_{nn}}\right) V_{pre-fault} \qquad (6.1)$$

This approach has been followed here and the results are shown in Figure 6.2 along with the values obtained through simulations in PowerFactory. It is noted that in these simulations, only static loads have been considered.
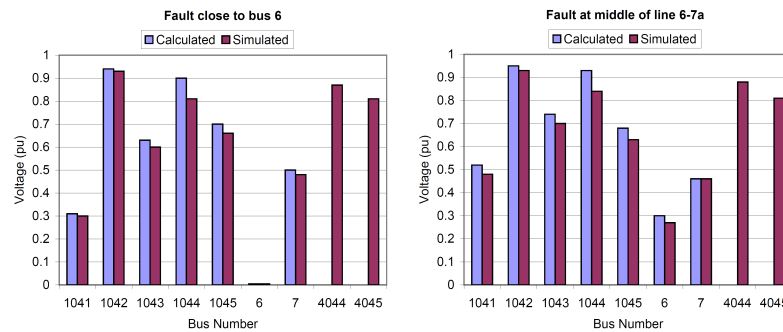
Figure 6.2 Voltage dip magnitudes for two different three-phase faults.

As seen, the calculated results are quite close to the simulated values. These results indicate that in the considered network, only the buses close to the fault experience voltage dips that could endanger the GFRT of wind turbines.

These results are however only rough and do not take into account any dynamic aspect. Also, the severity of the dip must be combined with the duration of the dip to make any assertion on GFRT of wind turbines. The duration of the fault depends on the protection system. Faults not correctly cleared by the protection system may cause failure to ride through the fault even if the voltage dip is not particularly deep.

6.4   Faults at sub-transmission network

The aim of this paragraph is to find out how voltage dips following a set of considered fault events on the sub-transmission network look like and to evaluate if they pose any risk to GFRT of wind farms eventually connected in the vicinities of the faults.

The voltage dip recovery in the grid is affected by the load mix composition. The voltage recovery will directly impact on the GFRT capability of connected wind turbines. Three different composition mixes are analyzed, with the dynamic load making up respectively 0 %, 30 % and 50 % of the total load. Moreover, two scenarios are considered for the dynamic load with regard to the amount of motor load disconnected during the voltage dip. In the first case only 25 % of the initial motor load is disconnected and in the second case 50 % is disconnected.

Different short-circuit cases on line *6-7a* between buses *6* and *7* and on line *1-6a* between buses *1041* and *6* are considered, see Figure 6.3. The total clearing time depends on where on the line the short-circuit is located and on the correct operation of the circuit breaker. Normal cases in which the protection and the breaker behave as expected are considered along with cases in which the circuit breaker fails to open and the CBF protection opens all the other breakers connected to the same bus. The considered cases are reported below with the total fault clearing times.

The analysis focuses on the voltage dip profiles on the *50 kV* bus, see Figure 6.1, to which a wind farm is connected during the simulations. The resulting voltage dip profiles are then compared to the Swedish, German (E.ON) and the Danish GFRT voltage-time curves. This will give an indication on whether wind turbines are capable of GFRT.

Fault at 50 % of line *6-7a*, Case 1

The fault is in this case applied in the middle of one of the two parallel lines, line *6-7a*, between buses *6* and *7*. In the case in which the protection relays and the breakers behave correctly, the total fault clearing times are reported in Table 6.2. The distance protections at both ends of the line see a fault in Zone 1, triggering a trip signal without time delay.

Table 6.2 Normal fault clearing times (FCT) for a fault in the middle of line *6-7a*

	B67a	B76a
FCT	0.1 s	0.1 s

The case in which breaker B67a fails to open leads to the CBF protection opening breakers B61a, B61b and B67b. The total fault clearing times are in this case reported in Table 6.3.

Table 6.3 FCT for a fault in the middle of line *6-7a*. CBF protection operation

	B67a	B76a	B61a	B61b	B67b
FCT	-	0.1 s	0.25 s	0.25 s	0.25 s
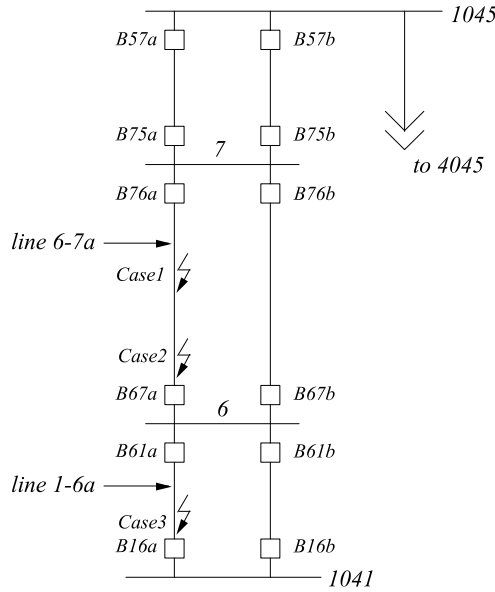
Figure 6.3 Part of the 130 kV system with three different considered fault cases. Buses *1041* and *1045* are further connected with other 130 kV buses, not shown in this figure (see Figure 6.1).

Fault at 1 % of line *6-7a, Case 2*

The fault is in this case applied close to one end of line *6-7a* between buses *6* and *7*, close to bus *6*. In this case, only the distance protection close to the fault will intervene in Zone 1, while the protection at the other line end will intervene in Zone 2. The total fault clearing time is therefore longer than in the previous case, see Table 6.4.

Table 6.4 Normal FCT for a fault near bus *6* end of line *6-7a*

	B67a	B76a
FCT	0.1 s	0.5 s

In case breaker B67a fails to open, breakers B61a, B61b and B67b will open triggered by the CBF protection. The fault clearing times in this case are reported in Table 6.5.

Table 6.5 FCT for a fault at the beginning of line *6-7a*. CBF protection operation

	B67a	B76a	B61a	B61b	B67b
FCT	-	0.5 s	0.25 s	0.25 s	0.25 s

Fault at 1 % of line *1-6a*, *Case 3*

The fault is in this case applied close to one end of line *1-6a* between buses *1041* and *6*, close to bus *1041*. Only the case of correct operation of the protection system is analyzed. The distance protection close to the fault will intervene in Zone 1, while the protection at the other line end will intervene in Zone 2. The total fault clearing time is reported in Table 6.6. This case is analogous to *Case 2*, but with a more severe voltage dip at bus 1041.

Table 6.6 Normal fault clearing times for a fault at the beginning of line *1-6 a*

	B16a	B61a
FCT	0.1 s	0.5 s

6.5   Simulation Results

Five different short-circuit cases with normal or circuit breaker failure protection operation have been considered. For each short-circuit case, five different load scenarios have been taken into account, resulting in a total amount of 25 simulated cases. All simulations have been performed in DigSilent PowerFactory as instantaneous value simulations.

Fault at 50 % of line *6-7a*, *Case 1*

The voltage dip profiles at the *50 kV* bus for a fault in the middle of line *6-7a* are reported in Figure 6.4 and Figure 6.5.

In Figure 6.4 the protection system and the breakers operate correctly and clear the fault according to the fault clearing times in Table 6.2. In this case, the voltage dip profiles at the *50 kV* bus are well within all of the three considered GFRT curves. This is true independently of the load mix composition in the network.
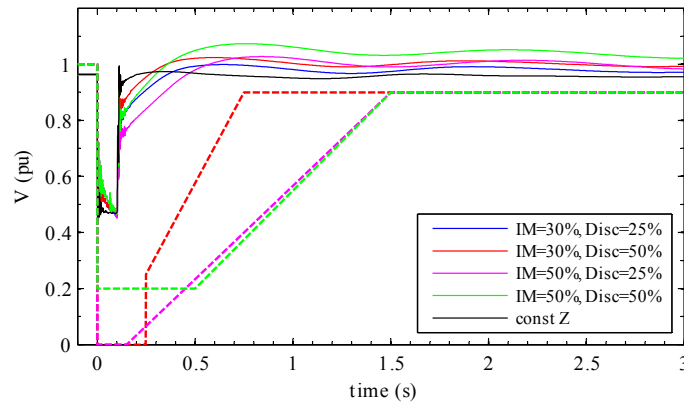
Figure 6.4 Fault at 50 % of line *6-7a*, *Case 1*. Correct fault clearing. Swedish (red dashed), E.ON (magenta dashed) and Danish (green dashed) GFRT curve.

Figure 6.5 Fault at 50 % of line *6-7a, Case 1*. CBF protection operation. Swedish (red dashed), E.ON (magenta dashed) and Danish (green dashed) GFRT curve.

In the case shown in Figure 6.5 instead, the three GFRT curves are violated for the most severe load case. The wind turbines may therefore disconnect in this case. However, this last case is representative of a voltage instability phenomenon. When the voltage in the system remains low for long periods, overloading of induction motors may occur but their disconnection, which would help voltage restoration, may take up to several seconds (Taylor 1994). It is important therefore to consider the dynamic effects of load on the

voltage to assess if wind turbines could ride through the fault.

Fault at 1 % of line *6-7a*, *Case 2*

The voltage dip profiles at the *50 kV* bus for a fault on line *6-7a* close to bus 6 are reported in Figure 6.6 and Figure 6.7.

Figure 6.6   Fault on line *6-7a* close to bus 6, *Case 2*. Correct fault clearing. Swedish (red dashed), E.ON (magenta dashed) and Danish (green dashed) GFRT curve.
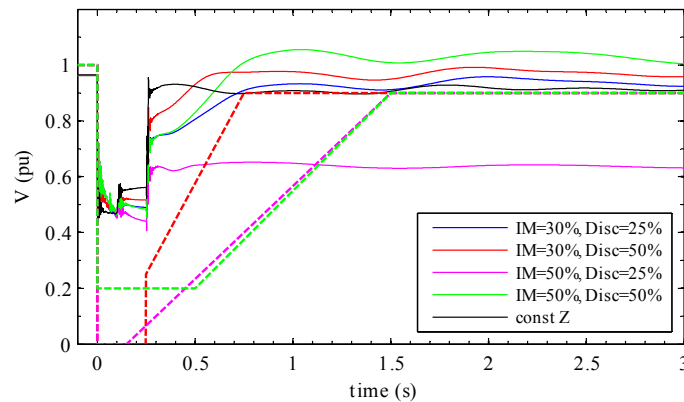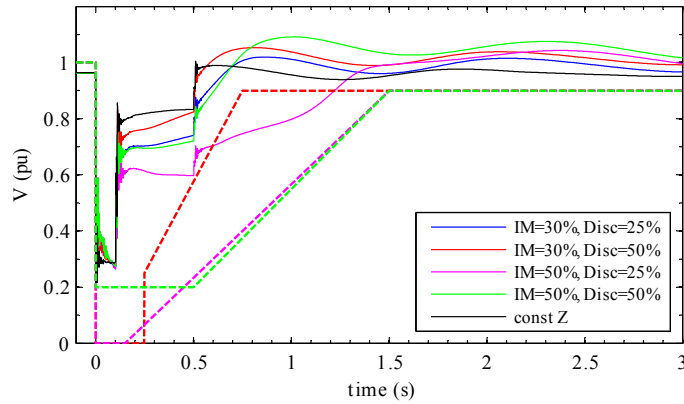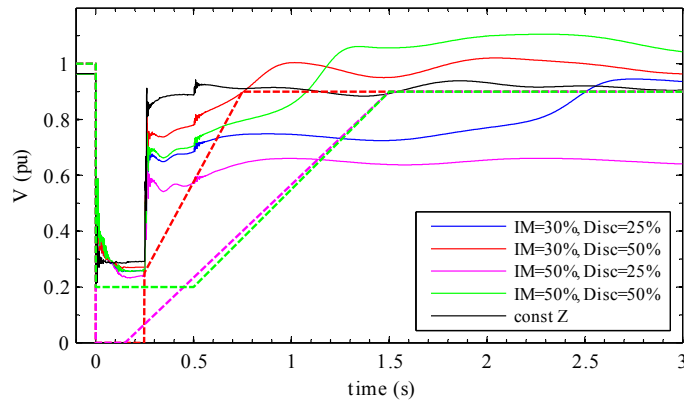

Figure 6.7   Fault on line *6-7a* close to bus 6, *Case 2*. CBF protection operation. Swedish (red dashed), E.ON (magenta dashed) and Danish (green dashed) GFRT curve.

In this case, GFRT is mainly endangered when the fault is cleared by the

CBF protection, with the clearing times in Table 6.5, and with the most severe load cases. If the fault is cleared by normal operation of protection relays, only the heavier load case leads to temporary violation of the Swedish GFRT curve.

Fault at 1 % of line *1-6a, Case 3*

In this case even if the fault is cleared correctly, three load cases lead to temporary violation of the Swedish GFRT curve while the E.ON GFRT curve is violated only for the most severe load case. Note that the Danish GFRT curve does not require zero voltage ride-through and it is violated for a close-in three-phase fault. The voltage recovery is now clearly worst than the analogous case shown in Figure 6.6, being the fault closer to the *50 kV* considered bus.
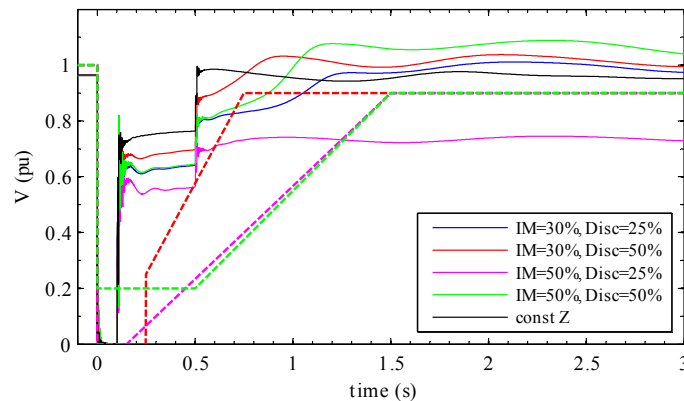
Figure 6.8   Fault on line *1-6a* close to bus *1041*, *Case 3*. Correct fault clearing. Swedish (red dashed), E.ON (magenta dashed) and Danish (green dashed) GFRT curve.

Voltage dip at other buses

The voltage at other buses in the network are plotted in Figure 6.9 for the worst case scenario found above. This is a fault at the beginning of line *6-7a* closed to bus *6* cleared by CBF protection and shown in Figure 6.7. The motor load is 50 % and only 25 % of the initial load is disconnected during the fault.

It is found that violation of the GFRT curves happens only on buses *1041* and *1043*, except obviously buses *6* and *7* close to the fault. Wind farm connected at other buses would not experience any GFRT problems.
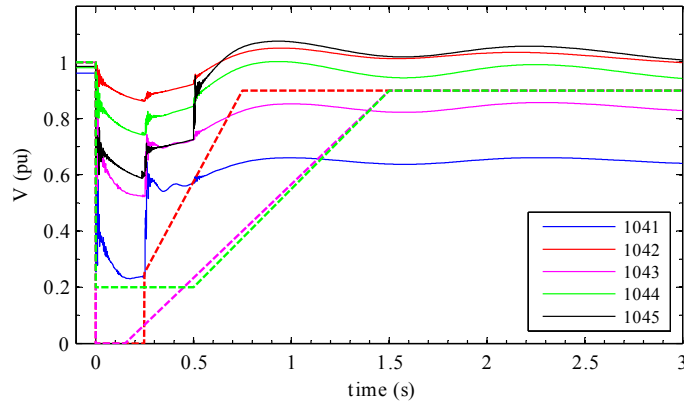
Figure 6.9   Fault on line *6-7a* close to bus *6*, *Case 2*. CBF protection operation. Swedish (red dashed), E.ON (magenta dashed) and Danish (green dashed) GFRT curve.

6.6   Faults at Medium Voltage Network

In this paragraph, it is investigated the GFRT of wind turbines during a fault on an adjacent feeder on the 50 kV medium voltage network. The fault is supposed to be cleared by the feeder overcurrent protection in 1 s. Only the worst case load mix scenario, as suggested by the previous simulations, is considered. The motor load is 50 % of the network load and of this, only 25 % is disconnected during the fault.

The length of the feeder where the fault is applied is 10 km. A load is connected at the end of the feeder. The cases of a fault at the beginning and at the end of the feeder are both considered. The resulting voltage dips are shown in Figure 6.10 for the *50 kV* bus and for buses *1041* and *1043*.

A close in fault on an adjacent feeder is a severe fault that endangers the GFRT capability of wind turbines on the same medium voltage network. Such a fault causes also violation of the Swedish GFRT curve on the 130 kV buses *1041* and *1043*, showing that a fault on the 50 kV network could cause GFRT problems also in other medium voltage networks tapped from different, but close, 130 kV buses, if wind turbines are just able to comply with the minimum GFRT requirements. However, the voltage dip at buses *1041* and *1043* does not violate the E.ON and Danish GFRT curves. These avoid therefore disconnection of wind turbines at the adjacent 130 kV buses.

A fault at the end of the 10 km feeder causes violation of the Swedish GFRT

curve at the 50 kV network and at bus *1041*, but it does not violate the GFRT curve at bus *1043*. The violation of the E.ON and Danish GFRT curves at the *50 kV* bus is only marginal and this indicates that wind turbines connected to parallel feeders on the same medium voltage network may still remain connected if they comply with the E.ON and Danish grid codes.
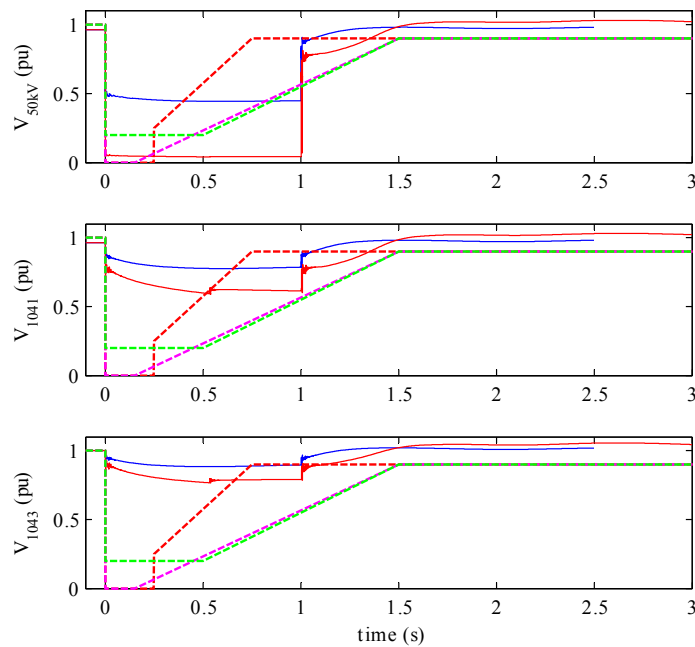
Figure 6.10 Fault at end (blue) and beginning (red) of 50 kV feeder. Swedish (red dashed), E.ON (magenta dashed) and Danish (green dashed) GFRT curve.

6.7   Summary

An investigation on GFRT of wind turbines during faults below the transmission network has been performed in this chapter.

The extension of the area where a voltage dip following a fault in the sub-transmission network may cause GFRT problems has been first studied analytically. The analysis on the chosen test system shows that in sub-transmission networks only the buses close to the fault would experience voltage dips that could compromise GFRT. The way the dips would then

propagate to the point of common coupling of wind farms in a medium voltage network, tapped from the severely affected sub-transmission buses, depends on the topology of the medium voltage network.

This information alone is however not enough to assess the GFRT performance of wind turbines and must be supported by dynamic simulations. Load modelling is a central issue when investigating wind turbine GFRT, since it has a strong impact on the voltage recovery after fault clearing. It has been shown that cases, in which no GFRT problems would arise if a constant impedance load model is used, instead prove to endanger the GFRT capability of wind turbines if a more realistic load mix including dynamic loads is used.

It is mainly during faults cleared by circuit breaker failure (CBF) protection and under high motor load conditions that wind turbine GFRT could be compromised for faults at sub-transmission networks. Circuit breaker failure is however a rare event.

Faults on medium voltage adjacent feeders seriously endanger the GFRT of wind turbines connected in the same network. The most severe faults on a medium voltage feeder may cause GFRT problems also on other sub-transmission buses and medium voltage networks tapped from these sub-transmission buses. Among the considered GFRT curves, the E.ON and Danish ones proved to be more robust for the GFRT of wind turbines following a fault on the medium voltage network. Wind turbines complying with these grid codes could even ride through faults at the remote end of adjacent parallel medium voltage feeders.

Chapter 7

Wind Turbines Voltage Support in Weak Networks

In this chapter, it is investigated how wind turbines can contribute to voltage support in weak networks during faults. Voltage recovery in weak networks may be slow, especially if a consistent portion of the local load is constituted by induction motors. Fixed-speed wind turbines with induction generators also cause slow voltage recovery. Variable-speed wind turbines connected in weak networks are instead an asset that can be exploited to improve the post-fault voltage recovery, therefore helping the nearby connected loads to return faster to operating conditions close to normal and reducing component stresses.

7.1   Introduction

Many national grid codes require wind turbines to be able to ride-through faults in the network causing a voltage dip at the Point of Common Coupling (PCC) above a specified voltage-time characteristic. Moreover, wind turbines must also be able to inject reactive power into the grid to help voltage recovery after fault clearing. The amount of reactive power to be injected may vary in different grid codes.

Modern wind turbines are able to improve the grid voltage if required so. Few grid codes also require that wind turbines should be equipped with voltage control capability (Martinez 2011(c)). Voltage control capability is technically achievable even if not required by present grid codes.

Three main issues are addressed in this chapter:

1. How the voltage support of wind turbines depends on the short-circuit power and the *X/R* ratio at the connection point of the weak grid.

2. Possible ways to improve wind turbine voltage support in weak networks.

3. How wind turbine voltage support performs when compared to the one supplied by a power plant with synchronous generation.

In order to address these issues, a review on wind turbine voltage support and an analysis of voltage support limits are first briefly introduced. An analysis on active and reactive power coordination is then described together with different strategies for voltage support during faults considered in the simulations in this chapter. The performance of each of these strategies is evaluated through simulations of a simple test system. Finally a comparison between the voltage support of wind turbines and a power plant with synchronous generation is done by using a simplified model of the real power system of the Danish island of Bornholm.

7.2   Wind Turbine Voltage Support

A brief overview of some grid code requirements for voltage support and a literature review on wind turbine voltage support in weak grids are presented in this section.

Grid Codes Requirements

Some grid codes require voltage support from wind turbines during a fault event in the grid. The Danish and German (E.ON) grid codes require wind turbines to feed into the grid a reactive current proportional to the voltage drop at the PCC. The reactive current is increased proportionally to the voltage deviation until current limit is reached. Moreover, a voltage deadband is defined within which the wind turbine ceases any reactive power supply. The reactive current injection characteristic for the Danish and E.ON grid codes are shown in Figure 7.1.

Note that the Danish grid code requires no reactive current injection at the deadband lower limit, while the E.ON grid code requires 0.2 pu reactive current. E.ON grid code prescribes a minimum proportional gain equal to 2. The E.ON grid code also states that reactive power support has to be continued for a further 500 ms after the voltage returns into the deadband, in accordance with the shown characteristic.

Supply of reactive current has priority over active current outside the

deadband. The Danish grid code does not have any requirement on active power ramping after fault clearing. E.ON grid code requires active power ramping after fault clearing with at least 20 % rated power per second. Grid codes in UK and Ireland require a post-fault active power ramp of at least 90 % rated power per second.
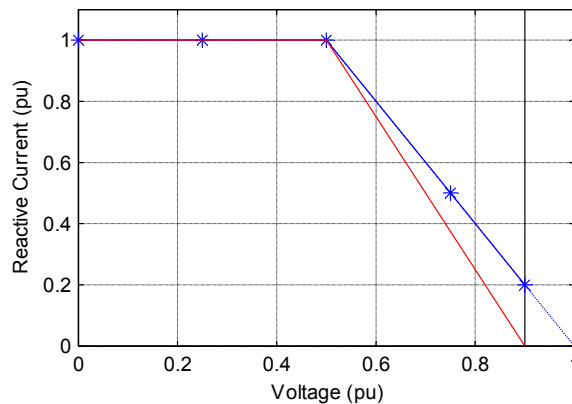

Figure 7.1   Reactive current support as required by E.ON (blue *) and Danish (red) grid codes.

Other national grid codes do not require explicit voltage support from wind turbines during faults. This is the case for example of the Swedish and Spanish grid codes.

Research on Wind Turbines Voltage Support

Alternative approaches for wind turbine voltage support have been investigated in the literature. In (Neumann 2011), the authors do not focus on the voltage recovery process but mainly on the voltage during the fault. Increasing the proportional gain over 2 may result in higher voltage during the fault. However, further increase of the gain may not result in further improved performance, because of the limitation on maximum current. Reactive power support without a voltage deadband is also proposed in the mentioned reference to speed-up voltage control and to allow the controller to react also to small voltage variations. In (Shewarega 2009) it is also concluded that no deadband and high proportional gain improve the post-fault transient performance in the system. The effects of different proportional gains on voltage recovery is investigated also in other papers (Ullah 2007, Ashkhane 2011), showing that an increase of the gain up to 6 significantly reduces the voltage recovery time. (Ashkhane 2011) also includes

a motor load in his studies.

Another interesting result in (Ashkhane 2011) is that voltage recovery is faster with a STATCOM than with a wind turbine, even if they have comparable reactive power dynamics. The author suggests that a possible cause for this phenomenon is the active power injection of a wind turbine that causes extra voltage drop compared to a STATCOM. Also in (Shewarega 2009) the active power injection is pointed out as a possible cause that deteriorates the voltage recovery and a strategy for reducing the active power injection is proposed. In (Kayicki 2007) it is shown how prioritizing active, instead of reactive, power injection leads to higher voltage during faults in grids with low X/R ratio. A coordination of reactive and active power injection seems therefore beneficial to voltage recovery and will be further investigated in this chapter.

In (Martinez 2010) the authors point out that in the case a wind farm is connected through a long line to the PCC, a particular active current control should be adopted to maximize the reactive current injected at the PCC, as a consequence of the fact that a reactive current injected from a wind turbine is not a pure reactive current at the PCC because of the voltage angle differences at the two locations.

In other articles (Michalke 2010, Aghatehrani 2009, Kayikci 2007, Strachan 2010) a proportional-integral (PI) controller is proposed for voltage control at the PCC. However, application of a PI controller in a wind farm with many wind turbines may result in "hunting" problems (Ashkhane 2011, Martinez 2011(c)). Even in the case the voltage would be controlled by a central wind plant controller that subsequently sends a reference to each wind turbine, a PI controller implementation may be problematic because of delays in the communication link (Martinez 2011(c)). A further problem would be in this case, the determination of the reference to be sent to each wind turbine, which would likely depend on the different loading of each turbine in the plant. A possible solution to this problem is to let proportional controllers at each wind turbine perform fast voltage control and let the outer central plant controller eliminating steady-state errors on a much slower scale (Martinez 2011(c)). In this chapter it is assumed that the voltage support by wind turbines is realized through a proportional controller, with gain K_p.

A comparison between the behavior of power plants with synchronous generators and wind turbines during and after a fault in the network is presented in (Feltes 2009, Shewarega 2009, Muljadi 2007). The authors in (Feltes 2009) show how a DFIG wind farm has better transient performance regarding active power injection. A synchronous generator with its exciter has

a slower response and despite a higher reactive power injection into the grid immediately after the fault, it becomes underexcited for at least one second. This fact, along with the fact that active power cannot be controlled worsens the voltage recovery compared to the case with a wind farm. Similar results are found in (Shewarega 2009), where the authors also show that increasing the proportional gain for GFRT voltage support strongly improves the transient stability margins of other synchronous generators connected in the same system. The paper (Muljadi 2007) compares the performance of a DFIG wind farm with a synchronous generator with focus on transient stability and rotor oscillations, concluding that a DFIG wind farm may help damping oscillations in large synchronous motors connected to the system. In (Piwko 2005) it is stated that a modern wind farm may have better transient performance as compared to traditional power plants with synchronous generation. In (Piwko 2010) a comparison is shown between a conventional combined-cycle power plant and a DFIG wind turbine. The DFIG ramps back to nominal active power in 0.2 s without the marked oscillatory behavior of the combined-cycle power plant.

7.3   Voltage Support Limits

There are limits on the voltage increase that can be achieved by reactive current injection. As pointed out in (Ashkhane 2011) and (Shewarega 2009), simultaneous active power injection can even counteract this voltage increase. The achievable voltage increase depends on the ratio between the short-circuit power and the injected power and on the *X/R* ratio at the connection point, as shown in Figure 7.2.

Two values for *X/R* have been considered, corresponding to an angle of the equivalent Thevenin impedance of respectively almost 90 degrees and 56 degrees. In Figure 7.2 , the complex power is kept constant to 1 pu and the *cos(φ)* has been varied to inject different amounts of active power.

It is seen how for high *X/R* ratios, the injection of active power, i.e. increasing *cos(φ)*, strongly reduces the maximum possible voltage increase, which is obtained for pure reactive power injection with *cos(φ)=0*. However, for weak grids with low *X/R* ratios, this no longer holds and active power injection also contributes to voltage increase. With a constant rated complex power, there is one combination of active and reactive power injection that results in maximum voltage increase. For weak grids with small *X/R* ratios, a coordinated control of active and reactive current can therefore result in better voltage support than pure reactive power injection.
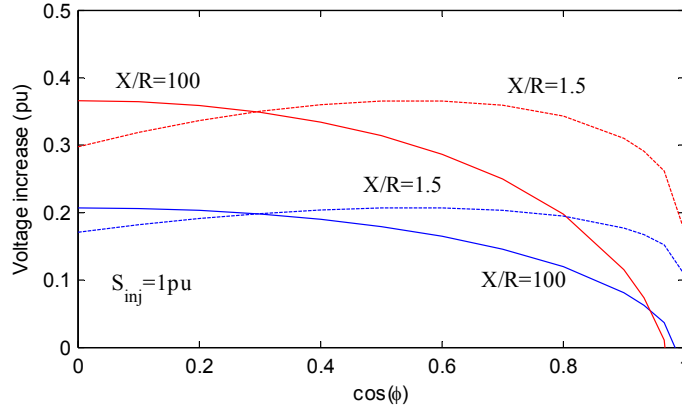
Figure 7.2 Achievable voltage increase by active and reactive power injection. $S_{sc}/S_{inj}=4$ (blue) and $S_{sc}/S_{inj}=2$ (red). Thevenin voltage of the main grid is equal to 1 pu.

7.4   Coordinated Active and Reactive Current Injection

Injecting a pure reactive current equal to the maximum rated current during a fault, as required by the majority of grid codes, is meaningful if the Thevenin equivalent impedance of the main network at the PCC is purely inductive. Weak grids connected to the main network through long cables may instead have low *X/R* ratio and prioritizing active power injection may result in better voltage support (Kayicki 2007).

In these cases, the best voltage support strategy for a wind farm is to coordinate the injection of the active and reactive current during a fault. The angle of the total injected current, with respect to the voltage at the PCC, should be close in magnitude to the angle of the network equivalent Thevenin impedance. This can be easily shown graphically. With reference to Figure 7.3, the Thevenin voltage will be the sum of the voltage at the PCC, chosen as reference, and the voltage drop over the impedance *Z*, as in Equation 7.1.

$$V_{th}e^{j\delta} = V_d - Ze^{j\theta} \cdot Ie^{j\varphi} = V_d + ZIe^{j\left(\theta + \varphi + 180°\right)} \tag{7.1}$$
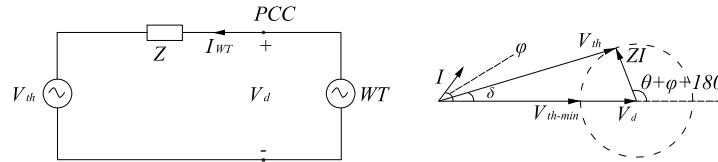
Figure 7.3 Single-line diagram of a wind turbine (WT) connected at the PCC to a grid represented with its Thevenin equivalent circuit (left) and its phasor diagram (right).

As the current angle increases, the voltage drop over the Thevenin impedance describes a circumference with radius $Z \cdot I$. The condition for maximum voltage increase, is that the Thevenin voltage is also lying on the real axis and it has minimum possible magnitude, as shown in Figure 7.3. This condition means $\theta + \varphi + 180^o = 180^o$, i.e.

$$\varphi = -\theta \tag{7.2}$$

The wind turbine current, injected into the PCC, must have an angle opposite to the network impedance angle for achieving maximum voltage increase. In the special case the Thevenin impedance angle is 90º, the optimal current angle is -90º, which means that the wind turbine should inject pure reactive power as required by actual grid codes.

The implementation of this voltage support scheme in a wind turbine is theoretically easy once the Thevenin impedance at the PCC is known. Practically, maximum wind turbine current at the optimum angle may or may not be achievable depending on the available wind turbine mechanical power. In low wind speed conditions and depending on the voltage dip magnitude, the angle of the Thevenin impedance may be such that it requires an active current, I_d, corresponding to more active power than the mechanical power available from the wind. Another issue is the mechanical stress caused by this control scheme on the wind turbine drive train, during the fault. However, in FSC wind turbines the generator is decoupled from the grid and it could in principle be controlled by the generator side converter in a way that does not result in high torque stresses. Moreover, in such wind turbines the main concern during voltage dips is the DC-link voltage increase that must be contained using a chopper. Continuing to inject some active power into the grid is beneficial to counteract the DC-link voltage increase. In a DFIG wind turbine, the proposed voltage control scheme could be implemented on the GSC, thus not directly resulting in mechanical stresses

on the drive train. Here, only the effectiveness of the proposed voltage support scheme is in focus, with no further investigation on the mechanical stresses resulting on the wind turbine drive train.

7.5   Voltage Support Strategies during Faults

Three different voltage support strategies from wind turbines in weak networks are evaluated in this chapter through simulations in PowerFactory. The three strategies are described below.

Case 1)

The first strategy follows the requirements of the Danish grid code, i.e. a reactive current injection as a function of the voltage magnitude at the PCC without any specific requirement set for the post-fault voltage recovery. A voltage deadband is also applied, so that the reactive current injection ceases when the voltage recovers above 90 % of rated value. Maximum current must be delivered when the voltage is at 50 % of rated value.

Case 2)

The second strategy is from the E.ON grid code. It is similar to the Danish grid code requirement, but it also specifies that the reactive current injection must be maintained for a further 500 ms after the voltage has returned into the deadband. Moreover, it is also required that the active power output be increased after fault clearance to its pre-fault value with a minimum gradient of 20 % of rated power per second. The characteristic of the supplied reactive current in *Case 1)* and *Case 2)* are shown in Figure 7.1.

Case 3)

The third considered strategy is the injection of a coordinated active and reactive current during the fault, as described in the previous section. The total current is let to vary proportionally to the voltage dip, as an analogy to the Danish and E.ON grid codes with a gain initially fixed to 2. After fault clearing, the wind turbine starts immediately to ramp back the active current, and hence power, to the pre-fault value. Therefore, after fault clearing the optimal angle is no longer achievable. Instead, the wind turbine enters a proportional voltage control scheme with reactive current injection without voltage deadband. The voltage control scheme could be terminated after a fixed amount of time, e.g. 10 seconds after fault clearing. The post-fault active power ramp is also assumed to have a fixed gradient, initially equal to 20 % rated power per second. This control scheme is shown in the block
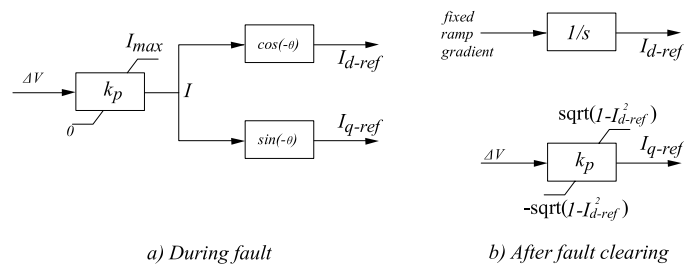
diagram of Figure 7.4.

a) During fault   b) After fault clearing

Figure 7.4 Block diagram for voltage support strategy corresponding to *Case 3*. θ is the angle of the grid Thevenin impedance seen from the PCC.

Test System

The test system used in these simulations is a simple model composed of an external 400 kV grid connected to a simple 60 kV grid made up of a load bus and a generation bus at which a FSC wind farm is connected. The wind farm is represented by using an aggregate model, i.e. with a single wind turbine with a rated power S_{WT}=35 MVA. The wind farm is initially operating at 30 MW. The load in the weak grid is initially set to 50 MW and it is composed by 60 % impedance load and 40 % induction motor load, also represented as lumped models. The connection between the 400 and the 60 kV grid can be changed to vary the short-circuit power S_{sc} at the PCC and the *X/R* ratio of the equivalent Thevenin impedance as seen from the PCC. A single line diagram of this simple system is shown in Figure 7.5.
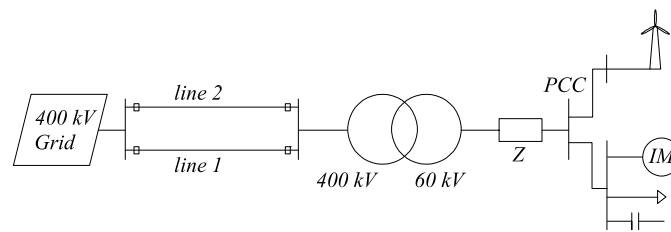
Figure 7.5 Single-line diagram of test system used in the simulations.

Three-phase short-circuit faults on one of the two 400 kV lines, cleared by line disconnection after 200 ms have been analyzed. A disconnection time of 200 ms has been considered since this represents a scenario close to the limit, for which many grid codes still require grid fault ride-through of wind turbines. In particular, the Swedish grid code requires wind turbines to ride-

through dips in the transmission system with zero voltage for 250 ms.

Short-Circuit Power and *X/R* Ratio

The performance of each of the three voltage support strategies for different ratios of the short-circuit power at the PCC and the installed wind farm power capacity are shown in Figure 7.6, where two values of S_{sc}/S_{WT} are considered, respectively 4 and 10. From Figure 7.6, it is seen how for stronger grids, the three considered voltage support schemes behave in approximately the same manner. The choice of the voltage support control scheme becomes more relevant in very weak grids. Continuous voltage support without voltage deadband, *Case 3)*, performs best.

Figure 7.6   Voltage at the PCC during a three-phase fault on 400 kV line *2*, with fault resistance 0.31 Ω. *Case 1)* (blue), *Case 2)* (red) and *Case 3)* (magenta). *X/R* ratio is approximately 12.

In Figure 7.7, it can be seen how in weak grids with low *X/R* ratio, a coordinated injection of active and reactive power along with continuous voltage support results in a faster voltage recovery as compared to pure reactive power injection with deadband. This strategy results in better voltage during the fault and as a consequence the motor load decelerates less regaining quicker its pre-fault values of speed and reactive power. The pre-fault active power from the wind farm is also re-established faster and this leads to a better voltage recovery. *Case 2)* performs better than the *Case 1)* because of the higher amount of injected reactive current, see Figure 7.1. The extra 500 ms required by the E.ON grid code bring a limited benefit.
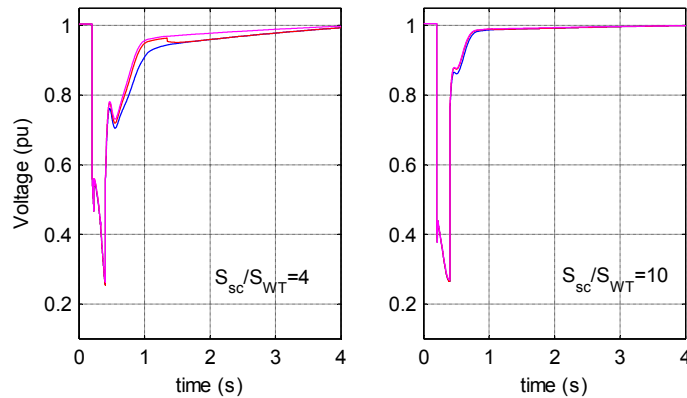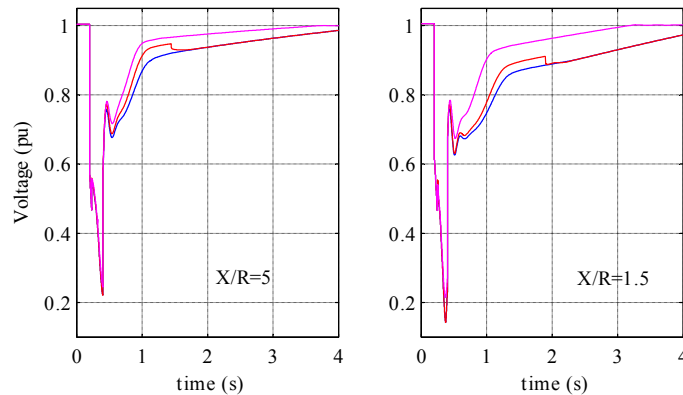
Figure 7.7   Voltage at the PCC during a three-phase fault on 400 kV line *2*, with fault resistance 0.31 Ohms. *Case 1)* (blue), *Case 2)* (red) and *Case 3)* (magenta). $S_{sc}/S_{WT} = 4$.

Controller Gain

In the simulations results presented in Figure 7.6 and Figure 7.7 the controller gain for voltage support has been assumed equal to 2, which is also the minimum requirement by the E.ON grid code. Note that in *Case 1)*, the gain is actually equal to 2.5 but the reactive current support starts from zero when the voltage is 0.9 pu, see Figure 7.1. In this section it is studied how the choice of the controller gain affects voltage recovery in weak grids with relatively low *X/R* ratios.

After fault clearing, the wind turbine will deliver a current lower than its nominal one, since the active power is being ramped up and the reactive power is low because of the low voltage deviation from nominal value. There is therefore room for an increase in controller gain, leading thus to a better exploitation of voltage support from wind turbines through reactive current injection after fault clearing.

Simulation results obtained with different controller gains are reported in Figure 7.8 and Figure 7.9. Only the voltage support schemes corresponding to *Case 2)* and *Case 3)* have been considered, since they are the ones resulting in fastest voltage recovery. The short-circuit power at the PCC is assumed to be equal to 140 MVA, i.e. 4 times the wind power installed in the weak grid.
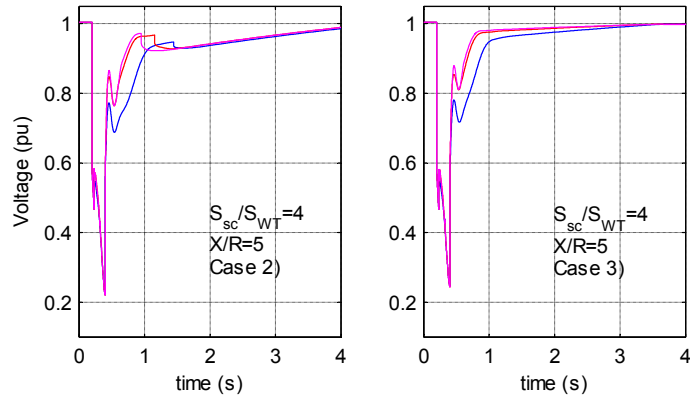
Figure 7.8   Voltage at the PCC during a three-phase fault on 400 kV line *2*, with fault resistance 0.31 Ω. K_p=2 (blue), K_p=8 (red) and K_p=14 (magenta). S_{sc}/S_{WT}=4. X/R=5.
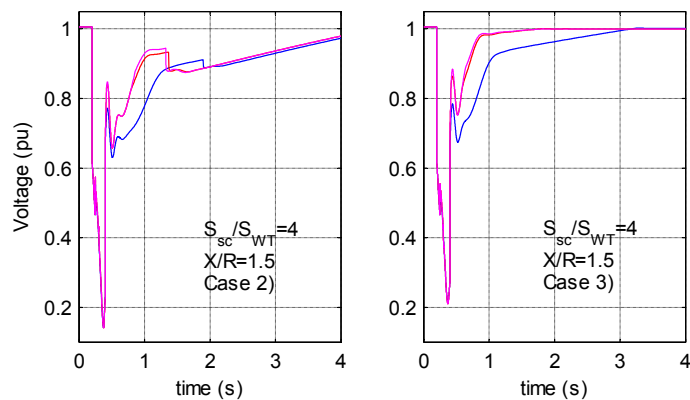
Figure 7.9   Voltage at the PCC during a three-phase fault on 400 kV line *2*, with fault resistance 0.31 Ω. K_p=2 (blue), K_p=8 (red) and K_p=14 (magenta). S_{sc}/S_{WT}=4. X/R=1.5.

In *Case 2)*, increasing the controller gain results in a faster voltage recovery until 500 ms after the voltage returns in the deadband. Voltage support ceases at this time, and for a short period the voltage may even be worse as compared to the voltage obtained with lower proportional gains, e.g. compare the voltage corresponding to K_p=8 and K_p=2 between 1.5 and 2 seconds. Some time after fault clearing, the voltage recovery is not affected by the choice of the controller gain.

In *Case 3)* instead, increasing the controller gain and applying a continuous voltage regulation without deadband is particularly effective after fault clearing. Considerable improvements on the voltage recovery can be made by increasing the controller gain up to a value of 8. This is true especially in case of weak grids with low *X/R* ratios. Further gain increases lead only to marginal voltage improvements. Increasing the controller gain does not affect the voltage during the fault, since nominal current is already being delivered with a gain of 2 for deep voltage dips. It should be noted that after fault clearing the reactive current support is not fully exploited not even in the considered cases with high proportional gain, since the total wind turbine current is still below its rated value.

Post-Fault Active Power Ramp

(Shewarega 2009, Ashkhane 2011) show how active power injection from wind turbines may even counteract the voltage support provided by reactive current injection. However, in weak grids with high loading, a fast active power ramp may contribute decisively to a better voltage recovery, since it decreases the loading on the connection to the main grid, thus reducing the voltage drop across it. The simulations results shown in Figure 7.10, Figure 7.11 and Figure 7.12 illustrate the effects of the post-fault power ramp gradient on the voltage recovery. A maximum gradient of 90 % rated power per second has been considered, as required by the UK and Irish grid code. The proportional gain K_p is assumed equal to 8 in all the considered cases.
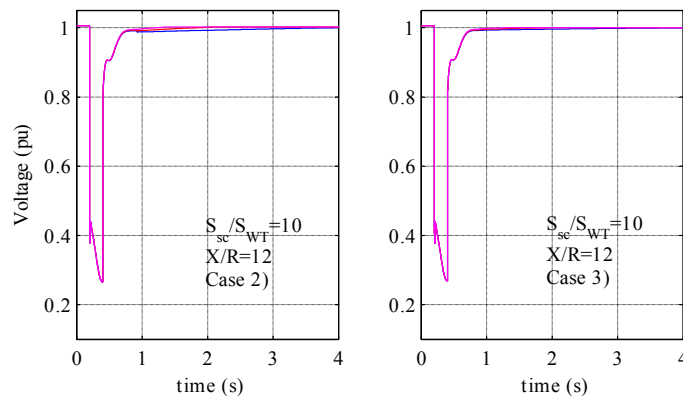
Figure 7.10 Voltage at the PCC during a three-phase fault on 400 kV line *2*, with fault resistance 0.31 Ω. *P_{ramp}=20 %/s* (blue), *P_{ramp}=50 %/s* (red) and *P_{ramp}=90 %/s* (magenta). *S_{sc}/S_{WT}=10. X/R=12.*
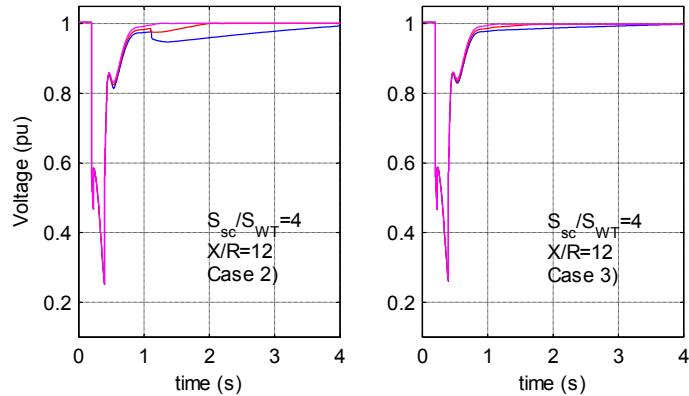
Figure 7.11 Voltage at the PCC during a three-phase fault on 400 kV line *2*, with fault resistance 0.31 Ω. P_{ramp}=20 %/s (blue), P_{ramp}=50 %/s (red) and P_{ramp}=90 %/s (magenta). S_{sc}/S_{WT}=4. X/R=12.
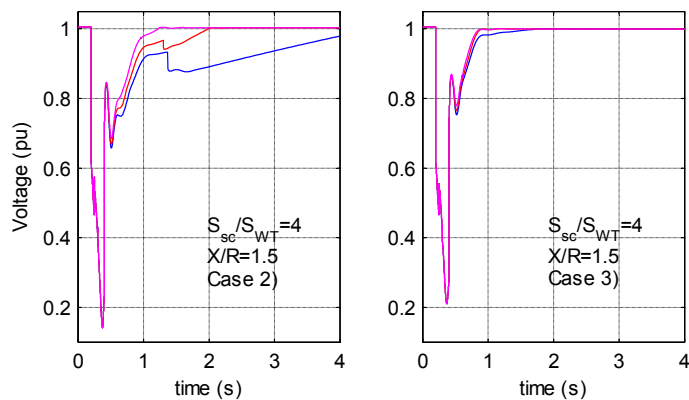
Figure 7.12 Voltage at the PCC during a three-phase fault on 400 kV line *2*, with fault resistance 0.31 Ω. P_{ramp}=20 %/s (blue), P_{ramp}=50 %/s (red) and P_{ramp}=90 %/s (magenta). S_{sc}/S_{WT}=4. X/R=1.5.

From Figure 7.11 and Figure 7.12, it can be seen how a fast active power ramp improves the voltage recovery in very weak grids, in particular in grids with low *X/R* ratios. In stronger grids, the gradient of the active power ramp does not affect significantly the voltage recovery. It is noted that in very weak grids, a fast power ramp is beneficial especially in *Case 2)*, corresponding to the voltage support scheme required by E.ON grid code. *Case 3)*, i.e. coordinated injection of active and reactive current during the fault along

with post-fault reactive current injection for voltage regulation without voltage deadband, is less sensitive to the power ramp gradient.

Summary

From the analysis of the simulation results presented up to here, it can be concluded that the choice of a particular voltage support scheme becomes relevant in very weak grids, where the ratio between the short-circuit power at the PCC and the installed wind power capacity is much less than 10. Continuous voltage support without deadband is essential for fast voltage recovery after fault clearing. A high proportional gain K_p, up to approximately 8, may help improving the voltage support from wind farms, but must also be accompanied by continuous voltage support without deadband. Further increases of K_p do not bring any additional benefit. In weak grids with low *X/R* ratios, a coordinated injection of active and reactive current may help to increase the voltage during the fault and speed-up voltage recovery after fault clearing. A fast power ramp is highly beneficial to voltage support in weak grids, especially if the *X/R* ratio is low. This is particularly true for the voltage support scheme required by E.ON's and the Danish grid codes.

7.6　　Study Case – The Bornholm Power System

The voltage support strategies evaluated in the previous sections are now compared in the case of a simplified model of a real power system, the one of the Danish island of Bornholm. This power system can be considered as a weak grid, being the ratio between the short-circuit power at the connection point with the main network, the Swedish power system, and the installed wind power capacity considered in these simulations around 6. The aim is to compare the voltage support provided by a wind farm with FSC wind turbines to that supplied by a thermal power plant with a synchronous generator, with the same rated power as the wind farm. Both a low and a high load condition in the system are considered.

Test System

The Bornholm power system is connected through a long submarine cable to the Swedish power system, represented in the model as a simple external grid. The power system contains both 60 and 10 kV buses. A detailed description can be found in (Østergaard 2011). The basic Bornholm model has been slightly modified and the final system used in these simulations is shown in Figure 7.13.

The short-circuit power from the external grid at the 60 kV bus *F60A*, where

the submarine cable is connected to the island power system, can vary between approximately 215 and 245 MVA. The *X/R* ratio varies between 1.8 and 2. The connection to the Swedish grid is modelled as a small 130 kV network with two lines. A three-phase short-circuit in the middle of the 130 kV line *2* is the basic case considered in these simulations. The fault is cleared in 200 ms by line disconnection. The line disconnection results in a reduction of the short-circuit capacity at bus *F60A* from 245 to 215 MVA.

The generation capacity in the Bornholm power system is made up of a mix of CHP, diesel and wind power plants. However in this study only a wind farm and a simplified model of a 35 MVA thermal power plant are considered. The synchronous generator in the thermal plant is equipped with an excitation system of type AC5A, representing a brushless excitation system not affected by system disturbances. This model is sometimes used to represent other types of systems when simplified models are required (IEEE Std 421.5 - 2005). A wind farm modelled as an aggregate FSC wind turbine model, with rated power 35 MVA, is connected in this study to the same bus as the thermal plant. The wind farm delivers 28 MW before the fault occurs. The ratio between the short-circuit power at node *F60A* and the wind power installed in the Bornholm grid in this study case is approximately 6. The Bornholm power system can be therefore considered as a weak grid with a quite low *X/R* ratio.

Two load scenarios are considered, one low load condition with 30 MW and one high load condition with 50 MW, representing the peak load in the system (Qiuwei Wu 2010). When analyzing the post-fault voltage recovery, modelling of the load into the system is of great importance. In the simulations presented in this section, 40 % of the load has been modelled as induction motors, which makes load modelling more realistic. Induction motors will worsen the voltage recovery by drawing reactive power from the grid. It is also assumed that reactive compensation devices are present at bus *F60A* to regulate the voltage close to nominal value under different generating conditions in the weak grid. The amount of compensation remains constant during the fault.

Figure 7.13   Single-line diagram of simplified power system of Bornholm. 130 kV (blue), 60 kV (black), 10.5 kV (brown) and 10 kV (red).

Benchmarking the Wind Turbine Voltage Support

In this section, the voltage support provided by the wind farm is compared to two other cases:

a) no generation in the weak grid

b) only one synchronous generator connected

The voltage support strategies for the wind farm are the ones corresponding to *Case 2)* and *Case 3)* in the previous section. *Case 2)* represents the voltage support requirements following E.ON grid code. *Case 3)* combines a coordinated active and reactive current injection during the fault with voltage support without deadband after fault clearing. These control strategies are evaluated either with the minimum requirements set by E.ON grid code, i.e. a proportional gain $K_p=2$ and active power ramp of 20 % rated power per second, or with $K_p=8$ and a power ramp of 90 % per second.

The analyzed case is a fault on the 130 kV line *2* cleared in 200 ms by line disconnection. The voltage in the weak grid changes when the wind farm or the synchronous generator are injecting active power or when the load changes. In this paragraph, it is assumed that the voltage is controlled in the weak grid by means of capacitors/inductors to give nominal voltage at bus *F60A*. During the fault transient, it is assumed that the amount of reactive compensation does not vary.

Low load condition

As seen in Figure 7.14, the coordinated injection of active and reactive current, *Case 3)*, results in higher voltage during the fault than in *Case 2)*. The wind farm is however not able to increase the voltage in the weak grid during the fault as the synchronous generator does. This is due to the high short-circuit currents delivered by the synchronous generator during the fault, while the wind farm keeps the current within nominal value.

Surprisingly, after fault disconnection the voltage recovery with the wind farm, operating with $K_p=2$ and $P_{ramp}=20$ %, is worse than in the case with no generation in the weak grid. To understand how this is possible, one has to consider that when no generation is connected in the weak grid, reactive power compensation needs to be added at bus *F60A* to get nominal voltage, in this case 22 Mvar. When the wind farm is connected the reactive compensation amounts to only 3.5 Mvar. This extra reactive power helps the voltage recovery after fault clearing. The post-fault voltage recovery is always

faster in *Case 3)* than in *Case 2).*

When the wind farm operates with a high proportional gain and fast active power ramp, the voltage recovery is greatly improved. In *Case 2)* however, the performance is still worse as compared to the synchronous generator case. *Case 3),* instead, results in a post-fault voltage support comparable to the synchronous generator. The voltage support from the wind farm results in no voltage oscillations after fault clearing, which are instead present in the synchronous generator case.

Figure 7.14   Voltage at bus F60A during a three-phase fault on 130 kV line *2*, with fault resistance 0.27 Ω. No generation (blue), Only SG (black), wind farm with $K_p=2$ and $P_{ramp}=20$ % (red), wind farm with $K_p=8$ and $P_{ramp}=90$ % (magenta). Total load in the Bornholm grid is 30 MW.

High load condition

The conclusions on the voltage support during the fault are the same as in the low load condition. The wind farm performs best in *Case 3)* but still not as good as the synchronous generator.

In the case of a high load condition in the weak grid, it is easier to appreciate how the post-fault voltage support provided by the wind farm is greatly dependent on the adopted scheme, see Figure 7.15. The coordinated injection of active and reactive power, along with voltage support with no deadband after fault clearing, results clearly in better voltage recovery when compared to the case in which the wind farm is supporting the grid following E.ON grid code requirements. It appears also clear the importance of choosing a high proportional gain and fast post-fault power ramp. Only in

Case 3) and with high proportional gain and fast power ramp, the post-fault voltage support provided by the wind farm is comparable to the one provided by the synchronous generator. There are two reasons that result in faster voltage recovery in *Case 3)* than in *Case 2)*. The first reason is the fact that the active current is not zero during the fault in *Case 3)* and thus the active power ramp starts from a non-zero value, thus resulting in a faster power recovery, though with the same gradient. The second reason is the improved voltage during the fault in *Case 3)*, which results in lower speed decrease of the induction motors and lower reactive power need of the motors after fault clearing, see Figure 7.16.
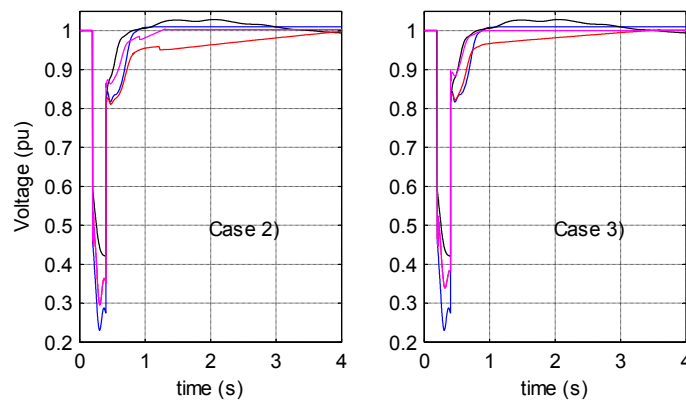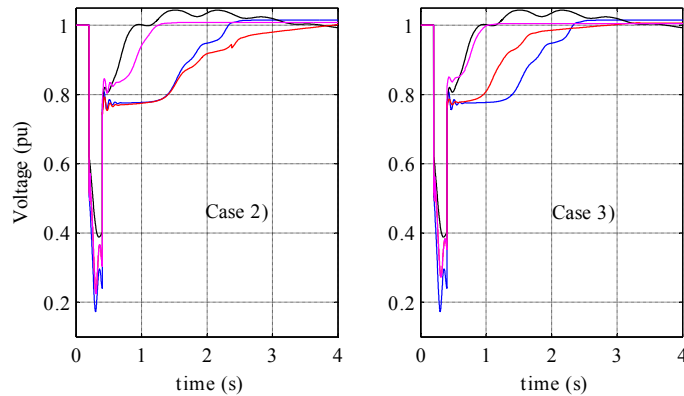

Figure 7.15   Voltage at bus F60A during a three-phase fault on 130 kV line *2*, with fault resistance 0.27 Ω. No generation (blue), Only SG (black), wind farm with $K_p=2$ and $P_{ramp}=20$ % (red), wind farm with $K_p=8$ and $P_{ramp}=90$ % (magenta). Total load in the Bornholm grid is 50 MW.

7.7   Summary

Wind turbines have the potentiality of substantially improving voltage recovery in weak networks if properly controlled and, seen from both the network and load perspective, wind turbines may be a valuable asset. In this chapter it is shown that the choice of the voltage support strategy for wind turbines becomes relevant in weak grids with low S_{sc}/S_{WT} and X/R ratios. Only FSC wind farms have been considered.

In weak grids with low X/R ratios, as is the case of grids connected to the main network through long cables, coordination between active and reactive current injection during the fault performs better than pure reactive current

injection. These effects are more evident the weaker the short-circuit power in the weak grid is.

Figure 7.16 Induction motor speed (left) and reactive power (right). *Case 2)* (blue), *Case 3)* (red), Only SG (magenta). $K_p=2$ and $P_{ramp}=20$ %. Total load in the Bornholm grid is 50 MW.

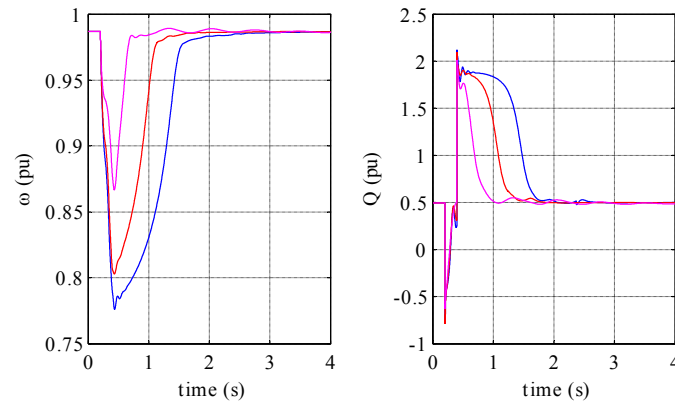A study case has been presented using a simplified model of the power system of the Danish island of Bornholm. It has been shown that the minimum requirements set in some grid codes for voltage support of wind farms are inadequate and do not result in a satisfactory voltage recovery in weak grids. When reactive compensation is used to regulate the voltage in the weak grid, the voltage recovery with wind power installed in the weak grid may even be worse than in the case with no generation in the weak grid.

However, FSC wind farms have the capability to provide a post-fault voltage support comparable to the support provided by a synchronous generator of the same size. In case of low *X/R* ratios, this requires a coordinated injection of the active and reactive current of the wind farm during the fault, along with voltage support without deadband after fault clearing. The current injected by the wind farm during the fault must have a *cos(φ)* dependant on the *X/R* ratio of the equivalent Thevenin impedance at the PCC. Moreover, a high proportional gain and a fast power ramp are also necessary to improve wind farms voltage support in a weak grid.

The voltage support provided by the synchronous generator is however superior during the fault duration and results in lower voltage drops.

Chapter 8

Conclusions and Future Work

This chapter briefly summarizes the most important results obtained in the course of this work. Suggestions for future work are given at the end.

8.1   Thesis Summary

A brief summary has been done on the research performed in the literature on the short-circuit current delivered by different types of wind turbines. The limitations of some of the proposed fault current calculation methods have been discussed. Particular attention in the literature has been given to DFIG wind turbines. Available methods in the literature mainly focus on three-phase short-circuits at the generator terminals.

A new analytical method has been proposed to calculate the fault currents of wind turbines with DFIG using crowbar protection for any symmetrical and unsymmetrical fault at any location in the grid. The proposed method can be used to calculate the peak fault current, its AC or DC component and it is a valid tool that can replace simulations when dealing with protection settings or component sizing. The method has been verified against simulations. The fault currents calculated using the analytical method show a high agreement with the results from simulations. The impact of the impedance of cables and step-up transformer, of the GSC current contribution and of the delay with which the crowbar is inserted on the accuracy of the method has been analyzed. It has been found that, in practical situations, only the crowbar insertion time can decrease the accuracy of the proposed method. If the crowbar is inserted within 5 ms from the fault, the method is still sufficiently accurate. A thorough explanation of the physical process going on in a DFIG during a short-circuit is also given. The analytical method can also be applied to calculate the fault currents of SCIG wind turbines.

Modern DFIG wind turbines may be protected using only a chopper on the DC link. The fault current contribution of this type of wind turbines is seldom analyzed in the literature. In this thesis it has been shown that the DC link capacitor and chopper are equivalent to a resistance directly connected to the DFIG rotor circuit under a symmetrical short-circuit. This implies that the methods known for fault current calculations for a DFIG with crowbar protection can also be applied to a DFIG with chopper. The proposed method allows using an equivalent DFIG with crowbar resistance instead of the DFIG with chopper. This is particularly useful since many power system simulation tools often do not include a standard model of a DFIG with chopper protection. A method to choose the value of the equivalent resistance has been proposed. The resistance value depends on the initial loading of the wind turbine and on the voltage dip during the fault. In theory for each fault case, a variable resistance should be used, but in practice it has been shown that the use of a fixed resistance results in sufficiently accurate results. It has also been shown that a DFIG with chopper protection delivers lower short-circuit currents than a DFIG with crowbar protection. The accuracy of the proposed method has been checked against simulations.

The fault current delivered by a wind farm is given by the contribution of all the individual wind turbines. Using an aggregate model with a single wind turbine of proper rating saves considerable simulation time. But how accurate is the fault current prediction using an aggregate model? Simulations performed in this work indicate that using an aggregate model of a wind farm results in sufficiently accurate fault current prediction both for SCIG and DFIG wind turbines. The aggregate model should be initialized with the average wind speed in the wind farm for better accuracy. The aggregate model should be connected to the grid through a cable, whose parameters have to be chosen to match the decay rate of the DC component in the fault current delivered by the detailed wind farm model.

GFRT requirements in Sweden are set with regard to fault on the transmission network. Fault clearing times at voltage levels below transmission network are often longer. An investigation has been performed on how GFRT of wind turbines is affected by fault at sub-transmission and medium voltage network. It has been found that the extension of the area with voltage dips so severe to endanger GFRT of wind turbines is very limited. Simulations show that accurate dynamic load modelling is important to assess the GFRT of wind turbines, while using constant impedance loads does not always result in realistic results. The cases that lead to violations of the considered GFRT curves are mainly related to high dynamic load scenarios and failure of the protection system. Faults on adjacent MV feeders

seriously endanger GFRT of wind turbines. It has been shown that the requirements in some grid codes, as the Danish and E.ON grid code, are more apt to preserve GFRT of wind turbines for faults at the MV network.

Wind turbines can contribute to a faster post-fault voltage recovery in weak grids, if properly controlled. It has been shown that the choice of the voltage support strategy becomes relevant in weak grids with low S_{sc}/S_{WT} and X/R ratios. This is the case of networks connected to the main grid through long cables. In these situations, it is useful coordinating the active and reactive power injection during faults so that the $cos(\varphi)$ is depending on the X/R ratio of the equivalent Thevenin impedance of the grid at the PCC. This proved to result in better voltage recovery as compared to pure reactive power injection, as required by some grid codes. A study case using a simplified model of the power system of the Danish island of Bornholm shows that the minimum requirements for voltage support of wind turbines set by grid codes are inadequate and result in unsatisfactory voltage recovery in weak grids. Coordinated active and reactive power injection, continuous post-fault voltage control without deadband, high proportional gain and fast active power ramp are all necessary to substantially improve wind turbine voltage support and make it comparable to the voltage support offered by synchronous generators.

8.2   Future Work

The theory laid down for the calculation of the symmetrical and unsymmetrical short-circuit current of a DFIG wind turbine with crowbar protection assumes that the generator can be modelled as a linear component without saturation. Saturation of the magnetizing and, above all, of the leakage reactances of an induction generator affects the delivered short-circuit currents. Further work to integrate the effects of saturation in the proposed method for calculation of the short-circuit current would result in improved agreement between analytical results and field measurements.

The short-circuit behavior of DFIG wind turbines with chopper protection has been analyzed only under symmetrical fault cases. The proposed method to model the DC-link with the chopper as an equivalent resistance connected to the DFIG rotor circuit should be evaluated also under unsymmetrical faults.

The proposed analytical methods for calculating the short-circuit currents of DFIG with crowbar and chopper protection have been both validated only against simulations. Lab measurements on small-scale generators would

constitute a better validation method. Field measurements of the short-circuit current from commercial wind turbines would give a more realistic picture and provide an indication of the saturation effects on the fault current.

Field measurements would be particularly interesting in the case of the fault currents delivered by commercial FSC wind turbines. Field measurements are in this case the only practical way to get a realistic insight on the fault behavior of this type of wind turbines, especially under unsymmetrical faults, which strongly depends upon the control strategy adopted by the manufacturer.

The analysis of the voltage dips resulting from faults at sub-transmission network has been carried out using a standard power system model, Nordic 32. It would be more interesting to perform the same kind of analysis on a model of a real power system. In this way, the extension of the voltage dip in the system could be directly correlated with geographic areas and a more accurate prediction on the amount of wind power experiencing GFRT problems could be made. The more realistic modelling of load behavior and of reactive power compensation devices in the system would also result in more accurate prediction of the voltage dips. Field measurements of the voltage dips in selected buses could help validating the theoretical analysis.

It has been shown that coordinating the injection of active and reactive current in a weak grid with low X/R ratio leads to better voltage support from wind turbines than the pure reactive current injection required by some grid codes. However, it has not been investigated how this voltage support strategy would affect the stresses on the mechanical drive train of wind turbines. Accurate modelling of the wind turbine drive train is necessary at this scope. The effects of injecting active current along with reactive current on the transient stability of nearby generator should also be analyzed. It is interesting to asses the voltage support from wind turbines also during island operation. In this case, using the active power to get a better voltage support would directly affect the frequency as well.

References

ABB REL650, Line Distance Protection, *Product Guide.*

ABB Type PMI, "Type PMI, 121-169 kV, up to 63 kA Power Circuit Breaker".

Abbey C., Wei L., Owatta L., Joos G., "Power Electronic Converter Control Techniques for Improved Low Voltage Ride Through Performance in WTGs", *Power Electronics Specialists Conference.* Jeju, South Korea, 2006.

Abdel-Baqi O., Nasiri A., "A Dynamic LVRT Solution for Doubly Fed Induction Generators", *IEEE Transactions on Power Electronics*, Vol. 25, No. 1, 2010.

Ackermann T., *Wind Power in Power Systems*, John Wiley and Sons, Ltd., 2005.

Aghatehrani R., Fan L., Kavasseri R., "Coordinated Reactive Power Control of DFIG Rotor and Grid Sides Converters", *IEEE PES General Meeting*, Calgary, U.S.A., 2009.

Akhmatov V., *Induction Generators for Wind Power*, Multi-Science Publishing Company Ltd., 2005.

Aluko O., Smith T. M., Tolbert L., "Behavior of Doubly-Fed Induction Generator Under Nearby Wind Plant Fault", *IEEE PES General Meeting*, Minneapolis, U.S.A., 2010.

Anderson P. M., *Analysis of Faulted Power Systems*, The Institute of Electrical and Electronics Engineers Inc., New York, 1995.

Ashkhane, Y., "A new approach to improve voltage stability in a network with fixed speed wind turbines", *19th Iranian Conference on Electrical*

131

Engineering, 2011.

Bak-Jensen B., Kawady T. A., Abdel-Rahman M. H., "Coordination between Fault-Ride-Through Capability and Overcurrent Protection of DFIG Generators for Wind Farms", *Proceedings of the 5th Nordic Wind Power Conference.* Technical University of Denmark, 2009.

Burnham D.J., Santoso S., Muljadi E., "Variable rotor-resistance control of wind turbine generators", *IEEE Power Energy Society General Meeting.* 2009.

Causebrook A., Atkinson D. J., Jack A. G., "Fault Ride-Through of Large Wind Farms Using Series Dynamic Braking Resistors", *IEEE Transactions on Power Systems*, Vol. 22, No. 3, 2007.

Chen X. S., Flechsig A. J., Pang C. W., Zhuang L. M., "Digital Modeling of an Induction Generator", *International Conference on Advances in Power System Control, Operation and Management, APSCOM-91*, Hong Kong, 1991.

CIGRÉ (1995). CIGRÉ TF 38-02-08, Long Term Dynamics Phase II, Final Report, March 1995.

Coster E., Morren J., Myrzik J., Kling W., "Comparison of MV-grid structures on fault ride through behavior of MV-connected DG-units", *20th International Conference and Exhibition on Electricity Distribution*, Prague, 2009.

Dahlgren A., Klippel C., Juntti Å., Samuelsson O., "Recorded fault ride-through capability for two types of wind turbine generators". *NWPC06 Nordic Wind Power Conference 2006*, Espoo, Finland, 22-23 May, 2006.

DigSilent PowerFactory Manual, version 14.0.519.1, 2010.

Dutta S., Overbye T. J., "A Clustering based Wind Farm Collector System Cable Layout Design". *IEEE Power and Energy Conference 2011*, Illinois, U.S.A., 2011.

Engelhardt S., Geniusz A., "Measurements of doubly fed induction generator with optimised fault ride through performance", *EWEC 2009 proceedings,* 2009.

E.ON Netz GmbH, "Grid Code – High and Extra High Voltage", Bayreuth, Germany, April 2006.

Erlich I., Wrede H., Feltes C., "Dynamic Behavior of DFIG-Based Wind Turbines during Grid Faults", *Power Conversion Conference.* Nagoya*, 2007.

Esandi I., Juankorena X., Lopez J., Marroyo L., "Alternative Protection System for Wind Turbines with Doubly Fed Induction Generator", *International Conference on Power Engineering, Energy and Electrical Drives.* Lisbon*, 2009.

Feltes C., Engelhardt S., Kretschmann J., Fortmann J., Koch F., Erlich I., "Comparison of the Grid Support Capability of DFIG-Based Wind Farms and Conventional Power Plants with Synchronous Generators", *IEEE PES General Meeting*, Calgary, U.S.A., 2009.

Flannery P.S., Venkataramanan G., "Unbalanced Voltage Sag Ride-Through of a Doubly Fed Induction Generator Wind Turbine with Series Grid-Side Converter", *IEEE Transactions on Industry Applications*, Vol. 45, No. 5, 2009.

Foster S., Xu L., Fox B., "Grid Integration of Wind Farms Using SVC and STATCOM", *41st International Universities Power Engineering Conference.* 2006.

Garcia-Gracia M., Paz Comech M., Sallan J., Llombart A., "Modelling Wind Farms for Grid Disturbance Studies", *Renewable Energy*, vol. 33, No. 9, 2008.

Glover D., Sarma M., *Power System Analysis and Design*, Brooks/Cole, 2002.

Hansen A. D., Iov F., Blaabjerg F., Hansen L. H., "Review of Contemporary Wind Turbine Concepts and their Market Penetration", *Wind Engineering*, Vol. 28, No. 3, 2004.

Hansen A. D., Michalke G., "Fault ride-through capability of DFIG wind turbines", *Renewable Energy*, Vol. 32, No. 9, 2007(a).

Hansen A. D., Michalke G., Sørensen P., Lund T., Iov F., "Co-ordinated Voltage Control of DFIG Wind Turbines in Uninterrupted Operation During Grid Faults", *Wind Energy*, Vol. 10, No. 1, 2007(b).

Horowitz S. H., Phadke A. G., *Power System Relaying*, Second Edition, Research Studies Press LTD., John Wiley and Sons Inc., 1995.

IEEE Std 421.5 – 2005, *IEEE Recommended Practice for Excitation System Models for Power System Stability Studies*, IEEE Power Engineering Society.

Jabr H. M., Kar N. C., "Effects of Main and Leakage Flux Saturation on the Transient Performances of Doubly-Fed Wind Driven Induction Generator", *Electric Power Systems Research*, Vol. 77, No. 8, 2007.

Jenkins N., Allan R., Crossley P., Kirschen D., Strbac G., *Embedded Generation*, The Institution of Electrical Engineers, London, 2000.

Kayikci M., Milanovic J.V., "Reactive Power Control Strategies for DFIG-Based Plants", *IEEE Transactions on Energy Conversion*, Vol. 22, No. 2, 2007.

Kayikci M., Milanovic J.V., "Assessing Transient Response of DFIG-Based Wind Plants - The Influence of Model Simplifications and Parameters", *IEEE Transactions on Power Systems*, Vol. 23, No. 2, 2008.

Kimbark E. W., *Power System Stability: Synchronous Machines*, Dover Publications, Inc., New York, 1968.

Kovacs P.K., *Transient Phenomena in Electrical Machines*, Elsevier, Amsterdam, 1984.

Kundur P., *Power System Stability and Control*, EPRI Power System Engineering Series, McGraw-Hill, Inc., 1993.

León-Martínez V., Montañana-Romeu J., "Analysis of Wind Generator Operations under Unbalanced Voltage Dips in the Light of the Spanish Grid Code", *Energies*, Vol. 4, No. 8, 2011.

Li H., Chen Z., "Overview of different wind generator systems and their comparisons", *IET Renewable Power Generation*, Vol. 2, No. 2, 2008.

Liang J., Qiao W., Harley R. G., "Direct Transient Control of Wind Turbine Driven DFIG for Low Voltage Ride-Through", *IEEE Power Electronics and Machines in Wind Applications.* Lincoln, Nebraska, USA, June 2009.

Lima F. K. A., Luna A., Rodriguez P., Watanabe E. H., Blaabjerg F., "Rotor

Voltage Dynamics in the Doubly Fed Induction Generator During Grid Faults", *IEEE Transactions on Power Electronics*, Vol. 25, No. 1, 2010.

Lopez J., Sanchis P., Roboam X., Marroyo L., "Dynamic Behavior of the Doubly Fed Induction Generator During Three-Phase Voltage Dips", *IEEE Trans. on Energy Conversion*, Vol. 22, No. 3, 2007.

Lopez J., Gubia E., Sanchis P., Roboam X., Marroyo L., "Wind Turbines based on Doubly Fed Induction Generator under Asymmetrical Voltage Dips", *IEEE Trans. on Energy Conversion*, Vol. 23, No. 1, 2008(a).

Lopez J., Sanchis P., Gubia E., Ursua A., Marroyo L., Roboam X., "Control of Doubly Fed Induction Generator under Symmetrical Voltage Dips", *IEEE International Symposium on Industrial Electronics.* Cambridge, UK, 2008(b).

Luna A., Rodriguez P., Teodorescu R., Blaabjerg F., "Low voltage ride through strategies for SCIG wind turbines in distributed power generation systems", *IEEE Power Electronics Specialists Conference.* Rhodes, Greece. 2008.

Manwell J. F., McGowan J. G., Rogers A. L., *Wind Energy Explained – Theory, Design and Applications*, John Wiley and Sons, Ltd., 2009.

Martínez J., Kjær P. C., Rodriguez P., Teodorescu R., "Active Current Control in Wind Power Plants during Grid Faults", *Wind Energy*, Vol. 13, No. 8, 2010.

Martínez J., Kjær P. C., Rodriguez P., Teodorescu R., "Parameterization of a Synchronous Generator to Represent a Doubly Fed Induction Generator with Chopper Protection for Fault Studies", *Wind Energy*, Vol. 14, No. 1, 2011(a).

Martínez J., Kjær P. C., Rodriguez P., Teodorescu R., "Short Circuit Signatures from Different Wind Turbine Generator Types", *IEEE/PES Power Systems Conference and Exposition*, 2011(b).

Martínez J., Kjær P. C., "Fast Voltage Control in Wind Power Plants", *IEEE Power and Energy Society General Meeting*, 2011(c).

Martinez De Alegria I., Villate J. L., Andreu J., Gabiola I., Ibanez P., "Grid Connection of Doubly Fed Induction Generator Wind Turbines: a

Survey", *European Wind Energy Conference and Exhibition.* London, November 2004.

MATLAB R2009b. SimPowerSystems User's Guide, Version 5.2.

Michalke G., Hansen A. D., "Modelling and Control of Variable Speed Wind Turbines for Power System Studies", *Wind Energy*, Vol. 13, No. 4, 2010.

Miller N. W., Price W. W., Sanchez-Gasca J. J., "Dynamic Modeling of GE 1.5 and 3.6 Wind Turbine-Generators", Version 3.0, Technical Report, GE Power Systems Energy Consulting, Schenectady NY, 2003.

Molinas M., Jon Are Suul, Undeland T., "Low Voltage Ride Through of Wind Farms With Cage Generators: STATCOM Versus SVC", *IEEE Transactions on Power Electronics*, Vol. 23, No. 3, 2008.

Morren J., de Haan S. W. H., "Short-circuit current of wind turbines with Doubly Fed Induction Generator", *IEEE Trans. on Energy Conversion*, Vol. 22, No. 1, 2007.

Mullane A., Lightbody G., Yacamini R., "Wind-Turbine Fault Ride-Through Enhancement", *IEEE Transactions on Power Systems*, Vol. 20, No. 4, 2005.

Muljadi E., Butterfield C. P., Ellis A., Mechenbier J., Hochheimer J., Young R., Miller N., Delmerico R., Zavadil R., Smith J. C., "Equivalencing the Collector System of a Large Wind Power Plant", *IEEE Power Engineering Society General Meeting*, 2006.

Muljadi E., Butterfield C. P., Parsons B., Ellis A., "Effect of Variable Speed Wind Turbine Generator on Stability of a Weak Grid", *IEEE Transactions on Energy Conversion*, Vol. 22, No. 1, 2007.

Muyeen S. M., Takahashi R., Murata T., Tamura J., "A Variable Speed Wind Turbine Control Strategy to Meet Wind Farm Grid Code Requirements", *IEEE Transactions on Power Systems*, Vol. 25, No. 1, 2010.

Neumann T., Feltes C., Erlich I., "Response of DFG-based wind farms operating on weak grids to voltage sags", *2011 IEEE Power and Energy Society General Meeting.* Detroit, USA, 2011.

Nguyen D. H., Negnevitsky M., "A review of fault ride through strategies for different wind turbine systems", *20th Australasian Universities Power Engineering Conference.* Christchurch, New Zeland, 2010.

Pannell G., Atkinson D., Kemsley R., Holdsworth L., Taylor P., Moja O., "DFIG Control Performance Under Fault Conditions for Offshore Wind Applications", *18th International Conference and Exhibition on Electricity Distribution*, Turin, Italy, 2005.

Pannell G., Atkinson D. J., Zahawi B., "Analytical Study of Grid-Fault Response of Wind Turbine Doubly Fed Induction Generator", *IEEE Trans. on Energy Conversion,* Vol. 25, No. 4, 2010.

Perdana A., Uski-Joutsenvuo S., Carlson O., Lemström B., "Comparison of an aggregated model of a wind farm consisting of fixed-speed wind turbines with field measurement", *Wind Energy*, Vol. 11, No. 1, 2008.

Petersson A., "Analysis, Modeling and Control of Doubly-Fed Induction Generators for Wind Turbines", *PhD Thesis*, Chalmers University of Technology, Göteborg, Sweden 2005 (a).

Petersson A., Lundberg S., Thiringer T., "A DFIG Wind Turbine Ride-Through System. Influence on the Energy Production", *Wind Energy*, Vol. 8, No. 3, 2005 (b).

Piwko R., Miller N., Sanchez-Gasca J., Yuan X., Dai R., Lyons J., "Integrating Large Wind Farms into Weak Power Grids with Long Transmission Lines", *IEEE/PES Transmission and Distribution Conference and Exposition: Asia and Pacific*, Dalian, China, 2005.

Piwko R., Miller N., Girad R. T., MacDowell J., Clark K., Murdoch A., "Generator Fault Tolerance and Grid Codes", *IEEE Power and Energy Magazine*, Vol. 8, No. 2, 2010.

Pöller M., Achilles S., "Aggregated Wind Park Models for Analyzing Power System Dynamics", *Fourth international workshop on large-scale integration of wind power and transmission networks*, Billund, Denmark, October 2003.

Pure Power – Wind Energy Targets for 2020 and 2030, report by the European Wind Energy Association, 2011.

Qiuwei Wu, Seung Tae Cha, Østergaard J., "Test Site for Smart Grid

Technologies – Bornholm Power System", Internal report, Department of Electrical Engineering, Technical University of Denmark, 2010.

Rahimi M., Parniani M., "Grid-fault ride-through analysis and control of wind turbines with doubly fed induction generators", *Electric Power Systems Research*, Vol. 80, No. 2, 2010.

REN21. Renewables 2011 Global Status Report, 2011.

Roeper R., *Short-circuit Currents in Three-phase Systems*, Siemens Aktiengesellschaft, John Wiley and Sons, 1985.

Salles M., Cardoso J.R., Grilo A.P., Rahmann C., Hameyer K., "Control strategies of doubly fed induction generators to support grid voltage", *IEEE International Electric Machines and Drives Conference,* Miami, U.S.A., 2009.

Samaan N., Zavadil R., Smith J. C., Conto J., "Modeling of Wind Power Plants for Short Circuit Analysis in the Transmission Network", *IEEE/PES Transmission and Distribution Conf. and Exposition*, 2008.

Sarma M. S., *Electric Machines – Steady-state Theory and Dynamic Performance*, West Publishing Company, 1986.

Seman S., Niiranen J., Kanerva S., Arkkio A., Saitz J., "Performance Study of a Doubly Fed Wind-Power Induction Generator Under Network Disturbances", *IEEE Transactions on Energy Conversion*, Vol. 21, No. 4, December 2006 (a).

Seman S., Niiranen J., Arkkio A., "Ride-Through Analysis of Doubly Fed Induction Wind-Power Generator Under Unsymmetrical Network Disturbance", *IEEE Transactions on Power Systems*, Vol. 21, No. 4, November 2006 (b).

Shewarega F., Erlich I., Rueda J. L., "Impact of large offshore wind farms on power system transient stability", *EEE/PES Power Systems Conference and Exposition.* Seattle, U.S.A., 2009.

Souza L. F. W., Assis T. M. L., Visconti I. F., "On the assessment of voltage ride-through needs of the power transmission Grid", *IREP Symposium Bulk Power System Dynamics and Control - VIII.* Rio de Janeiro, Brazil, 2010.

Strachan N. P. W., Jovcic D., "Stability of a Variable-Speed Permanent

Magnet Wind Generator with Weak AC Grids", *IEEE Transactions on Power Delivery*, Vol. 25, No. 4, November 2010.

"SvKFS 2005:2, Affärsverket Svenska Kraftnäts Föreskrifter och Allmänna Råd om Driftsäkerhetsteknisk Utformning av Produktionsanläggningar", Svenska Kraftnät, 2005, (in Swedish).

Taylor C. W., *Power System Voltage Stability*, McGraw-Hill International Editions, Electrical Engineering Series, 1994.

"Technical Regulation 3.2.5 for Wind Power Plants with a Power Output Greater than 11 kW, rev. 4.1", Energinet.dk, Denmark, 2010.

Transpower, "Upper North Island – Reactive Support Investigation Project – Attachment A", 2009, available online at: http://www.gridnewzealand. co.nz/f2504,36732500/upper-north-island-consultation-attachment-a.pdf

"TR2-05-2-1, Ledningsskyddssystem för Stamnätet", rev. D, Svenska Kraftnät, 2010, (in Swedish).

Tsili M., Papathanassiou S., "A review of grid code technical requirements for wind farms", *IET Renewable Power Generation*, Vol. 3, No. 3, 2009.

Ullah N. R., Thiringer T., Karlsson D., "Voltage and Transient Stability Support by Wind Farms Complying With the E.ON Netz Grid Code", *IEEE Transactions on Power Systems*, Vol. 22, No. 4, 2007.

Vas P., *Electrical Machines and Drives - A Space-Vector Theory Approach*, Oxford Science Publications, 1992.

Vicatos M. S., Tegopoulos J. A., "Transient State Analysis of a Doubly-Fed Induction Generator under Three Phase Short Circuit", *IEEE Trans. on Energy Conversion*, Vol. 6, No. 1, 1991.

"Vindkraftstatistik 2010 – ES 2011:06", report by Energimyndighet, 2011. (In Swedish).

Walling R. A., Reichard M. L., "Short circuit behavior of wind turbine generators", *62nd Annual Conference for Protective Relay Engineers.* 2009.

Webpage, *http://www.pes-psrc.org/c/CWG17.html*. Power System Relaying Committee, System Protection Subcommittee. C17 - Fault Current

Contribution from Wind Plants.

Yang C., Gan-gui Y., Da-wei J., Gang M., Zhi-qiang Z., Xiao-bo W., Li Qiang, "DFIG-based Wind Farm Equivalent Model for Power System Short Circuit Current Calculation", *International Conference on Sustainable Power Generation and Supply*, Nanjing, China, 2009.

Yang J., Dorrell D.G., Fletcher J.E., "A new converter protection scheme for doubly-fed induction generators during disturbances", *34th Annual Conference of IEEE Industrial Electronics.* Orlando, U.S.A., November 2008.

Xiang D., Ran L., Tavner P.J., Yang S., "Control of a doubly fed induction generator in a wind turbine during grid fault ride-through", *IEEE Transactions on Energy Conversion*, Vol. 21, No. 3, September 2006.

Zhou P., He Y., Sun D., Zhu J. G., "Control and Protection of a DFIG-Based Wind Turbine under Unbalanced Grid Voltage Dips", *IEEE Industry Applications Society Annual Meeting.* Edmonton, Alberta, Canada, October 2008.

Østergaard J., Nielsen J. E., "The Bornholm Power System – An Overview", 14th Edition, Kgs. Lyngby, Denmark, April 2011.